Real-time Performance Evaluation of TDD Reciprocity Calibration for Distributed Antenna Systems

Dissertation

submitted to

Sorbonne Université

in partial fulfillment of the requirements for the degree of
Doctor of Philosophy

Author:

Theoni MAGOUNAKI

Scheduled for defense on the 14th December, 2020, before a committee composed of:

Reviewers		
Prof.	**Danijela CABRIC**	UCLA, California
Associate Prof.	**Luca SANGUINETTI**	University of Pisa, Italy
Examiners		
Prof.	**Raymond KNOPP**	EURECOM, France
Prof.	**Fabien FERRERO**	UCA, France
Assistant Research Prof.	**Rahman DOOST-MOHAMMADY**	Rice University, Texas
Director of Thesis		
Assistant Prof.	**Florian KALTENBERGER**	EURECOM, France
Co-Director of Thesis		
Dr.	**Philippe RATAJCZAK**	Orange Labs, France

Évaluation des performances en temps réel de l'étalonnage de réciprocité en TDD pour les systèmes d'antennes distribuées

Thèse

soumise à

Sorbonne Université

pour l'obtention du Grade de Docteur

Auteur:

Theoni MAGOUNAKI

Soutenance de thèse effectuée le 14 Decembre 2020 devant le jury composé de:

Rapporteurs		
Prof.	**Danijela CABRIC**	UCLA, Californie
Associate Prof.	**Luca SANGUINETTI**	Université de Pise, Italie
Examinateurs		
Prof.	**Raymond KNOPP**	EURECOM, France
Prof.	**Fabien FERRERO**	UCA, France
Assistant Research Prof.	**Rahman DOOST-MOHAMMADY**	Université Rice, Texas
Directeur de Thèse		
Assistant Prof.	**Florian KALTENBERGER**	EURECOM, France
Co-Directeur de Thèse		
Dr.	**Philippe RATAJCZAK**	Orange Labs, France

To my family

Abstract

Massive multiple-input multiple-output (MIMO) is one of the key enabling physical layer technologies to address the massive capacity requirement demanded by 5G systems. Massive MIMO exploits the use of large antenna arrays at the base station (gNB) to simultaneously serve multiple users through spatial multiplexing over a channel. Massive MIMO relies on uplink pilots to obtain channel state information (CSI), exploiting channel reciprocity and time division duplexing (TDD) operation. In reality, however, the communication channel does not only consist of the physical channel in the air, but also the radio-frequency (RF) front-ends in transceivers which are not reciprocal. Therefore the system needs to be calibrated before channel reciprocity can be exploited. Distributed massive MIMO with spatially separated antennas gives a higher spectral efficiency and enhanced coverage area, compared to collocated massive MIMO. Nevertheless, coordinating a large number of remote radio units (RRUs), forming the gNB, is a big challenge. Hence, TDD reciprocity calibration and RRU synchronization are the two key factors to enable distributed massive MIMO.

In this thesis, we focus on deploying a distributed massive MIMO system on the OpenAirInterface (OAI) 5G testbed and applying real-time channel calibration algorithms in order to evaluate their performance. The main contributions can be summarized as follows. First, we implement the precoder function and the multi-thread parallelization for the optimal performance of the functional splits in our Cloud-RAN (C-RAN) system while increasing the number of active RRUs. Second, we present the low-cost solutions for the hardware issues resulting from our RRUs forming the distributed antenna system (DAS). Also, we analyze the methods used for time/frequency/phase synchronization and calibration in our testbed. Third, we carried out real-time measurements on our C-RAN testbed in order to prove the stable and precise synchronization between several RRUs and confirm the efficiency of the proposed group-based reciprocity calibration scheme. Fourth, we provide a ground truth for the evaluation of the group-based over-the-air (OTA) calibration framework through channel measurements on a simulated DAS. Last but not least, enabled by TDD reciprocity calibration, we built up a multiple-input single-output (MISO) testbed based on the OAI platform, in order to facilitate the evaluation of relative calibration and simultaneously access the performance of the MIMO antenna prototypes designed by the team in Orange labs.

Acknowledgements

Foremost, I would like to express the deepest appreciation to my academic advisor Florian Kaltenberger, for his thorough assistance and guidance during my thesis. I would also like to thank Prof. Fabien Ferrero, my industrial supervisor Philippe Ratajczak and Jean-Louis Desvilles, for offering me this great opportunity to be a part of the Orange labs team. Also, I am trully grateful to Prof. Raymond Knopp, Cedric Roux and Tsu-Han Wang for helping me realize and implement new concepts. Next, I would like to thank two past Ph.D. students, Xiwen Jiang and Cyril Buey, for their careful and precious guidance which was extremely valuable for my studies both theoretically and practically. I am grateful for having the chance to meet these wonderful people and professionals who led me though these Ph.D. years.

I could not have completed these studies without the support of my friends in France and Greece. Thank you for all the trips, the parties and the unforgettable moments we had together. You groove me. Special thanks to Kathy and Stamatis for tolerating me. I feel very lucky for having you.

Finally, I am extremely grateful to my parents for their unconditional love, continuing support and sacrifices for educating and preparing me for my future life. You are the driving force in my life. I love you like any words can say.

Contents

List of Figures

List of Tables

Acronyms and Abbreviations

The acronyms and abbreviations used throughout the manuscript are specified in the following. They are presented here in their singular form, and their plural forms are constructed by adding and s, e.g. RRU (Remote Radio Unit) and RRUs (Remote Radio Units). The meaning of an acronym is also indicated once, the first time appearing in the text.

3GPP	Third Generation Partnership Project
5G	Fifth Generation
ADC	Analog-to-digital converter
AI	Artificial Intelligence
AWGN	Additive White Gaussian Noise
BBU	BaseBand Unit
BS	Base Station
CA	Carrier Aggregation
CAPEX	Capital Expenditure
CDD	Cyclic Delay Diversity
CDMA	Code-Division Multiple Access
CN	Core Network
CPU	Central Processing Unit
C-RAN	Cloud-Radio Access Network
CP	Cyclic Prefix
CPRI	Common Public Radio Interface
CSI	Channel State Information
CSIT	Channel State Information at the Transmitter
DAC	Digital-to-Analog Converter
DAS	Distributed Antenna System
DL	DownLink
DMRS	Demodulation Reference Signal
ECP	Extended Cyclic Prefix
EPC	Enhanced Packet Core
FC	Fast Calibration
FDD	Frequency-Division Duplex
FPGA	Field Programmable Gate Array
FTT	Fast Fourier Transform

gNB	gNodeB
GPS	Global Positioning System
HPA	High Power Amplifier
HSS	Home Subscriber Server
IFFT	Inverse Fast Fourier Transform
i.i.d.	Independent and Identically Distributed
IRIG	Inter Range Instrumentation Group
LDS	Laser Direct Structuring
LO	Local Oscillator
LOS	Line Of Sight
LS	Least Squares
LTE	Long Term Evolution
LNA	Low Noise Amplifier
MAC	Multiple Access Channel
MCS	Modulation and Coding Scheme
MIMO	Multiple-Input Multiple-Output
MISO	Multiple-Input Single-Output
ML	Machine Learning
MME	Mobility Management Entity
MMSE	Minimum Mean Square Error
mmWave	Millimeter Wave
MRT	Maximum Ratio Transmission
MSE	Mean Square Error
MU	Multi-User
NLOS	Non Line Of Sight
NR	New Radio
OAI	OpenAirInterface
OCXO	Oven-Controlled Crystal Oscillator
OFDM	Orthogonal Frequency Division Multiplexing
OFDMA	Orthogonal Frequency Division Multiple Access
OPEX	Operational Expenditure
OTA	Over-The-Air
PA	Power Amplifier
PBCH	Physical Broadcast Channel
PCB	Printed Circuit Board
PCIe	Peripheral Component Interconnect Express
PDCCH	Physical Downlink Control Channel
PDCP	Packet Data Convergence Protocol
PDSCH	Physical Downlink Shared Channel
PGw	Packet Data Network Gateway
PLL	Phase-Locked Loop
PoE	Power over Ethernet
PPS	Pulse Per Second
PRB	Physical Resource Block

PSS	Primary Synchronization Sequence
PTP	Precision Time Protocol
PUCCH	Uplink Shared Channel
PUSCH	Uplink Control Channel
QPSK	Quadrature Phase-Shift Keying
RAN	Radio Access Network
RAU	Radio Aggregation Unit
RB	Resource Block
RCC	Radio Cloud Center
RE	Resource Element
RF	Radio Frequency
RLC	Radio Link Control
RRC	Radio Resource Control
RRU	Remote Radio Unit
RS	Reference Signal
Rx	Receiver
SGw	Serving Gateway
SINR	Signal to Interference and Noise Ratio
SM	Spatial Modulation
SNR	Signal to Noise Ratio
SRS	Sounding Reference Signal
SSF	Special SubFrame
SyncE	Synchronous Ethernet
TDD	Time Division Duplex
TM	Transmission Mode
Tx	Transmitter
UE	User Equipment
UL	UpLink
USRP	Universal Software Radio Peripheral
UTC	Coordinated Universal Time
VCD	Value Change Dump
VCO	Voltage-Controlled Oscillator
VCTCXO	Voltage-Controlled Temperature Compensated Crystal Oscillators
ZF	Zero Forcing
ZFBF	Zero-Forcing Beamforming

Chapter 1

Introduction

During the last years, data traffic (fixed/mobile) has grown exponentially due to the dramatic growth of wireless/wired data consuming devices. Globally, devices and connections are growing faster than both the population and the Internet users [2]. Each year, various new devices in different form factors with increased capabilities and intelligence are introduced and adopted in the market, Fig. 1.1. A growing number of machine to machine[1] (M2M) applications, such as smart meters, video surveillance, healthcare monitoring, transportation, and package or asset tracking, are contributing in a major way to the growth of devices and connections. By 2023, M2M connections will be the fastest-growing device and connections category. New technologies are required to meet this demand. Related to wireless data traffic, the performance limitation will always be at the physical layer because of the limited available spectrum, the strict laws of electromagnetic propagation, and the principles of information theory.

There are three principle ways of improving the efficiency of a wireless network:

1. Operating more spectrum. The abundant spectrum available at mmWave frequency bands above 24 GHz is capable of delivering extreme data speeds and capacity [3],

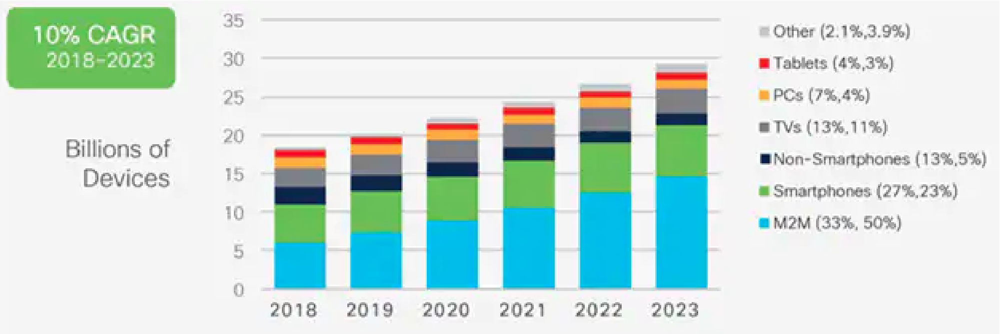

Figure 1.1 – Global device and connection growth.

---

[1] Machine to machine is direct communication between devices using any communications channel, including wired and wireless.

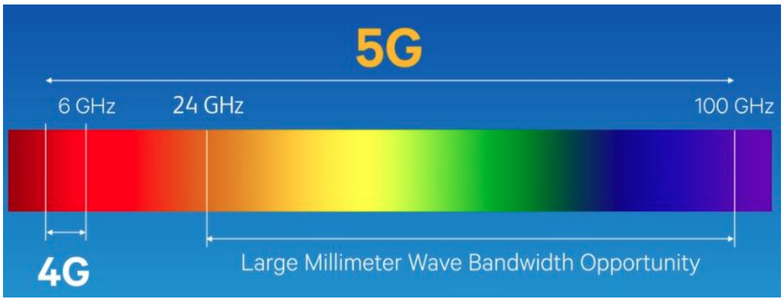

Figure 1.2 – mmWave and 5G

Fig. 1.2. Nonetheless, the mmWave RF complexity does not match with the cost and power constraints of the mobile devices.

2. Deploying access points (APs) more densely. That is a popular approach, named *small cells*. However, this solution intensifies the interference problem because of the short distances betweeen the APs.

3. Increasing the spectral efficiency[2].

A well-known way to increase the spectral efficiency is using multiple antennas at the transceivers, also known as multiple-input multiple-output (MIMO) technology. In wireless communications, the transmitted signals are attenuated by fading due to multipath propagation and by shadowing due to large obstacles between the transmitter and the receiver, yielding a fundamental challenge for reliable communication. MIMO technology provides two types of gains: *diversity gain* that combats channel fading and enhances the reliability of wireless communications and *spatial multiplexing gain* that increases the data rate, and improves the network capacity.

MIMO technology can be classified into one of three categories: single-user MIMO (SU-MIMO), multi-user MIMO (MU-MIMO) and massive MIMO. In SU-MIMO, a base station (BS) transmits multiple spatial streams at once, but only to one user at a time. On the other hand, MU-MIMO allows multiple spatial streams to be assigned to different user equipments (UEs) simultaneously, increasing the total throughput and capacity of the system [4]. MU-MIMO concept builds upon the transmit beamforming capabilities to establish simultaneous directional RF links between the BS and all the active UEs, using the same time-frequency resources. The BS uses enhanced beamforming techniques to maximize transmission in the desired user direction while simultaneously minimizing transmission in the direction of undesired users through null steering [5]. Known as spatial reuse, this technique provides to each one of the active UEs with its own dedicated full-bandwidth channel [6, 7].

Massive MIMO, is an extension of MU-MIMO, which uses an order of magnitude more antennas than classical MIMO systems and improves the end user experience by significantly increasing network capacity and coverage while also reducing interference [8].

---

[2] Spectral efficiency, measured in bit/s/Hz, refers to the information rate that can be transmitted over a given bandwidth.

The “massive” number of antennas helps focus energy, bringing huge improvements in throughput and radiated energy efficiency. Massive MIMO is a key enabler of 5G’s extremely fast data rates and relies on uplink pilots to obtain channel state information (CSI), exploiting channel reciprocity and time division duplexing (TDD) operation. In a multi-antenna spatial coexistence scenario, beamforming allows control of the mutual interference. The TDD mode, which is the main mode envisaged for massive MIMO and cellular 5G, largely facilitates this coexistence due to the possible exploitation of channel reciprocity.

1.1 Motivation

One of the most fundamental challenges in modern wireless communication systems is to meet an ever-increasing demand for network throughput from ever-increasing numbers of users. One way of meeting this demand is the use of the emerging massive MIMO technology which is capable of greatly enhancing the spectral efficiency by serving multiple users at the same time-frequency resource via TDD operation.

Massive MIMO represents one of the key 5G RAN technologies because it improves energy efficiency [9]. Also, by the law of large numbers, the randomness of the wireless channel introduced by small-scale fading can be hardened statistically to provide more predictable system performance [10]. Furthermore, as long as the number of transmit antennas is much larger than the number of simultaneously served users, the system throughput can be greatly enlarged by the high rank of MU-MIMO scheme [8].

To deploy the massive MIMO systems, two main topologies can be considered: collocated massive MIMO, where the base station antennas are co-located in a single array in the cell center, and distributed massive MIMO, where the BS antennas are geographically distributed over the cell, creating what is widely known as distributed antenna system (DAS). In DAS, we make use of remote radio units (RRUs) to provide more uniform coverage especially in shadowed and indoor locations. The RRUs are equipped with one or more antennas and are connected to a central processing unit (CPU) using a high-bandwidth low-latency dedicated connection. The information exchange between the RRUs and the CPU is limited to the payload data, and power control coefficients that change slowly. There is no sharing of instantaneous CSI among the RRUs or the central unit. All channels are estimated at the RRUs through uplink pilots. The obtained channel estimates are used to precode the transmitted data in the downlink and to perform data detection in the uplink. In addition, since the users are close to the RRUs, DAS can offer a high coverage probability. Conjugate beamforming/matched filtering techniques, also known as maximum-ratio processing, are used both on uplink and downlink [11]. These techniques are computationally simple and can be implemented in a distributed manner, locally at the RRUs.

In conclusion, the distributed massive MIMO approach has several advantages compared to a conventional massive MIMO system with co-located antennas, such as enhanced coverage area and ease of networking planning, decreased shadowing effect and better decorrelation of channels even for closely located users [12]. Nevertheless, in practice, several challenges should be addressed to deploy a distributed massive MIMO system.

Those are the synchronization of distributed local oscillators, amplifier non-linearities, non-ideal analog filters [13] and the critical TDD channel reciprocity.

In TDD systems, channel reciprocity means that the physical channel in the air, within the channel coherence period, for both UL and DL is the same. However, the channel includes not only the physical channel in the air, but also the radio frequency (RF) front-ends on the transceivers, as channel estimation is applied in the digital domain. As these two RF front-ends are distinct, the channel is not reciprocal from a digital signal processing point of view. In the CSIT calculation, failure to account for hardware asymmetry will cause inaccuracy and, as a consequence, significant degradation in the downlink beamforming efficiency [14–17]. Calibration techniques are required to compensate for hardware symmetry and achieve maximum channel reciprocity. Even before the emergence of the massive MIMO systems, this subject was investigated. In [18–22], authors recommend that transceivers that are dedicated to calibration add additional hardware components. The RF asymmetry in the transceivers is compensated by this approach, but it does not appear to be a cost-effective solution. Thus, "over-the-air" (OTA) calibration schemes are proposed in [23–26] where calibration coefficients are calculated using signal processing methods based on BS and UE bi-directional channel estimations. Because hardware properties can be assumed to remain reasonably constant, they can be used later to modify instantaneous UL channel estimation to evaluate the CSIT once these coefficients are obtained in the initialization process of the system (*calibration phase*). In the calibration phase, conventional OTA calibration methods include UE, meaning that UEs must feed their estimated DL channel back to the BS. Although, the calibration coefficients are reasonably stable in time, and the system does not repeat the calibration very often, for large MIMO systems, feeding back DL channel data for all BS antennas is still a heavy process. This led to a new group of calibration schemes that calibrate the system internally at BS without the aid of UE ("BS internal calibration") [27–32]. Many problems are still unsolved, despite these accomplishments, and these calibration methods need to be verified in a real system with a distributed antenna topology:

- What is the best way to calibrate a TDD distributed massive MIMO system?
- Do the geometrical characteristics of the area where the antennas are distributed affect the performance of each calibration algorithm?
- What do those calibration parameters look like in a practical system?
- How to assign the calculation tasks of the calibration parameters between the CPU and the radio units?
- Is it possible to not interrupt the data service when the system is calibrating itself?

For LTE/5G mobile communications standards, precise synchronization is a key requirement for the implementation of spatially distributed massive MIMO systems. Many applications based on MIMO transmissions such as beamforming methods, require high-precision synchronization among the transmit nodes. A distributed massive MIMO network requires time synchronization and phase coherence between each RF chain. This is achieved using a reference clock and trigger distribution topology. This provides phase coherence among devices. The trigger signal is used to provide a time reference to all the spatially distributed radios in the system. All Field Programmable Gate Arrays (FPGAs) receive this time-aligned trigger, so processing starts simultaneously. State synchronization is ensured by invoking a state reset on all devices prior to the trigger event, [33].

Current state-of-the-art large MIMO testbeds use coaxial cables to transmit synchronization signals to slave devices and subsequently to the RF front-ends from a master clock source [27, 34]. The signal phase is determined by the time of propagation and therefore by the coaxial cable's variable length. Damping, environmental distortions and impairments in propagation are proportional to the length of the cables and are a limit to the efficiency of the synchronization signal. Packet-based synchronization techniques can be used to synchronize several radio units, in comparison to direct frequency transfer using coaxial cables. The IEEE 1588 Precision Time Protocol (PTP) is often used, where the accuracy and resolution of the timestamps provide highly precise synchronization [35]. Synchronous Ethernet (SyncE) is another synchronization method which brings direct frequency transfer into packet-based networks [36]. With SyncE, the transmitter clock is regenerated using a phase-locked loop (PLL) on the receiver side, enabling distributed radio units to operate at the same frequency as the source. The precision is primarily determined by the oscillators and components of the PLL. Alternatively, the White Rabbit timing system [37], developed at CERN, combines the IEEE 1588 Precision Time Protocol (PTP) with SyncE using fiber optics providing high-accurate synchronization. Finally, in [28], the authors do not rely at all on wired synchronization, but suggest an OTA synchronization protocol that scales well with the size of the network.

The cloud-RAN (C-RAN) or Open-RAN (O-RAN) architectures are one possible way of implementing distributed Massive MIMO by centralizing a major part of the processing of the physical layer on a central server. The C-RAN architecture allows for flexible functional splits in the radio network between various processing components, for an optimal trade-off between cloud or RRU processing. Eurecom has built and deployed a C-RAN testbed which consists of various RRUs connected by Gbit Ethernet to a switch which are in turn connected to a central server over optical 20Gbit Ethernet [38]. Frequency synchronization is provided by a clock distribution unit and timing synchronization is achieved by a special OTA protocol. Based on this particular C-RAN testbed and using the OpenAirInterface (OAI) platform, we are investigating in this thesis the challenges for deploying a distributed massive MIMO testbed:

- How to stabilize timing and frequency synchronization while increasing the number of the active distributed radio units.
- Finding efficient solutions for the low-cost radio units we use, when hardware-related problems arise regarding the inter-RRU synchronization.
- Optimizing the multi-thread parallelization for the lower-layer functional splits of the C-RAN testbed while increasing the number of RRUs.

1.2 Contributions

This thesis mainly concerns deploying a low-cost distributed antenna system based on the OpenAirInterface 5G platform and evaluating the performance of the proposed fast calibration scheme [32] in a real-time environment. In this section, we summarize the achieved results and the contributions.

1.2.1 Performance Evaluation of Relative Calibration Methods on our C-RAN testbed

In Section 4.1 we describe the system architecture of our C-RAN testbed deployed at Eurecom using OpenAirInterface (OAI) software and inexpensive commodity hardware. We discuss the synchronization and calibration algorithms implemented in our network and we analyze the hardware problems we had to overcome (Section 4.4). We achieved to maintain OTA synchronization between several RRUs and confirmed the efficiency of the proposed fast calibration (FC) schemes based on RRU grouping in real environment. Our results were based on based on the variance of the time-domain calibration elements and illustrated that the FC algorithm with equally partitioned groups outperforms the existing Argos, Rogalin and Avalanche methods in [27, 28, 31]. Moreover, we presented the case where the overall estimation performance of our FC algorithm improves when we try to minimize the size of the largest RRU group. Finally, we proved through real-time measurements that the interleaved grouping of the RRUs results in performance gains.

These results are presented in Chapter 5 and published in:

- T. Magounaki, F. Kaltenberger, and R. Knopp, “Real-time Performance Evaluation of Relative Calibration on the OAI 5G testbed”, published in 53rd Asilomar Conference on Signals Systems and Computers, 2019.

We also modeled our OpenAirInterface C-RAN testbed through simulations in order to provide a ground truth for the evaluation of the proposed FC scheme using channel measurements. We illustrated that the performance of each grouping scheme is highly sensitive to the geometrical characteristics of the area where the RRUs are distributed. Moreover, we proved, through MSE and condition number metrics, that the overall estimation performance of our group-based FC algorithm improves when we try to minimize the size of the largest RRU group with equally partitioned groups. In general, we established the correctness of the corresponding real-time evaluation made in the work above which was carried out using variance as a metric.

These results are presented in Chapter 6 and published in:

- T. Magounaki, F. Kaltenberger, and R. Knopp, “Modeling the Distributed MU-MIMO OAI 5G testbed and group-based OTA calibration performance evaluation”, published in IEEE 21st International Workshop on Signal Processing Advances in Wireless Communications, 2020.

1.2.2 Testbed for MIMO Antenna Performance Assessment

During the first year of my PhD studies we developed a testbed in order to facilitate the evaluation of relative calibration in a MISO-TDD system and simultaneously assess the performance of the MIMO antenna prototypes designed by our team in Orange labs. The following studies combine a joint effort from colleagues in Eurecom, Orange labs and the CREMANT, joint lab between Orange and the University Nice Sophia Antipolis.

We deployed a testbed inside a controlled laboratory environment and in line-of-sight (LOS) propagation conditions, using the open-source hardware and software development platform OpenAirInterface, ExpressMIMO2 motherboards and a rail moving with a Digital Servo Amplifier, SERVOSTAR 300 along with a Rosier servo motor controlling the movement. We studied the beamforming performance under different CSIT acquisition methods for a 8x1 TDD-MISO system. Our experimental results proved that the applied relative calibration method works in a real environment and over a long time period. Also, we implemented an antenna selection scheme at the transmit side as a low-cost low-complexity alternative to capture many of the advantages of multi-antenna systems.

These results are presented in Subsection 7.2.1 and published in:

- T. Magounaki, F. Kaltenberger, X. Jiang, C. Buey, P. Ratajczak, and F. Ferrero, “Experimental evaluation of relative calibration in a MISO-TDD system”, published in 2017 European Conference on Networks and Communications.

Moreover, we confirmed the effectiveness of our ExpressMIMO2 testbed for assessing MIMO antenna prototypes build with Laser Direct Structuring (LDS) techniques, based on the reproducibility of the signal-to-noise-ratio (SNR) measurements to characterize the beamforming gain.

These results are presented in Subsection 7.2.2 and published in:

- C. Buey, T. Magounaki, F. Ferrero, P. Ratajczak, L. Lizzi and F. Kaltenberger, “MIMO antenna performance assessment based on open source software defined radio”, published in 11th European Conference on Antennas and Propagation, 2017.
- C. Buey, T. Magounaki, F. Ferrero, P. Ratajczak, L. Lizzi and F. Kaltenberger, “Validation of an open source software defined radio test bed”, published in 2017 IEEE International Symposium on Antennas and Propagation.

Finally, we contributed to a work proving that although 5G is based on multi-carrier modulation which is not compatible with spatial modulation, the mobile networks have the potential to support single-carrier modulations, with bandwidths as large as several MHz. We carried out experiments in the same ExpressMIMO2 testbed but in non-line-of-sight (NLOS) propagation conditions.

These results are presented in Subsection 7.2.3 and published in:

- D-T. Phan-Huy, Y. Kokar, K. Rachedi, P. Pajusco, A. Mokh, T. Magounaki, R. Masood, C. Buey, P. Ratajczak, N. Malhouroux-Gaffet and others, “Single-carrier spatial modulation for the internet of things: Design and performance evaluation by using real compact and reconfigurable antennas”, published in Journal IEEE access 7, 2019.

Chapter 2

Massive MIMO and Distributed multi-user MIMO Background

2.1 Fundamentals of MIMO technology

This section briefly reviews the technology of MIMO in wireless communications. With the advancement of wireless technology and the growing need for greater data capacity for mobile networks in 2020 and beyond, it addresses the reasoning behind why MIMO evolves into massive MIMO. Since Shannon formulated the fundamental capacity limits for SISO systems in the late 1940s, wireless data traffic has increased dramatically over the years. In [39] a MIMO patent was proposed, where multiple transmit antennas are co-located at one transmitter with the objective of improving the achievable link throughput. MIMO is an evolving technology that offers considerable increase in data bandwidth without any extra transmission power, and has been accepted as one of key technologies in the 4G wireless communications systems. To achieve capacities unimaginable by SISO systems, MIMO systems effectively exploit fading in a rich scattering environment. MIMO systems can be divided into three categories: single-user MIMO (SU-MIMO) or point-to-point MIMO, multi-user MIMO (MU-MIMO) and massive MIMO.

One of the key enablers of 5G is massive MIMO technology, where the BS is equipped with an excess of antennas to achieve multiple orders of spectral and energy effieciency gains over current LTE networks. This short review primarily follows the content in [8, 10, 40–43].

2.1.1 From SISO to MIMO

Traditional wireless communication systems use a single antenna at the transmitter and a single antenna at the receiver. Such systems are known as single-input single-output (SISO) systems, Fig. 2.1. The SISO communication channel is upper bounded by the Shannon capacity which has the following form for additive white Gaussian noise (AWGN) channels (in bits/sec),

$$C_{SISO} = B \log_2(1 + \rho) \tag{2.1}$$

Figure 2.1 – SISO model [1]

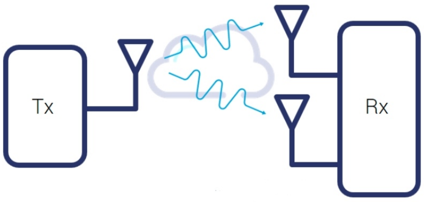

Figure 2.2 – SIMO model (receive diversity or receive beamforming)

where B is known as the bandwidth of the signal and ρ is interpreted as the SNR. (2.1) is known as Shannon capacity formula or Shannon limit [44], an expression (logarithmic function) for how many bits of information can be transmitted without error per second over a channel.

Next, we can have multiple receive antennas and one transmit antenna, a technique referred to as single-input multiple-output (SIMO) and is depicted in Fig. 2.2 or multiple antennas at the transmitter side and only one antenna at the receiver (MISO), Fig. 2.3, which are both special cases of the MIMO technology. The SIMO technique can be used to improve link reliability by combining the received versions of the signal. While in MISO, the transmit antennas are combined to minimize errors and optimize data speed. The transmission of multiple signals can reduce the distortions caused by multipath wave propagation.

Systems with multiple antennas at both ends can be classified as multiple-input multiple-output (MIMO) systems which constructively explore multipath propagation using different transmission paths to the receiver [45]. These paths may be used to provide redundancy of transmitted data, thus enhancing transmission efficiency (diversity gain) or increasing the number of data streams transmitted simultaneously and increasing the system's data rate (multiplexing gain). The multiple spatial signatures can also be

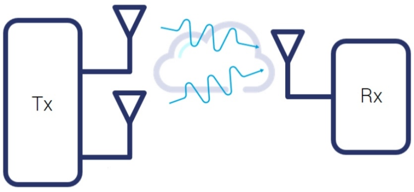

Figure 2.3 – MISO model (transmit diversity or transmit beamforming)

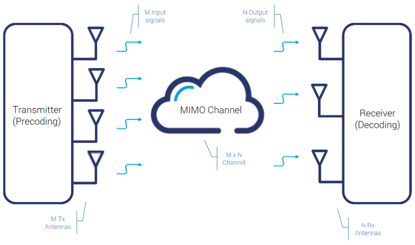

Figure 2.4 – MIMO model

used for combating interference in the system (interference reduction). Fig. 2.4 shows a general model of a wireless MIMO communication system.

On a MIMO system, each antenna operates at the same frequency and thus needs no additional bandwidth. While fading can affect a channel and this will affect the error rate, MIMO's concept is to provide several versions of the same signal to the receiver. There is a substantial reduction in the probability that all these versions will be affected simultaneously and in the same way by the propagation direction. This helps to stabilize a connection and increase capacity by reducing errors. Therefore, MIMO technology is able to significantly increase the capacity of a given channel. Moreover, it is possible to linearly increase the throughput of the channel by increasing the number of transmitting and receiving antenna pairs.

MIMO systems can be generally divided into two broad categories: single-user (SU-MIMO or point-to-point MIMO) or multi-user (MU-MIMO) as depicted in Figure 2.5.

2.1.2 Single-User MIMO

SU-MIMO represents the simplest form of MIMO: a base station equipped with multiple antennas serves a terminal equipped with multiple antennas. Performance improvements in terms of coverage, link reliability and data rate can be achieved by techniques such as beamforming, space-time coding and multiplexing of many data streams. These methods can not be completely used simultaneously, so we usually see a trade-off between them. In LTE, for example, adaptive switching is implemented between spatial diversity and multiplexing schemes [46]. Near the edges of the cell, multiplexing gains disappear where signal levels are low relative to interference or in an environment of propagation that is insufficiently dominated by scattering [8].

We consider a SU-MIMO system which consists of a BS and a UE equipped with M and K antennas respectively. When the channel $M \times K$ is constant, the channel capacity is given by [47],

$$C_{dl} = \max_{\mathbf{Q}:Tr(\mathbf{Q})=P} \log_2 \left| \mathbf{I}_K + \mathbf{H}\mathbf{Q}\mathbf{H}^H \right| \tag{2.2}$$

where the optimization is over the input covariance matrix $\mathbf{Q}$ and P is the power constraint across all transmit antennas at the BS. The optimal signal covariance is achieved through singular value decomposition (SVD) of the matrix $\mathbf{H}$ and the optimal power allocation through waterfilling. Using SVD the channel matrix $\mathbf{H}$ is converted into $\min(M, K)$

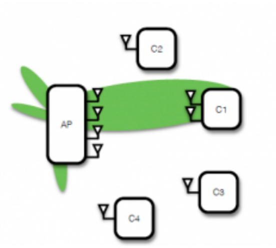

(a) Single-user MIMO
Serves one user at a time.

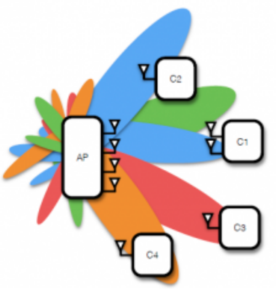

(b) Multi-user MIMO
Serves multiple users simultaneously.

Figure 2.5 – SU-MIMO vs MU-MIMO

parallel non-interfering SISO channels with power gain λ_i^2 which are the singular values of $\mathbf{H}$.

If the BS has no CSI knowledge, the optimal covariance matrix is identity resulting in a waterfilling strategy which allocates equal amounts of power across all the spatial-time modes (eigenmodes), which means $\mathbf{Q} = \frac{1}{M}\mathbf{I}$,

$$C_{dl} = \log_2 \left| \mathbf{I}_M + \frac{\rho_{dl}}{M} \mathbf{H}\mathbf{H}^H \right| \tag{2.3}$$

If the BS has full CSI knowledge, we may perform dynamic power allocation only to the stronger eigenmodes and the capacity is given by,

$$C_{dl} = \sum_{i=1}^{\min(M,K)} \log_2 \left(1 + \frac{P_i \lambda_i^2}{\sigma_n^2} \right) \tag{2.4}$$

where the optimal powers P_i are obtained via waterfilling and σ_n^2 is the noise variance.

In a rich scattering propagation environment such that the matrix of channel gains between transmit and receive antenna pairs has full rank and independent entries, modeled by independent Rayleigh fading, for sufficiently high SNRs, channel capacity scales linearly with $\min(M, K)$ and logarithmically with the SNR. [49] showed that the MIMO channel can be converted into parallel, non-interfering SISO channels through the SVD of the channel matrix. However, in practice, the limited number of antennas at the UE side, the correlation between the channel gains on each antenna element and the line-of-sight (LoS) propagation conditions, make it difficult to achieve $\min(M, K)$ parallel channels. Besides, in the low SNR regime, the capacity increases linearly with the number of receive antennas.

2.1.3 Multi-User MIMO

An alternative to a SU-MIMO system is a MU-MIMO system in which several users are simultaneously served by a multiple-antenna BS. With MU-MIMO technology, a spatial multiplexing gain can be achieved even if each user has a single antenna [50–53]. This is important because, due to the small physical size and low-cost requirements of the terminals, UEs can not support many antennas, while the BS can have a large number of antennas. By using scheduling mechanisms, MU-MIMO overcomes most LOS propagation constraints in MIMO, such as ill-conditioned channels. The wireless channel is now spatially shared by numerous users, and users operate among them without joint encoding and detection. The BS communicates simultaneously to the separated by many wavelengths users by exploiting differences in spatial signatures induced by spatially dispersed users. As a result, performance gains in terms of sum rates of all users can be impressive.

We consider a MU-MIMO system which consists of one BS and K active users. The BS is equipped with M antennas, while each user has a single-antenna. We assume that all K users share the same time-frequency resource. Furthermore, we assume that the BS and the users have perfect knowledge of the CSI acquired during the training phase. Let $\mathbf{H} \in \mathbb{C}^{M\times K}$ be the channel matrix between the K users and the BS antenna array, where the kth column of $\mathbf{H}$, denoted by $\mathbf{h}_k$, represents the $M \times 1$ channel vector between the kth user and the BS. Again, we ignore large-scale fading, and assume that the elements of $\mathbf{H}$ are i.i.d. Gaussian distributed with zero mean and unit variance [54]. The DL sum-capacity is given by,

$$C_{dl} = \max_{\mathbf{v}} \log_2 \left| \mathbf{I}_M + \rho_{dl} \mathbf{H} \mathbf{D}_{\mathbf{v}} \mathbf{H}^H \right| \tag{2.5}$$

$\mathbf{D}_{\mathbf{v}} = \mathrm{diag}\{v_1, v_2, \cdots, v_K\}$ with $v_k \geq 0$ and $\sum_{k=1}^{K} v_k \leq 1$ is the power allocation strategy at the BS. Note that, assuming an equal power allocation constraint at the BS, $\mathbf{D}_{\mathbf{v}} = \frac{1}{M}\mathbf{I}_K$, (2.5) collapses to (2.3).

2.1.4 Evolution of MIMO towards Massive MIMO

Massive MIMO (also knows as very large MU-MIMO, hyper MIMO, full-dimension MIMO (FD-MIMO), and ARGOS), introduced in the pioneering work in [8], is an extension of MU-MIMO technology where K UEs are serviced on the same time-frequency resources by a base station with M antennas, such that $M \gg K$, and operates in TDD mode using linear uplink and downlink processing, Fig. 2.6.

The fundamental advantages of massive MIMO over the MU-MIMO technology can be summarized as follows:

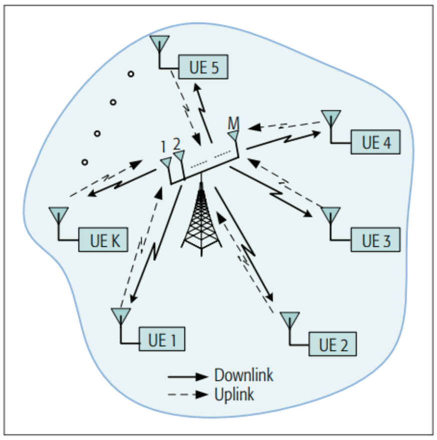

Figure 2.6 – Massive MIMO model

- ***Scalability***: With FDD, the channel estimation overhead depends on the number of BS antennas, M. By contrast, with TDD, the channel estimation overhead is independent of M. In Massive MIMO, M is very large, and hence, TDD operation is preferable. By operating in TDD mode and relying on reciprocity between the uplink and downlink channels, the amount of resources needed for pilots only depends on the number of simultaneously served terminals K and not on the large number of BS antennas. This renders Massive MIMO entirely scalable with respect to the number of BS antennas, M.

- ***Channel hardening and favorable propagation***: Both phenomena are consequences of the law of large numbers. If the channel hardens, the sum-capacity does not depend on the small-scale fading which is averaged out since there are many antennas with similar channel gains. This property simplifies the power allocation, system scheduling and interference management which can be done over the large-scale fading variations only. Therefore, the overhead for these system designs is significantly reduced. Moreover, there is no need for instantaneous CSI knowledge at the receiver side. The receiver needs only the statistical knowledge of the channels gains in order to detect the transmitted signals. Thus, the resources (power and training duration) required for channel estimation are significantly reduced, [55, 56].

  The massive MIMO channel, under some conditions and a large excess of antennas can offer asymptotically favorable propagation, defined as mutual orthogonality among the vector-valued channels to the terminals. The great spatial resolution will likely make the channels to different users nearly orthogonal, meaning that the propagation channel responses from the BS to different terminals are sufficiently different. This is favorable since there will be little interference leakage between the users.

- ***Linear processing***: Linear processing can reach optimal performance with favorable propagation. More specifically, noise and interference can be canceled out on the UL, with a simple linear detector such as the matched filter, which separates the signals transmitted by the various terminals. On the DL, with linear beamforming techniques, the BS can simultaneously beamform multiple data streams to multiple terminals without causing mutual interference.

We consider the uplink transmission under favorable propagation conditions where $\mathbf{H}\mathbf{H}^H = \mathbf{I}$ holds, the sum-capacity is given by [55],

$$C_{sum} = \log_2 \det(\mathbf{I}_K + \rho_u M \mathbf{I}_K) = K \log_2(1 + M\rho_u) \tag{2.6}$$

where K is the multiplexing gain and M represents the array gain. We notice that by scaling M and K, the spectral and energy efficiency are increased, without any increase in transmitted power per terminal. Also, by increasing K and M, we can simultaneously serve more users in the same frequency band and at the same time increase the throughput per user.

Many concerns still need to be investigated, considering the tremendous benefits of Massive MIMO. Some of the primary challenges are described as follows:

- ***Pilot contamination***: A fundamental problem where if each cell is serving the maximum number of terminals then the pilot signals received by a BS are contaminated by pilots transmitted by terminals in other cells, since many cells have to share the same time-frequency resources from a limited availability of frequency spectrum. Ideally, every terminal in a massive MIMO system is assigned an orthogonal uplink pilot sequence. However, the maximum number of orthogonal pilot sequences that can exist is upper-bounded by the duration of the coherence interval divided by the channel delay spread. For example, the maximum number of orthogonal pilot sequences in a 1ms coherence interval is estimated to be about 200, [8]. Therefore, it is easy to exhaust the available supply of orthogonal pilot sequences in a multicellular system.

- ***Channel reciprocity***: Massive MIMO operates in TDD mode which relies on the channel reciprocity to acquire the DL CSI based on UL channel estimation. However, as the transmit and receive hardware in transceivers are not symmetric, reciprocity calibration is essential for CSIT acquisition. Calibrating massive MIMO and maintaining the system in a calibrated status is an important topic and will be the focus of this thesis.

- ***Unfavorable propagation***: Massive MIMO is based on the premise that as the number of BS antennas grows, the individual user channels are spatially uncorrelated and their channel vectors asymptotically become pairwise orthogonal under favorable propagation conditions. However, in practice, there may be propagation environments where the channels are not favorable. For example, in propagation environments where the numbers of the scatterers is small compared to the numbers of users, or the channels from different users to the BS share some common scatterers, the channel is not favorable, [57]. One possibility to tackle this problem is to distribute the BS antennas over a large area. This will also resolve the processing of huge amounts of data in real time and renders possible the distribution of the calculation to different modules with low-complexity signal processing algorithms. Furthermore, in some propagation environments, such as keyhole channels, channel hardening does not hold, [55]. A keyhole channel (or double scattering channel) appears in scenarios with rich scattering around the transmitter and receiver, and where there is a low-rank connection between the two scattering environments. The keyhole effect can occur when the radio wave goes through tunnels, corridors, or when the distance between the transmitter and receiver is large, [58–61].

2.2 Fundamentals of Distributed Massive MIMO

Distributed massive MIMO or distributed antenna system (DAS) with spatially separated antennas is considered for improving indoor coverage with not so large number of antennas [62]. It gives a higher spectral efficiency and enhanced coverage area especially for users at the cell edge, compared to co-located massive MIMO. Distributed multi-user MIMO (MU-MIMO) unifies small cells and massive MIMO approaches. Simultaneously obtaining both multi-user interference suppression through spatial precoding, and dense coverage by reducing the average distance between transmitters and receivers. These distributed antennas are also called access points (APs). More specifically, several access points (APs), distributed over a certain coverage region, can be connected to a central server and operate as a large distributed multi-antenna AP, ensuring that all transmitted signal power serves the purpose of data transmission, rather than creating “interference”.

The cell-free massive MIMO network infrastructure, depicted in Fig. 2.7 has been proposed in [11, 63] as a beneficial form of the general distributed massive MIMO concept but without cells or cell boundaries. By relying on time-division duplex (TDD) operation, a large number of geographically distributed antennas jointly serve a lower number of UEs with the aid of a fronthaul network and a central processing unit (CPU) operating in the same time-frequency resource. More explicitly, a large number of distributed access points (APs) employing single or multiple antennas simultaneously serve all UEs by exploiting local CSI and performing joint transmission. The CPU sends the downlink (DL) data and power control coefficients to the APs, while the APs feed back the data received from the UEs in the uplink (UL) to the CPU via fronthaul link. In cell-free massive MIMO, only the channel statistics are utilized at the CPU to apply joint detection with good performance.

Nevertheless, in practice, there are some important issues to be addressed in order to deploy a distributed massive MIMO system. Those are the synchronization of distributed local oscillators, amplifier non-linearities, non-ideal analog filters and the critical TDD channel reciprocity.

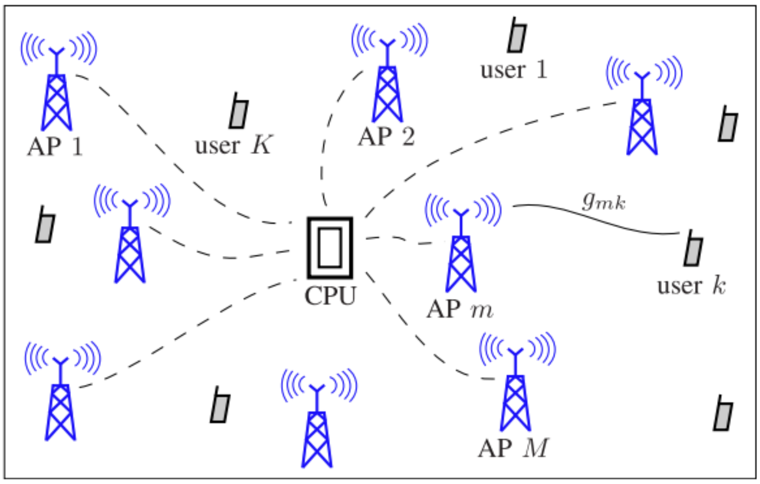

Figure 2.7 – Cell-Free Massive MIMO system

2.3 TDD Reciprocity Calibration

TDD is a duplex method by which the uplink (UL) and the downlink (DL) transmissions are carried over the same frequency using synchronized time intervals. Hence, since the UL and DL channels are reciprocal the BS can acquire knowledge of the channel just through UL channel estimates. The DL channel in a real-world system is split into three components:

1. The over-the-air (OTA) channel.
2. The hardware response of the BS transmit RF paths.
3. The hardware response of the user receive RF paths.

Although the assumption of reciprocity applies for the over-the-air interface, it does not hold for the paths of the hardware. Because of mismatched traces, poor synchronization between the RF paths, and temperature-related phase drifts, the RF signal chains introduce inaccuracies into the system [64].

The existing calibration methods can be classified into two categories:

- *Absolute Calibration*: Additional hardware is used to perform the calibration separately in the transmitter and the receiver [18].
- *Relative Calibration*: Signal processing techniques are used (less costly).

As a result of the intrinsic imperfections in several different hardware components comprising the front ends of the RF transceiver, such as amplifiers, converters, mixers, filters and oscillators, RF impairments occur [65, 66]. The three main types of RF impairments are I/Q imbalance, oscillator phase noise, and high-power amplifier (HPA) nonlinearities [67]. I/Q imbalance refers to the amplitude and phase mismatch between the in-phase (I) and quadrature (Q) signal branches, i.e., the mismatch between the real and imaginary parts of the complex signal. Oscillator phase noise refers to the noise in an oscillator, mainly due to the active devices in the oscillator circuitry, which introduces phase-modulated noise, directly affecting the frequency stability of the oscillator [68]. The HPA nonlinearities refer to the operation of the HPA in its nonlinear region when working at medium- and high-power signal levels. The influence of these RF impairments is usually mitigated by suitable compensation algorithms, which can be implemented by analog and digital signal processing.

Relative or OTA calibration can be classified as *partial calibration* and *full calibration*. In partial calibration only the radio frequency (RF) mismatches at the BS are calibrated. While, the full calibration compensates for the RF mismatches at both the BS and the user equipments (UEs). Full calibration parameters are estimated based on bidirectional channel measurements. This requires heavy feedback in a massive MIMO context, thus making this approach unsuitable. Actually, in [69] it is shown that the RF mismatches at the BS are the major factor for degrading the system's performance. As a result, the most essential element is the calibration at the BS and not at the UE side.

A few prior works have offered solutions for efficient channel calibration in TDD systems [70], [25]. The authors in [23] proposed to use multiplicative matrices to compensate the hardware non-symmetry. Nonetheless, the above solutions require terminal involvement and feedback in the calibration phase, resulting in an unacceptable overhead in large-scale MIMO. In contrast, the relative calibration in Argos [27] is done internally at the BS without such overhead. Specifically, one of the antennas can be treated as a reference and signals can be traded between the reference antenna and each of the other antennas to derive a compensation factor for that antenna. Moreover, a fast calibration method Avalanche is proposed in [31]. The principle is to use a calibrated subset of antenna elements to calibrate the uncalibrated ones. Hence, the calibrated array grows during the calibration process in a way similar to the phenomenon of avalanche. In [32], the authors provide a unified framework for OTA reciprocity calibration in a TDD system using antenna partition. They present different ways to partition the array into transmit and receive elements during successive training phases yielding different schemes. Finally, they propose a novel calibration scheme based on antenna grouping, which can greatly speed up the calibration process. In [28], the authors extended the Argos method to a distributed multi-user MIMO (MU-MIMO) network where the calibration is performed among non-collocated antenna arrays. The least-squares (LS) estimator was generalized in order to calibrate large-scale distributed MIMO networks. To improve the calibration performance, the LS method does not only rely on the reference antenna, but utilizes the received calibration signals of all antennas.

2.4 Distributed 5G network: Open RAN architecture

Nowadays, with the increasing number of mobile internet technology, telecommunications operators are faced with huge pressure on the increasing number of operating expenses with much less growth in their income. In order to support user needs, such growth would require more and more base stations, which would be really costly to deploy and manage.

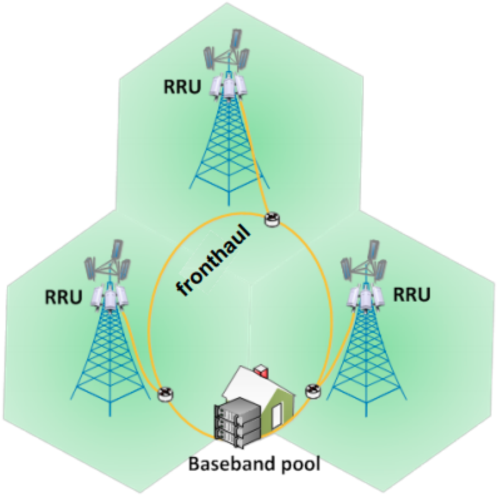

Figure 2.8 – Generic C-RAN architecture

The Cloud Radio Access Network (C-RAN) and its derivatives have been recognized as one of the possible technologies capable of meeting the underlying 5G technological radio access requirements [71, 72].

C-RAN [73, 74] refers to a cellular network architecture which separates the RAN functionalities from the hardware and transfers them to software, introducing virtualization of the network resources to enable a centralized radio resource management. The C-RAN architecture consists of three building blocks, i.e. baseband units (BBUs) located in the cloud, remote radio units (RRUs) acting as remote antenna elemets and fronthaul links that interconnect the BBUs and the RRUs, Fig. 2.8. Different network nodes may utilize different parts of the available resources, i.e. the BBU pool, allowing an efficient network adaptation to heterogeneous traffic types and loads. New BBUs can be easily added, improving the scalability and easing the network maintenance. The RRU is separated from the BBU. Compared to a traditional BS (where the RRU and BBU are coupled together) it improves the network resource sharing. It is possible to connect a very large number of RRUs via high-speed fronthaul (usually fiber optics) to a single BBU. C-RAN also helps networks to become programmable, adaptable, cost effective and centrally controlled. Moreover, C-RAN has drawn significant attention as the emerging architecture of future generation cellular networks, due to its noticeable performance benefits for cellular operators [75]. In C-RAN, each RRU uses high bandwidth, low latency fronthaul links to forward the user information to the central cloud processor and thus relies on the BBU pool to perform the compute-intensive baseband functions.

The C-RAN has recently begun to evolve towards the Open-RAN (O-RAN) concept [76]. By focusing on Openness and Intelligence, O-RAN supports more accessible and smarter radio access networks. To address the complexity issues, operators and vendors cannot rely on conventional human intensive means of deploying, optimizing and operating the mobile networks. Instead, emerging intelligence-based technology such as Machine

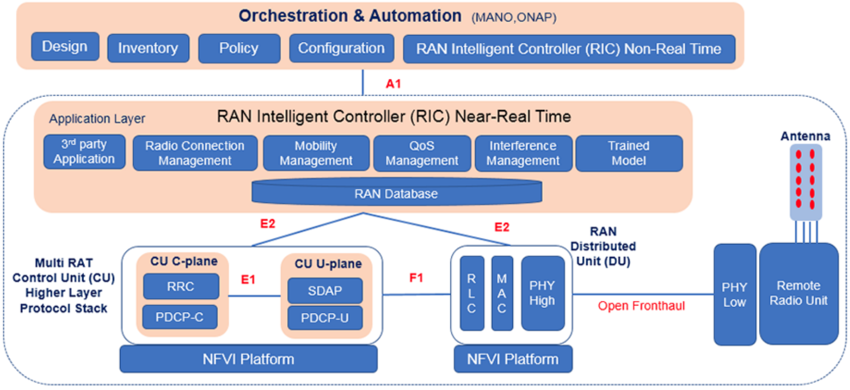

Figure 2.9 – O-RAN Alliance Reference Architecture

Learning (ML) and Artificial Intelligence (AI) must be able to enable mobile networks in order to simplify network operations and reduce functioning costs. O-RAN Alliance, established in February 2018, is creating a full reference architecture for open hardware to create a virtualized RAN. An open and interoperable supply chain ecosystem will be allowed by standardized interfaces [77]. Several technical working groups cover various subjects, including overall architecture, open midhaul and fronthaul interfaces, intelligent RAN controller and AI interface, and the hardware and software white-box architecture required for 5G New Radio (NR) [78]. The Open RAN reference architecture that the O-RAN alliance is creating is shown in Fig. 2.9.

O-RAN specification provides guidance about the split of the gNB into three main functional modules: the Centralized Unit (CU), the Distributed Unit (DU) and the Remote Radio Unit (RRU), Fig. 2.10. CU is the centralized unit that runs the radio resource control (RRC) and packet data convergence protocol (PDCP) layers and controls the operation of several DUs over the middlehaul interface which may be up to $20-40$ km. The distributed unit that is next to the RRU and controls it, is called the DU. The DU is responsible for the radio link control (RLC) layer, the media access control (MAC) layer and parts of the physical layer (PHY layer). Its operation is controlled by the CU. Fronthaul connects the DU with the RRU within a distance of $1-20$ km away. Finally, RRU is the remote radio unit that handles parts of the PHY layer, as well as the digital beamforming functionality. Backhaul connects the 5G core to the CU and can be up to 200 km away.

2.4.1 Fronthaul Synchronization Challenges

In this subsection we present the importance of timing synchronization for the fronthaul architectures. The term timing synchronization refers to the transportation and distribution of phase/time synchronization through the fronthaul transport in order to precisely synchronize the O-RAN radio units [79]. Synchronizing clocks in distributed cloud-native edge networks has been a long-standing problem. Accurate clocks enable applications to operate on a common time axis across the different nodes and locations, which in turn

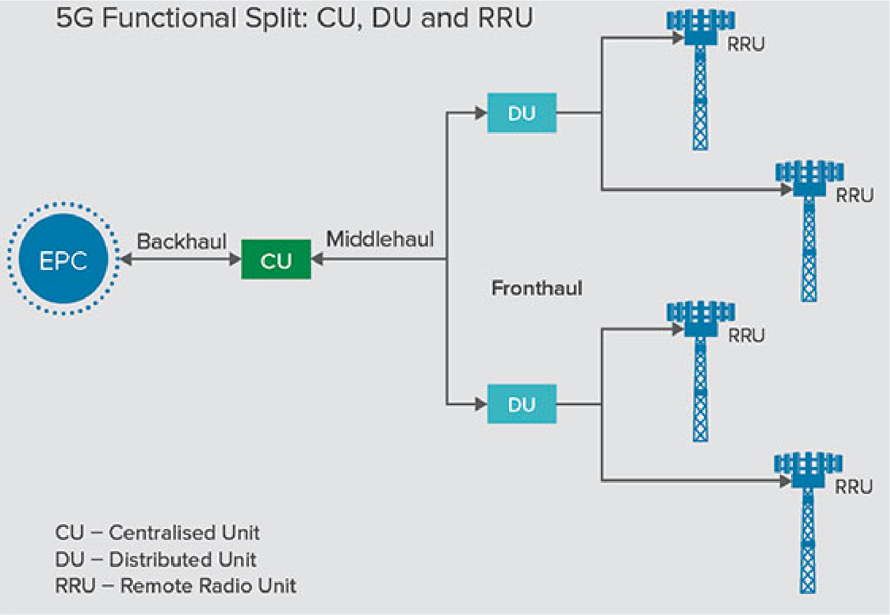

Figure 2.10 – 5G RAN functional units

precisely and accurately enables consistency, event ordering, causality, and scheduling of tasks and resources. To allow several different UEs to connect simultaneously and to sustain their connections as they travel between RRUs, extreme precision is required by the mobile networks [80].

Accurate synchronization improves over-the-air radio performance, which is directly linked to the time alignment error (TAE) between two adjacent RRUs. As a result, the RRUs that are not precisely synchronized in the O-RAN architecture will result in variations in carrier frequency that would result in random phase noise in turn. This directly conduces to poor radio performance at the air interface. RRUs are equipped with Local Oscillators (LOs) which must be locked to a particular reference frequency at a given time, in order for the RRUs to be precisely synchronised to each other. Over the period of time, the accuracy levels with which these LOs must be locked has evolved. In particular in the context of 5G, the accuracy values are extremely strict. For example, the deployment of coordinated RAN features such as CoMP requires relative time sync $\leq 1\mu$s (synchronization between neighbor radios) and beamforming with NR-TDD needs absolute time sync $\sim 1.5\mu$s [81]. Moreover, highly accurate synchronization between RRUs is required in order to achieve TDD, Carrier Aggregation (CA)[1], MIMO, and other processes.

From a transport network point of view, the current fronthaul transport is represented by Common Public Radio Interface (CPRI). However with regards to 5G, Ethernet-based fronthaul transport is pushed strongly by operators, due to the existing limitations in CPRI to support 5G data rate, as well as due to the presence of Ethernet equipment

---

[1] A technology that expands bandwidth and achieves high-speed transmission by performing simultaneous transmission and reception on multiple component carriers.

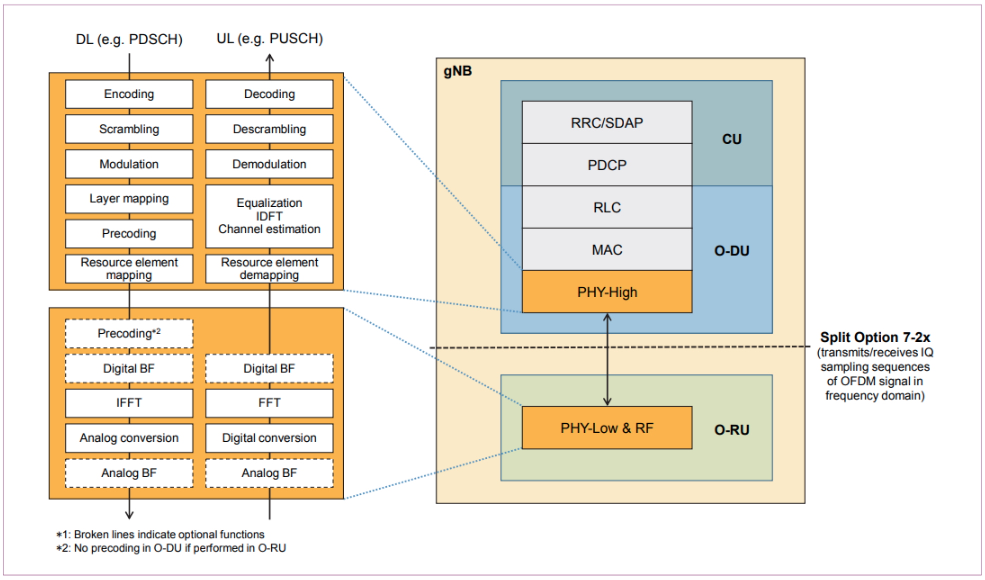

*1: Broken lines indicate optional functions
*2: No precoding in O-DU if performed in O-RU

Figure 2.11 – Functional split option 7-2x.

in operator transport networks. Nevertheless, in contrast to CPRI, Ethernet does not support synchronization [82].

In 5G RAN transport, the most challenging interface is between the DU and RU. The RU offers functions such as ADC, filtering, amplification of power and is combined with antennas. Including signal modulation, encoding and scheduling, the DU provides digital processing. Usually using CPRI, the two systems are closely linked through the fronthaul [83]. CPRI was designed for fiber runs for the base of a cell tower to a tower-mounted remote radio head covering a few tens of meters, but has since been extended over long distances (up to tens of kilometers) to enable centralized RAN architectures. The challenges with CPRI over long distances are that it is very demanding on transport and requires wavelengths or dark fiber pairs and it does not scale well to massive MIMO. The large bandwidth demands of CPRI-based fronthaul and the high cost of infrastructures needed to support them have limited the deployability of Cloud RAN architectures. On account of this bandwidth problem, O-RAN fronthaul specifications include a new functional splitting requirement called split option 7-2x which places certain physical layer functions that were previously located in the baseband processing unit in radio equipment [84]. An overview of split option 7-2x is shown in Fig. 2.11.

Furthermore, O-RAN introduces Control, User and Synchronization Plane (C/U/S-Plane) specifications. The C-Plane and U-Plane are protocols for transferring control signals and user data, respectively. The S-Plane is the protocol for achieving synchronization between multiple radio units. In the C/U-Plane, the O-RAN fronthaul specifications support a protocol stack that transmits signals used by eCPRI[2] or Radio over Ethernet

---

[2] Enhancement to run CPRI over switched Ethernet. Offers 10x reduction in bandwidth compared to CPRI.

(RoE) directly over Ethernet. The eCPRI payload of the C-Plane message passed from the DU to RU consists of information specifying beamforming weights to be applied when transmitting and receiving IQ samples sequences included in the U-Plane message on the radio interface. It also consists of time/frequency resource information to which the above beamforming weights are to be applied. The RU uses this information to generate a beam for transmitting and receiving signals on the radio interface. The eCPRI payload of the U-Plane message is used to transmit identification information for radio frame, subframe, slot and OFDM symbol or frequency resource information for the Physical Resource Block (PRB) start position and number of PRBs. In S-Plane, O-RAN fronthaul specifications support protocols such as PTP[3] and SyncE[4] to achieve high-accuracy synchronization on the RRU side by synchronizing with the clock on the high-performance DU side.

2.5 Summary

In this chapter, we reviewed the fundamentals of the MIMO technology and the capacity limits on different categories of MIMO systems. Also, we discussed about the evolution of MIMO towards massive MIMO and we pointed out the advantages and challenges you have to face when operating in systems equipped with an excess of antennas. Finally, we referred to the gains of distributed massive MIMO compared to the co-located case and how to deploy such a system.

---

[3] A protocol for achieving high-accuracy time synchronization among equipment connected to a network.

[4] A system for transmitting clock signals on the Ethernet.

Chapter 3

State of the art on OTA reciprocity calibration techniques

3.1 System Model

We consider a TDD communication system involving a BS A and a UE B with M_A antennas and M_B antennas respectively, illustrated in Fig. 3.1. The channel seen by transceivers in the digital domain (the composite channel), is comprised of the physical channel $\mathbf{C}$, assumed reciprocal in both UL and DL, and filters modeling the imperfections of the transmit RF hardware (e.g., power amplifiers (PA)), ($\mathbf{T}_A$ and $\mathbf{T}_B$), and the receive RF hardware (e.g, low-noise amplifiers (LNA)), ($\mathbf{R}_A$ and $\mathbf{R}_B$). The diagonal elements represent the gains on each transmit chain whereas the off-diagonal elements correspond to the RF chain on-chip crosstalk and the antenna mutual coupling. We consider the ideal case, where the transmit/receive RF hardware are all diagonal filters (no crosstalk/mutual coupling) and carrier frequency at both sides is identical. Also, the filters modeling the amplifiers are assumed to remain constant over the observed quite long time horizon. The measured UL and DL channels between nodes A and B, represented by $\mathbf{H}_{A\to B}$ and $\mathbf{H}_{B\to A}$, are thus modeled as:

$$\begin{aligned}\boldsymbol{H}_{A\to B} &= \boldsymbol{R}_B \boldsymbol{C}_{A\to B} \boldsymbol{T}_A \\ \boldsymbol{H}_{B\to A} &= \boldsymbol{R}_A \boldsymbol{C}_{B\to A} \boldsymbol{T}_B\end{aligned} \tag{3.1}$$

Since we operate within the channel coherence time we can eliminate the physical channel $\mathbf{C}$ from (3.1) and we obtain:

$$\boldsymbol{H}_{A\to B} = \boldsymbol{F}_B^{-T} \boldsymbol{H}_{B\to A}^T \boldsymbol{F}_A \tag{3.2}$$

where $\boldsymbol{F}_A = \boldsymbol{R}_A^{-T} \boldsymbol{T}_A$ and $\boldsymbol{F}_B = \boldsymbol{R}_B^{-T} \boldsymbol{T}_B$ include the hardware properties and are called the *calibration matrices.*

OTA calibration relies on signal processing techniques to calibrate at RF chain level and compensate the hardware non-symmetry. Thus, we estimate $\boldsymbol{F}_A$ and $\boldsymbol{F}_B$ which along with the UL channel estimates $\boldsymbol{H}_{B\to A}$ give us the CSIT $\boldsymbol{H}_{A\to B}$, (3.2), based on which advanced beamforming techniques can be implemented. In [85] it is shown that the RF

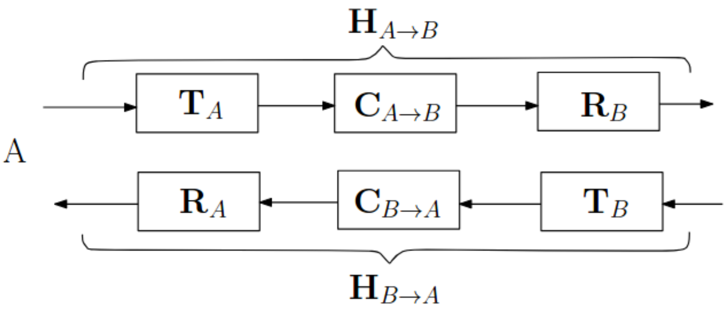

Figure 3.1 – Reciprocity Model

mismatches at the BS, and not at the UE side, are the major factor for degrading the system's performance. Hence, we perform *partial calibration* which is part of the relative or over-the-air (OTA) calibration methods. In partial calibration only the RF mismatches at the BS are calibrated. This has no impact at the beamforming performance as any unknown complex scalar factor is compensated by the channel estimation at the UE. We thus, in Section 3.2, focus on the estimation of $\mathbf{F}_A$, although the framework discussed in the following is not limited to this case.

3.2 Group-based Calibration Scheme

This is a review of the work held in [32] in which the authors proposed a fast calibration method based on antenna grouping in a collocated array. We extended this proposed group-based calibration scheme to a distributed MIMO framework and substituted the antennas with single-antenna RRUs.

Let as describe how the calibration matrix $\boldsymbol{F}_A$ (from 3.1) is estimated based on the fast calibration scheme proposed in [32]. We consider a set of M RRUs partitioned into G groups denoted by $A_1, A_2, \ldots, A_G$, as in Fig. 3.2. Group A_i contains M_i RRUs such that $\sum_{i=1}^{G} M_i = M$. Each group A_i transmits a sequence of L_i pilot symbols, defined by matrix $\mathbf{P}_i \in \mathbb{C}^{M_i \times L_i}$ where the rows correspond to antennas and the columns to successive channel uses. A channel use is considered as a calibration symbol or a frame. When an antenna group i transmits, all other groups are considered in receiving mode. After all G groups have transmitted, the received signal for each resource block of bidirectional transmission between antenna groups i and j is given by

$$\begin{aligned}\mathbf{Y}_{i\to j} &= \mathbf{R}_j\mathbf{C}_{i\to j}\mathbf{T}_i\mathbf{P}_i + \mathbf{N}_{i\to j}\\ \mathbf{Y}_{j\to i} &= \mathbf{R}_i\mathbf{C}_{j\to i}\mathbf{T}_j\mathbf{P}_j + \mathbf{N}_{j\to i}\end{aligned} \tag{3.3}$$

where $\mathbf{Y}_{i\to j} \in \mathbb{C}^{M_j \times L_i}$ and $\mathbf{Y}_{j\to i} \in \mathbb{C}^{M_i \times L_j}$ are received signal matrices at antenna groups j and i respectively. $\mathbf{N}_{i\to j}$ and $\mathbf{N}_{j\to i}$ represent the corresponding received noise matrix. $\mathbf{T}_i$, $\mathbf{R}_i \in \mathbb{C}^{M_i \times M_i}$ and $\mathbf{T}_j$, $\mathbf{R}_j \in \mathbb{C}^{M_j \times M_j}$ represent the effect of the transmit and receive RF front-ends of antenna elements in groups i and j respectively.

The reciprocity property induces that $\mathbf{C}_{i\to j} = \mathbf{C}_{j\to i}^T$, thus for two different groups $1 \leq i \neq j \leq G$ in (3.3), by eliminating $\mathbf{C}_{i\to j}$ we have

$$\mathbf{P}_i^T \mathbf{F}_i^T \mathbf{Y}_{j\to i} - \mathbf{Y}_{i\to j}^T \mathbf{F}_j \mathbf{P}_j = \widetilde{\mathbf{N}}_{ij} \tag{3.4}$$

The reciprocity calibration matrix $\mathbf{F}$ can be assumed diagonal [23, 24] and thus we can consider $\mathbf{F}_i = \text{diag}\{\mathbf{f}_i\}$ and $\mathbf{F} = \text{diag}\{\mathbf{f}\}$. This allows us to vectorize (3.4) into

$$(\mathbf{Y}_{j\to i}^T * \mathbf{P}_i^T)\mathbf{f}_i - (\mathbf{P}_j^T * \mathbf{Y}_{i\to j}^T)\mathbf{f}_j = \tilde{\mathbf{n}}_{ij} \tag{3.5}$$

where $*$ denotes the Khatri–Rao product, where we have used the equality $\text{vec}(\mathbf{A}\,\text{diag}(\mathbf{x})\,\mathbf{B}) = (\mathbf{B}^T * \mathbf{A})\,\mathbf{x}$. Stacking equations (3.5) for all $1 \leq i < j \leq G$ yields

$$\boldsymbol{\mathcal{Y}}(\mathbf{P})\mathbf{f} = \tilde{\mathbf{n}} \tag{3.6}$$

with $\boldsymbol{\mathcal{Y}}(\mathbf{P})$ defined as

$$\underbrace{\begin{bmatrix} (\mathbf{Y}_{2\to 1}^T * \mathbf{P}_1^T) & -(\mathbf{P}_2^T * \mathbf{Y}_{1\to 2}^T) & 0 & \cdots \\ (\mathbf{Y}_{3\to 1}^T * \mathbf{P}_1^T) & 0 & -(\mathbf{P}_3^T * \mathbf{Y}_{1\to 3}^T) & \cdots \\ 0 & (\mathbf{Y}_{3\to 2}^T * \mathbf{P}_2^T) & -(\mathbf{P}_3^T * \mathbf{Y}_{2\to 3}^T) & \cdots \\ \vdots & \vdots & \vdots & \ddots \end{bmatrix}}_{(\sum_{j=2}^{G}\sum_{i=1}^{j-1} L_i L_j)\times M} \tag{3.7}$$

The estimation of the calibration coefficients $\mathbf{f}$ consists in solving a LS problem assuming a unit norm constraint such as

$$\hat{\mathbf{f}} = \arg\min_{\mathbf{f}:\|\mathbf{f}\|=1} \|\boldsymbol{\mathcal{Y}}(\mathbf{P})\,\mathbf{f}\|^2 \;=\; V_{min}(\boldsymbol{\mathcal{Y}}(\mathbf{P})^H \boldsymbol{\mathcal{Y}}(\mathbf{P})) \tag{3.8}$$

where $V_{min}(\mathbf{X})$ denotes the eigenvector of matrix $\mathbf{X}$ corresponding to its eigenvalue with the smallest magnitude.

3.3 Existing calibration techniques

Different ways of partitioning the M RRUs and choosing the required number of pilots, generate different calibration algorithms. All RRUs have one antenna and form the base station. We assume that the channel is constant during the whole calibration process and we derive from (3.4) different estimators of the calibration matrix. In the following we will interpret every calibration scheme designed for antenna arrays to RRU groups, for the scope of our work.

3.3.1 The Argos calibration method

The Argos base station architecture [27] proposes an internal calibration algorithm to enable distributed beamforming with channel estimation cost independent of the number of base station antennas. It consists in performing bi-directional transmission between a

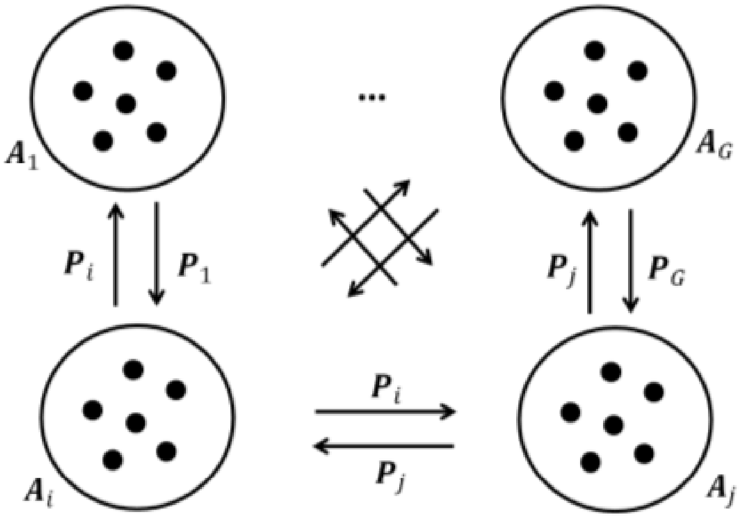

Figure 3.2 – Bi-directional transmission between RRU groups.

carefully chosen reference antenna and the rest of the antenna array. This can be recast in our framework by considering $G = 2$ groups of RRUs, with group A_1 containing only the reference RRU, i.e., $M_1 = 1$ and group A_2 containing all other RRUs with $M_2 = M - 1$, as shown in Fig. 3.3. In slot 1, pilot 1 is broadcasted from the master RRU to all RRUs in set A_2, thus $L_1 = 1$, $\mathbf{P}_1 = 1$ and $\mathbf{f}_2 = \begin{bmatrix} f_2, \ldots, f_M \end{bmatrix}^T$. From slot 2 to slot M, RRUs in group A_2 successively transmit pilot 1 to the reference RRU, thus $L_2 = M - 1$ and $\mathbf{P}_2 = \mathbf{I}_{M-1}$. (3.5) thus becomes

$$f_1 \mathbf{y}_2^T = \mathrm{diag}(\mathbf{y}_1^T)\mathbf{f}_2 + \tilde{\mathbf{n}}, \tag{3.9}$$

where $\mathbf{y}_1 = \begin{bmatrix} y_{1\to 2} & y_{1\to 3} & \ldots & y_{1\to M} \end{bmatrix}^T$ and $\mathbf{y}_2 = \begin{bmatrix} y_{2\to 1} & y_{3\to 1} & \ldots & y_{M\to 1} \end{bmatrix}^T$ with $y_{i\to j}$ representing the signal transmitted from RRU i and received at RRU j. (5.5) can be decomposed into $M - 1$ independent equations as

$$f_1 y_{i\to 1} = f_i y_{1\to i} + \tilde{n}_i, \tag{3.10}$$

where $\tilde{n}_i$ is the i^{th} element in the noise vector $\tilde{\mathbf{n}}$. The LS estimator for each element is thus given by

$$f_i = f_1 \frac{y_{i\to 1}}{y_{1\to i}}, \quad \text{where } i = 2, 3, \ldots, M. \tag{3.11}$$

The performance of different calibration schemes is affected by the SNR value between antennas/RRUs. The Argos calibration algorithm requires a careful placement of the reference antenna such that it can have high enough SNR with every other antenna for effective calibration.

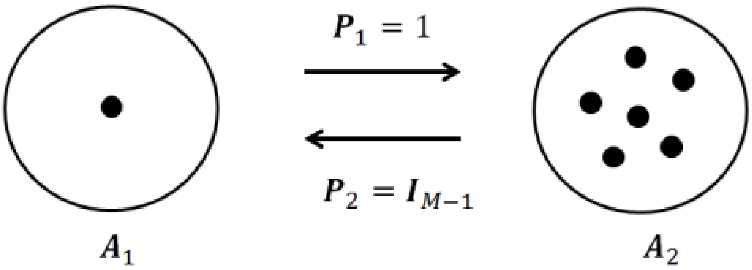

Figure 3.3 – Bi-directional transmission between master RRU and the rest of the RRUs.

3.3.2 The Rogalin calibration method

The method of Rogalin et al. for reciprocity calibration presented in [86], [28] and [30] proposes channel sounding based on mutual coupling with over-the-air measurement between adjacent antennas. Relative calibration using mutual coupling requires sequential channel sounding over different pairs of transmit and receive chains in order to avoid mutual interference. All received signals are subsequently taken into account through joint estimation of the calibration parameters. In order to represent this method within the group-based calibration framework, we define each group A_i as containing antenna i, i.e., $M_i = 1$ for $1 \leq i \leq M$, as in Fig. 3.4.

Since we assume that the channel is constant, this calibration procedure can be performed in a way that antennas can broadcast pilot 1 in a round-robin manner to all other antennas. In total, M channel uses are needed to finish the transmission, making the pilots to be $\mathbf{P}_i = 1$ (with $L_i = 1$). With these pilot exchanges, and under the assumption that the calibration matrix is diagonal, (3.4) degrades to

$$f_i y_{j\to i} = f_j y_{i\to j} + \tilde{n}. \tag{3.12}$$

Note that the calibration coefficient in [28] is defined as the inverse of that in the current chapter, in order to ease the comparison, we let $u_i = f_i^{-1}$ and rewrite (3.12) as

$$u_i^{-1} y_{j\to i} = u_j^{-1} y_{i\to j} + \tilde{n}. \tag{3.13}$$

Estimating $\mathbf{u} = \begin{bmatrix} u_1 & u_2 & \dots & u_M \end{bmatrix}^T$ may be performed by solving the minimization problem

$$\hat{\mathbf{u}} = \arg \min_{u_1, u_2, \dots, u_M} \sum_{i<j} |u_j y_{j\to i} - u_i y_{i\to j}|^2, \tag{3.14}$$

which is the same as defined in [86]. By fixing $u_1 = 1$, the solution of (3.14) is given by

$$\hat{\mathbf{u}} = -(\mathbf{A}_1^H \mathbf{A}_1)^{-1} \mathbf{A}_1^H \mathbf{a}_1 u_1, \tag{3.15}$$

where $\mathbf{A} = [\mathbf{a_1} | \mathbf{A}_1]$, with $\mathbf{a}_1$ representing the first column and $\mathbf{A}_1$ the remaining columns, and $\mathbf{A}$ is given by

$$A_{i,j} = \begin{cases} \sum_{k \neq i} |y_{k\to i}|^2 & \text{for } j = i, \\ -\, y_{i\to j}^* y_{j\to i} & \text{for } j \neq i. \end{cases} \tag{3.16}$$

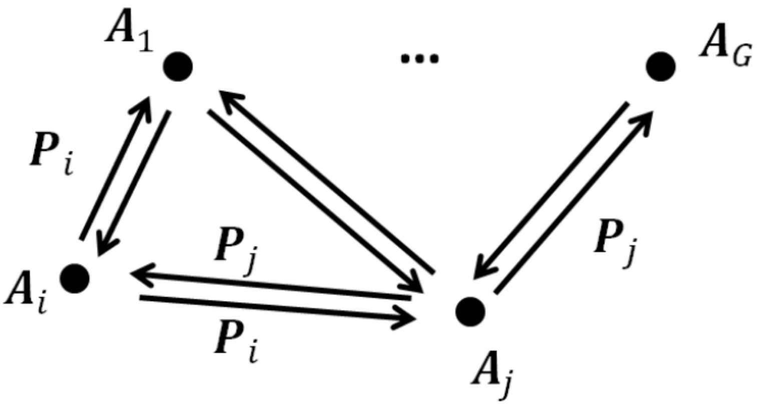

Figure 3.4 – Successive bi-directional transmissions followed by centralized LS estimation.

(3.14) can also be solved by assuming a unit norm on $\mathbf{u}$, the solution is then given by $V_{min}(\mathbf{A})$, the eigenvector corresponding to the eigenvalue with the smallest magnitude [28].

3.3.3 The Avalanche calibration method

Avalanche [31] belongs to a class of novel fast RF calibration techniques in order to enable low-overhead calibration of massive arrays for reciprocity based MIMO. This fast recursive calibration method exploits multi-stage sequential calibration, whereby at each stage the already calibrated part of the array is exploited to jointly calibrate multiple antennas with a single common pilot transmission. Thus, Avalanche belongs to the class of calibration methods that can calibrate massive arrays with moderate overheads.

The Avalanche calibration scheme may be represented within the group-based calibration framework by considering $M = \frac{1}{2}G(G-1)+1$ RRUs where G is the number of groups of RRUs partitioning the set of RRUs as follows: group A_1 contains RRU 1, group A_2 contains RRU 2, group A_3 contains RRUs 3 and 4, etc. until group A_G that contains the last $G-1$ RRUs. In other terms, group A_i contains $M_i = \max(1, i-1)$ antennas. Moreover, each group A_i uses $L_i = 1$ channel use by sending the pilot $\mathbf{P}_i = \mathbf{1}_{M_i \times 1}$. An example with 7 RRUs partitioned into 4 RRU groups, where we use calibrated groups 1, 2, 3 to calibrate group 4, is shown in Fig. 3.5.

In this case, (3.5) then becomes

$$(\mathbf{y}_{j\to i}^T * \mathbf{P}_i^T)\mathbf{f}_i - (\mathbf{P}_j^T * \mathbf{y}_{i\to j}^T)\mathbf{f}_j = \tilde{\mathbf{n}}_{ij}. \tag{3.17}$$

In [31], the authors exploited an online version of the LS estimator using previously estimated calibration parameters $\hat{\mathbf{f}}_1, \ldots, \hat{\mathbf{f}}_{i-1}$ by minimizing

$$\begin{aligned}\hat{\mathbf{f}}_i &= \arg\min_{\mathbf{f}_i} \sum_{j=1}^{i-1} \left\| (\mathbf{y}_{j\to i}^T * \mathbf{P}_i^T)\mathbf{f}_i - (\mathbf{P}_j^T * \mathbf{y}_{i\to j}^T)\hat{\mathbf{f}}_j \right\|^2 \\ &= (\mathbf{Y}_i^H \mathbf{Y}_i)^{-1} \mathbf{Y}_i^H \mathbf{a}_i, \end{aligned} \tag{3.18}$$

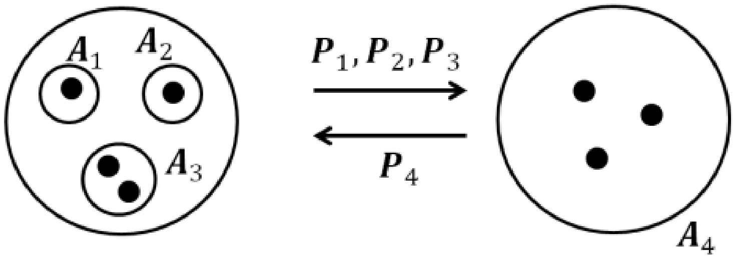

Figure 3.5 – Avalanche calibration with 7 RRUs partitioned into 4 groups. Already calibrated groups 1, 2 and 3 calibrate group 4.

where $\mathbf{Y}_i = \begin{bmatrix}\mathbf{y}_{1\to i} & \mathbf{y}_{2\to i} & \cdots & \mathbf{y}_{i-1\to i}\end{bmatrix}^T \in \mathbb{C}^{(i-1)\times M_i}$, and $\mathbf{a}_i = [(\mathbf{P}_1^T * \mathbf{y}_{i\to 1}^T)\hat{\mathbf{f}}_1, \ldots, (\mathbf{P}_{i-1}^T * \mathbf{y}_{i\to i-1}^T)\hat{\mathbf{f}}_{i-1}] \in \mathbb{C}^{(i-1)\times 1}$.

It is worth noticing that $\mathbf{f}_1, \ldots, \mathbf{f}_{i-1}$ are replaced by their estimated version which may cause error propagation. Estimation errors on a given calibration coefficient will later propagate to subsequently calibrated RRUs as we will see in Section 5.3.

3.4 Summary

In this chapter, we described the general system model for reciprocity calibration and a proposed fast calibration method based on antenna grouping. Moreover, we reviewed some basic existing calibration techniques which are later implemented in our C-RAN testbed for comparison reasons.

Chapter 4

Synchronization and Calibration on the OAI C-RAN testbed

4.1 System Architecture

Eurecom deployed a cloud radio access network (C-RAN) network using OpenAirInterface (OAI) software and inexpensive commodity hardware, Fig. 4.1 [38]. The testbed consists of the following 3 main entities:

1. The remote radio unit (RRU) which is a radio transceiver and contains the RF processing circuitry.
2. The radio aggregation unit (RAU) which connects multiple RRUs to a baseband unit (BBU) and serves as a data processing unit.
3. The radio cloud center (RCC) which is responsible for the centralized baseband processing and controls multiple RAUs.

The RCC runs on 20 Core Dell T620 server which is connected to Gigabit Optical Switch (Cisco Catalyst 2960-X). A set of 20 RRUs is deployed on the ceilings of the corridors on levels -3 and -4 of the Eurecom building Fig. 4.2. The RRUs on each floor are connected by Gbit Ethernet to a switch which are in turn connected to a central server over optical 20 Gbit Ethernet. A frequency reference unit outputs ten high-precision 40 MHz frequency reference outputs on each floor. The RRUs consist of an UP board from Intel, a B200 mini from Ettus Research, a RF frontend designed by Eurecom and Power over Ethernet (PoE) technology, Fig. 4.3. The system bandwidth is 10 MHz at the frequency of 2.58 GHz.

4.2 OpenAirInterface

OpenAirInterface (OAI), [87], wireless technology platform offers an open-source software-based implementation of the 3GPP stack:

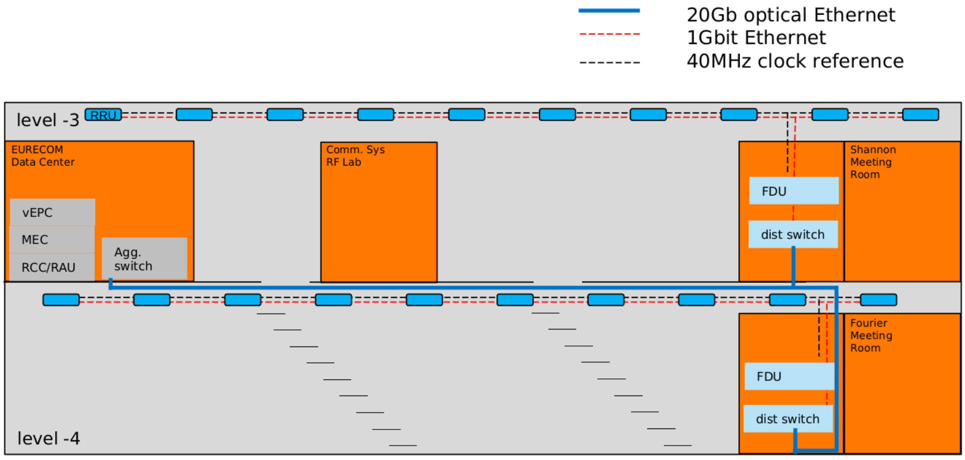

Figure 4.1 – OpenAirInterface 5G testbed

Figure 4.2 – RRU deployed on the ceiling of the corridor.

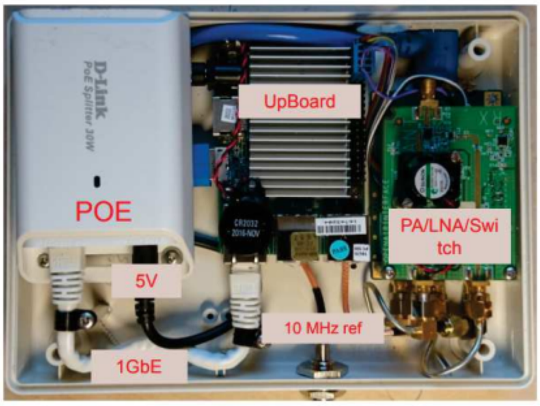

Figure 4.3 – RRU built from commodity hardware

- The radio access network (eNB, gNB and 4G, 5G UE).
- The core network (EPC and 5G-CN).

The OAI source code is split into two projects:

1. OAI Radio Access Network (OAI-RAN).
2. OAI Core Network (OAI-CN). Including Mobility Management Entity (MME), Home Subscriber Server (HSS), Serving Gateway (SGw) and Packet Data Network Gateway (PGw).

It can be used to build and customize a base station (OAI eNB/gNB), a user equipment (OAI UE) and a core network (OAI EPC) on a PC. The OAI eNB can be connected either to a commercial UEs or OAI UEs to test different configurations and network setups and monitor the network and mobile device in real-time. OAI is based on a PC hosted software radio frontend architecture. With OAI, the transceiver functionality is realized via a software radio front end connected to a host computer for processing. OAI is written in standard C for standard Linux-based computing equipment (Intel x86 PC/ARM architectures) and released as free software under the OAI License Model. OAI provides a rich development environment with a range of built-in tools such as highly realistic emulation modes, soft monitoring and debugging tools, protocol analyzer, performance profiler, and configurable logging system for all layers and channels. The schematic of the implemented LTE protocol stack in OAI is shown in Figure 4.4.

4.3 Multi-thread Parallelization and Precoding on OAI C-RAN testbed

4.3.1 Transmission modes and Antenna Ports in 3GPP standards

The various MIMO concepts apply to LTE transmission modes (TMs) which are explained in Table 4.1. Some TMs are designed mainly to increase throughput, some are to increase

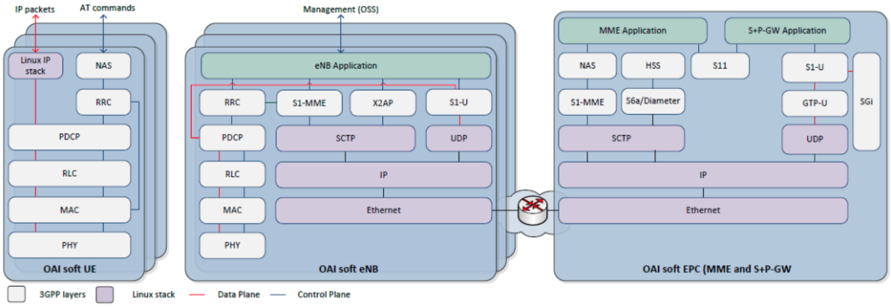

Figure 4.4 – OpenAirInterface LTE software stack

Transmission modes	Description	DCI	Comment
1	Single transmit antenna	1/1A	single antenna port port 0
2	Transmit diversity	1/1A	2 or 4 antennas ports 0,1 (...3)
3	Open loop spatial multiplexing with cyclic delay diversity (CDD)	2A	2 or 4 antennas ports 0,1 (...3)
4	Closed loop spatial multiplexing	2	2 or 4 antennas ports 0,1 (...3)
5	Multi-user MIMO	1D	2 or 4 antennas ports 0,1 (...3)
6	Closed loop spatial multiplexing using a single transmission layer	1B	1 layer (rank 1), 2 or 4 antennas ports 0,1 (...3)
7	Beamforming	1	single antenna port, port 5 (virtual antenna port, actual antenna configuration depends on implementation)
8	Dual-layer beamforming	2B	dual-layer transmission, antenna ports 7 and 8
9	8 layer transmission	2C	Up to 8 layers, antenna ports 7-14
10	8 layer transmission	2D	Up to 8 layers, antenna ports 7-14

Table 4.1 – Downlink transmission modes.

communications reliability and others are to handle multiple users simultaneously.

Antenna ports are specified by the LTE standard as logical entities differentiated by their reference signal sequences, Table 4.2. Reference signals are predefined signals within the downlink time-frequency grid occupying particular resource elements. The LTE specification contains many types of reference signals which are transmitted in various ways and are intended to be used by an UE for different purposes. MBSFN-RSs are transmitted in the MBSFN region of subframes only when the physical multicast channel (PMCH) is transmitted. PRS determines the location of an UE based on radio access network information. CSI-RSs are downlink reference signals intended to be used by UEs to acquire downlink CSI.

In our study we are mainly concerned with CRSs and UE-specific RSs. The downlink CRSs are used for cell search and initial acquisition, channel quality measurements and coherent demodulation. CRSs are common to all users. On the other hand, UE-specific RSs are specific to a user allocation, they are precoded reference signals using the same

Antenna Ports	**Downlink Reference Signals (RSs)**
port 0-3	Cell-specific RS (CRS)
port 4	Multicast Broadcast Single Frequency Network RS (MBSFN-RS)
port 5	UE-specific RS for single-layer beamforming (TM7)
port 6	Positioning RS (PRS)
port 7-8	UE-specific RS for dual-layer beamforming (TM8)
port 9-14	UE-specific RS for multi-layer beamforming (TM9)
port 15-22	Channel State Information RS (CSI-RS)

Table 4.2 – LTE antenna ports and their physical mapping.

beamforming weights as the data for each user.

4.3.2 Precoding and Beamforming for MIMO Downlink Channels in 3GPP standards

For the sake of completeness, we define what we understand as *precoding* and *beamforming* in the wireless communications. What is the difference between beamforming and precoding? When shall we use each technique? We name precoding the process of applying appropriate weighting (phase and gain) in the level of *antenna ports*. While using the technique of beamforming in the level of *physical antennas*. Antenna mapping can be designed according to various multi-antenna transmission schemes in different ways, including transmission diversity, beamforming, and spatial multiplexing [88]. In a multi-user MIMO system, a multi-antenna transmitter communicates simultaneously with multiple receivers. If we need to transmit data streams to two different users, and use the technique of beamforming, the same set of physical antennas may correspond to two separate antenna ports. Thus, we will apply first precoding weights to the antenna ports and then beamforming weights to the physical antennas. In general, we consider that precoding is a generalization of beamforming in order to support multi-layer transmission in multi-antenna wireless communications.

Beamforming utilizes multiple antennas in an array to control the direction of a wavefront by properly weighing the magnitude and phase of individual antenna signals [89]. The relative amplitude and phase shifts cause the output signals from the antenna array to match together coherently for a specific transmit/receive angle and cancel each other out destructively for other signals [64]. As a result, we get a lobe of power steering in a particular direction towards a user, as shown in Figure 4.5. Since every single antenna in the array makes a contribution to the steered signal, an array gain (aka, beamforming gain) is achieved.

In digital beamforming (aka, baseband beamforming, precoding) the signal is precoded (phase and amplitude modifications) in baseband processing before RF transmission. Digital beamforming (MU-MIMO) is used in LTE Advanced Pro (TMs 7,8, and 9) and in 5G NR. It improves the cell capacity as the same PRBs are used to transmit data simultaneously for multiple users.

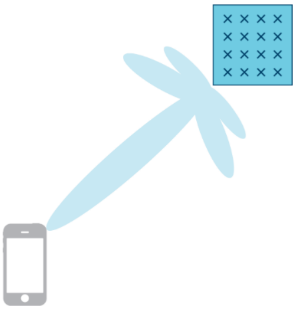

Figure 4.5 – Creating directional beams by varying the phase and amplitude of each antenna.

4.3.3 Integrating the precoding functionality into OAI

Based on the platform described in 4.1 we implemented transmission mode 8 (TM8) on OAI to support dual-layer beamforming, a precoder to map the logical antennas to the physical antennas carried by each RRU. For distributed MIMO systems, the calibration coefficients are obtained by exchanging calibration signals between the different RRUs.

Figure 4.7 depicts the integration of the precoder function into OAI. The IF4p5 fronthaul interface is the functional split implemented in the OAI platform, also known as the equivalent split option 7-2x in the 3GPP terminology [90]. In the split option 7-2x, in the UL, FFT, CP removal and resource de-mapping functions reside in the DU, the rest of PHY functions reside in the CU. In the DL, IFFT, CP addition, resource mapping and precoding functions reside in the DU, the rest of PHY functions reside in the CU. Accordingly, the IF4p5 functional split option in OAI, corresponds to the split-point at the input and output of the Orthogonal Frequency Division Multiplexing (OFDM) symbol generator Figure 4.6. The L1 instance is a separate set of threads for the eNB procedures and the RU entity manages a set of physical antennas, performing precoding of multiple eNB transmit streams and OFDM modulation and demodulation.

The precoder entity represents essentially the *antenna mapping* which is the combination of *layer mapping* and *precoding* the transmit data with different beamforming weights for each physical antenna/RRU. In layer mapping, the modulation symbols for one or two codewords will be mapped onto one or several layers. In our implementation, physical downlink control channel (PDCCH) and physical broadcast channel (PBCH) information on antenna ports 0 and 1 are mapped to the RRUs using common beamforming weights. While physical downlink shared channel (PDSCH) data on antenna ports 7 and 8 are mapped to the RRUs with UE-specific beamforming weights. An example of antenna mapping in the case of dual-layer beamforming with MU-MIMO is shown in Figure 4.8.

The reference signals (RSs) are LTE downlink physical signals which enable channel estimation. Specific pre-defined resource elements (REs) in the time-frequency domain carry the cell-specific and ue-specific reference signal sequence. Cell-specific RSs are available for all UEs in a cell. Their role is to enable the UE to determine the phase reference for demodulating the downlink control channels and downlink data. UE-specific

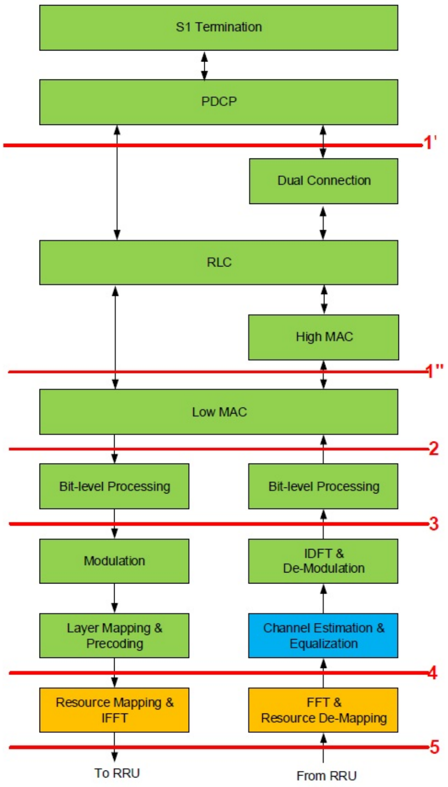

Figure 4.6 – Functional split IF4.5 in OAI

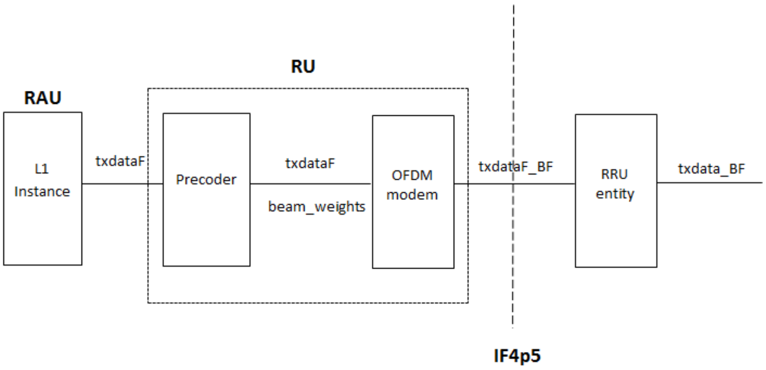

Figure 4.7 – Precoder configuration

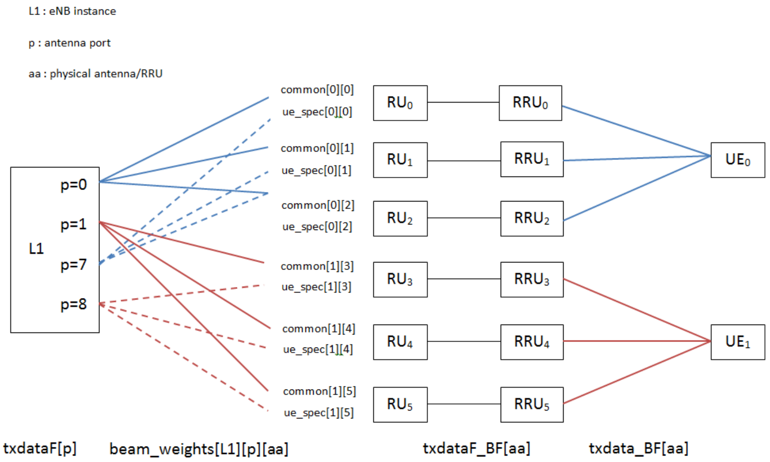

Figure 4.8 – Dual-layer beamforming with MU-MIMO

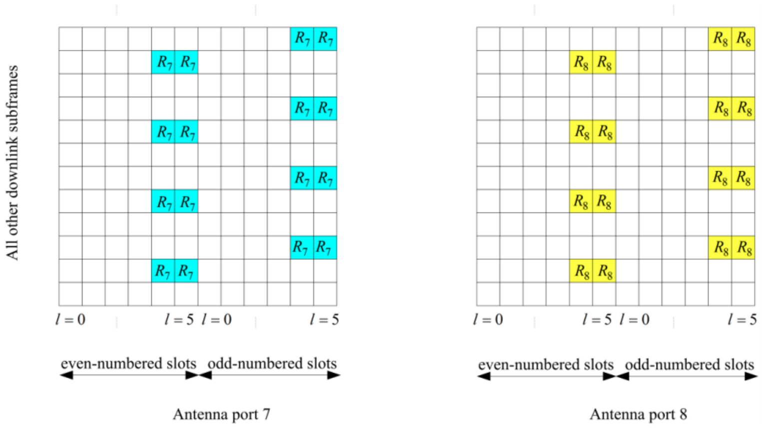

Figure 4.9 – Distribution of RSs for TM8

RSs are used for beamforming, where the PDSCH for each UE is sent with a different beamforming weighting. The UE-specific RSs and the data on the PDSCH for a UE are transmitted with the same beamforming weights. In TM8, the same REs are used, hence, the UE-specific RSs must be coded differently so that the UE can distinguish among them, Figure 4.9.

In order to implement dual-layer beamforming for multiple users on OAI we integrated the UE-specific RSs in the physical layer. UE-specific RSs are applied on antenna ports 7 and 8 to estimate the beamformed data channel in TM8/9. The UE-specific RSs associated with PDSCH are generated in the correct REs of one resource block (RB) compared to the corresponding Matlab LTE Toolbox.

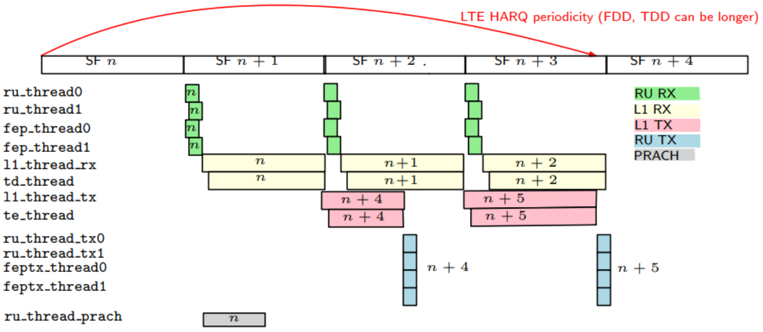

Figure 4.10 – Multi-thread parallelization for 2 RUs at RCC side (in theory)

4.3.4 Multi-thread Parallelization

The precoder and OFDM modulation for different RUs run in parallel for each subframe in order to reduce the processing time. In Figure 4.10 we see the theoretical parallelization of the main threads executed throughout the IF4p5-RU-eNB end. Each thread takes in charge the front end processing, precoding and OFDM modulation for one RU.

In order to confirm the right multi-thread parallelization and compare the precoding processing time while increasing the number of emulated RRUs, we run the OAI LTE softmodem on a 36-core machine. We compile the lte-softmodem with the -V option in order to support value change dump (VCD) debugging for timing analysis and signal visualization. In Figure 4.11 we can see 20 RUs being perfectly synchronized.

4.4 Synchronization of RRUs and Hardware Constraints

There are three levels of synchronization:

- *Time synchronization*,to ensure that the frames are aligned between the different RRUs up to within a sample.
- *Frequency synchronization*,to ensure that the RRUs stay synchronized in time and phase.
- *Phase synchronization*, to enable coherent transmission and precoding.

Our system is based on LTE TDD configuration 1, which has two UL, two DL, and one special subframe every 5ms, Fig. 4.12.

4.4.1 Time synchronization

Timing synchronization may consist of frame/slot/symbol/chip synchronizations, residual timing tracking, first arrival path search (in terms of Orthogonal Frequency-Division Multiple Access (OFDMA)) or multi-path search (in terms of Code-Division Multiple Access (CDMA)).

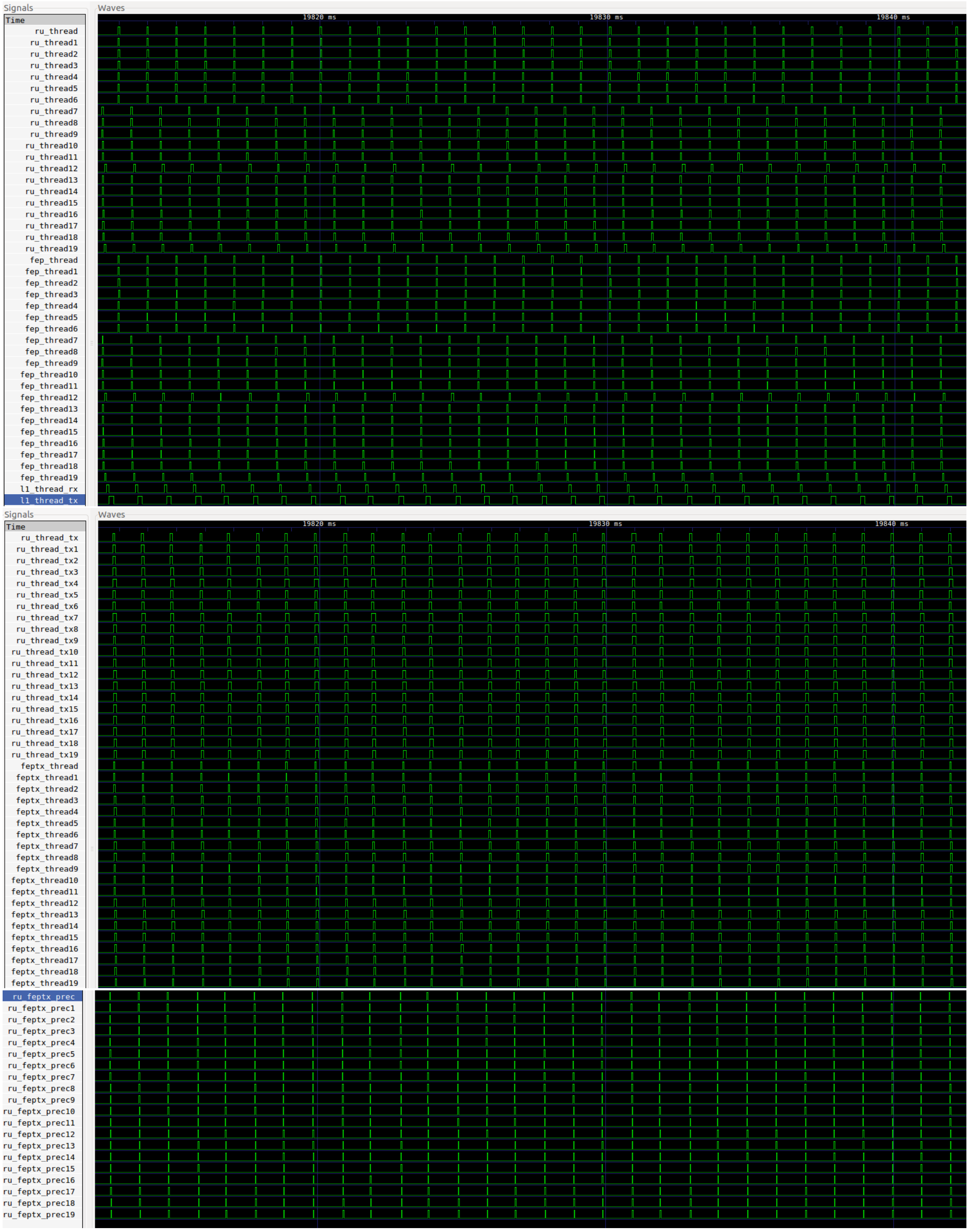

Figure 4.11 – Multi-thread parallelization for 20 RUs

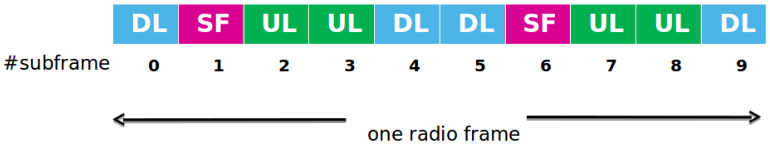

Figure 4.12 – LTE TDD configuration 1

Time across all RRUs must be synchronized to within the accuracy of 1 sample of the A/D and D/A converters. As mentioned before, the timing relation can be obtained through various means, including satellite systems for global navigation, coaxial cables, packet-based networks or over-the-air synchronization. The fronthaul interface in our C-RAN testbed consists of asynchronous Ethernet communication links which do not provide time and frequency synchronization since they do not support time-sensitive networking features such as IEEE 1588 precision time protocol and SyncE. In other words, our solution, avoids GPS or network-based synchronization and focuses on an OTA mechanism as it is a low-cost approach easy to implement with signal processing and no additional hardware. Time synchronization is achieved by using over-the-air trigger-based synchronization using a “master-slave” protocol, where one RRU acts as the master and the rest of the RRUs synchronize to it much as an UE would synchronize to the network. We leverage the “master-slave” architecture because our OAI platform features one RCC attached to a single RRU (master) through control/configuration signaling. Thus, the other RRUs (slaves) first synchronize in time with the master RRU and then attach to the RCC.

However, the primary synchronization sequence (PSS) used for UE synchronization would not provide the required accuracy as it only occupies ∼1MHz. Therefore we have added a demodulation reference symbol (DMRS) in OFMD symbol 3 of the special subframe 1, just after the PSS. The timing synchronization should be performed without interrupting data streaming, for that reason we select the special subframe in a TDD frame since it is only required for switching the transmission between UL and DL. OTA timing synchronization includes timing offset adjustment through edge detection of the received signal in order to compensate for the possible difference in samples as shown in Fig. 4.13.

As soon as the initial sync is done the frames are aligned and the slave RRUs start to connect to RAU. When the RAU knows that slave is running it sends a resynchronization command to the slave RRU to change its frame number to the right one.

4.4.2 Frequency Synchronization

In order to have all the RRUs form a single DAS, we have to provide a reference for frequency and time synchronization. A shared 10MHz oven-controlled crystal oscillator (OCXO) reference provides frequency disciplining for the internal voltage-controlled oscillator (VCO) used to generate the system local oscillator (LO) and A/D and D/A channels, both of which must be synchronized across the entire RRU array.

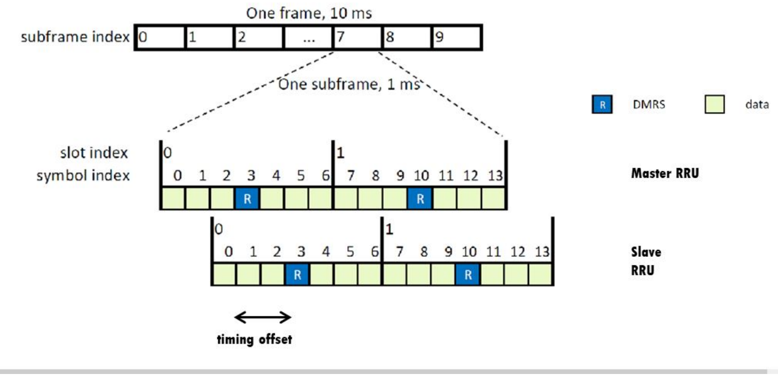

Figure 4.13 – Timing offset adjustment

Sharing the common 10MHz reference among RRUs allows a phase-coherent LO to be synchronized using a fractional-N frequency approach. During synthesis, as the reference is divided, the phase may lock on either rising or falling edges producing a constant but arbitrary phase offset on each channel. Due to a poor PLL design on the B200 USRPs we realized that the phase does not lock, showing a large deviation over 2π, rendering our system beamforming-uncapable. To deal with this phase incoherence we disabled the VCTCXO at each RRU and we replaced it with a 40MHz signal which is directly fed into the RF chip of the B200. A more detailed analysis of the frequency synchronization issues will be given on Subsection 4.4.4.

4.4.3 Phase synchronization/Calibration

Beamforming places additional requirements on the system. In addition to sample time and sample clock alignment, the system must maintain a known phase relationship between each RF chain. However, because each radio has an independent synthesizer circuit (PLL-VCO) for both Tx and Rx, the phase can be considered phase coherent but not phase aligned. Through periodic calibration, alignment can be achieved by digitally adjusting the real and imaginary signal component (I,Q) phase.

In order to calibrate the C-RAN testbed we need to collect channel measurements between the master and the slave RRUs. This is achieved by using the framework shown in Fig. 4.14. In this example there are 3 RRUs, 1 master RRU M and 2 slave RRUs S0,S1. In the first special subframe (SSF) in a TDD configuration 1 frame symbol 3 and 10 are reserved DMRS symbols.

The slave RRUs sacrifice symbol 2 in order to switch from Tx to Rx mode, so that PSS is omitted and only the first two PDCCH symbols are transmitted in the DL. At each special subframe 1 every 10ms, only one RRU transmits the calibration symbol. If the RRU which is in transmit mode is a master RRU then all the active slave RRUs receive, decode and estimate the DL channel estimates at symbol 10. On the other side, if a slave RRU transmits the calibration symbol, only the master RRU collects and estimates the UL channel estimates. Thus, a bidirectional calibration symbol exchange for a pair of

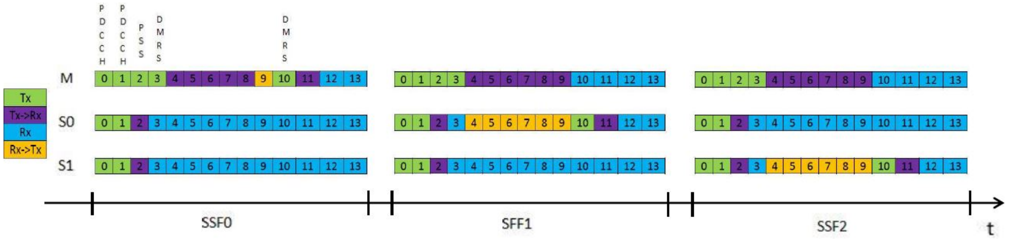

Figure 4.14 – Synchronization-Calibration framework

RRUs takes up to 20ms. We assign a number at each RRU, *tag*, such that each RRU enables its transmit mode if and only if $\textit{frame} \bmod p = \textit{tag}$, where $\textit{frame} = \{0, 1, .., 1023\}$ is the frame number and p is the number of active RRUs in the testbed. In contrast to the frequency with which the master RRU transmits the calibration symbol, the synchronization symbol is broadcasted to the slave RRUs every 10ms.

4.4.4 Hardware Issues

In order to build a distributed massive MIMO testbed with a certain number of RRUs, coherent transmission and reception among them is necessary. For this reason, all RRUs share the same RF reference signal. The USRP B200mini does not have a dedicated PLL chip to generate the 40 MHz reference signal for the RF chip from the external 10 MHz reference signal. Hence, signals from two such USRPs even though connected to the same external reference will not be locked in phase. Therefore, the USRP was modified by removing the local 40MHz oscillator and replacing it by a new reference input line. This modification allows the usage of an external reference signal to ensure phase stability among RRUs. In order to keep a reference frequency of 10MHz instead of 40MHz for convenience, a multiplier board (quadrupler) was added to the RRU. The multiplier board is a simple device with a quadrupler IC that just multiplies an input frequency by a factor of four. In a first field trial, we observed that the RRUs output signal suffers from severe out of band emissions. At this point, it was not obvious what the source of this impairment was. Through a tedious process of debugging, involving several measurements and experiments in the laboratory, we concluded that the phase noise performance of the multiplier board is not sufficient for the USRP reference signal. The impure RF output signal of the USRP were caused by the high phase noise of the 40MHz reference signal provided by the multiplier board. A measured sinusoidal signal of 1MHz at 2.58GHz from the USRP with a reference signal provided from the multiplier board is shown in Fig. 4.15. We therefore decided to remove the multiplier board from the RRU design and provide a 40MHz reference signal to all RRUs. This was achieved by a high-quality signal generator and a splitter, to support multiple RRUs at the same time. Through this modification, clean transmit signals with coherent phase of the RRUs were obtained. The USRP's output signal of a the same 1MHz signal at 2.58GHz as before, but with a high quality 40MHz reference source is shown in Fig. 4.16. We observe that the output signal's SINR has dramatically improved. During investigation of the phase instability among multiple RRU entities, a measurement with two USRPs connected

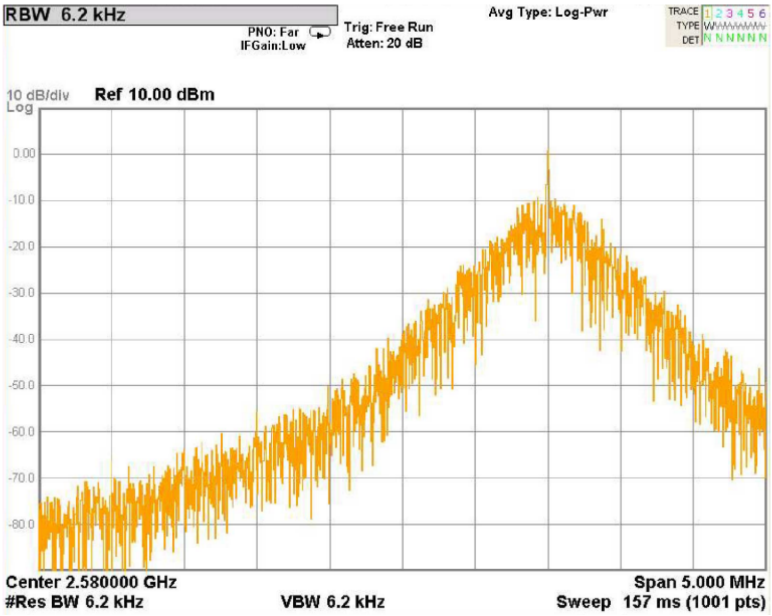

Figure 4.15 – Measured sinusoidal signal with the multiplier

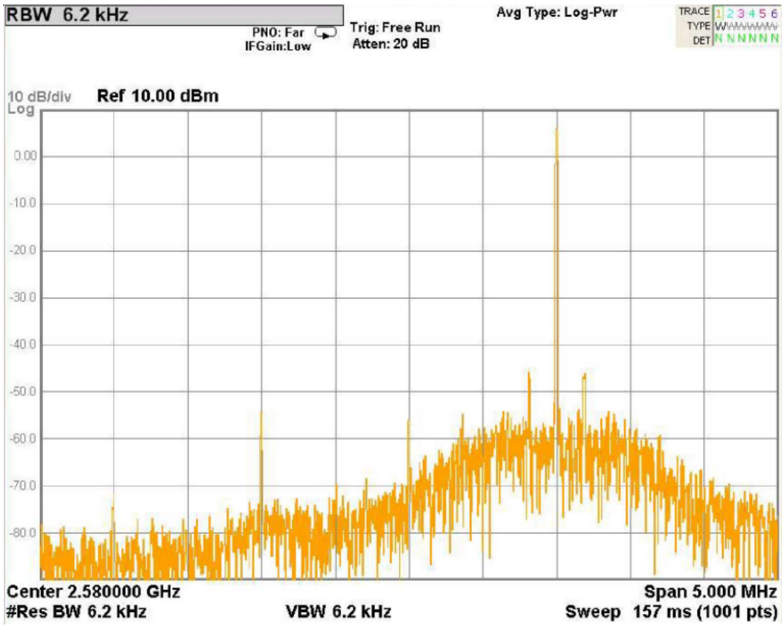

Figure 4.16 – Measured sinusoidal signal without the multiplier

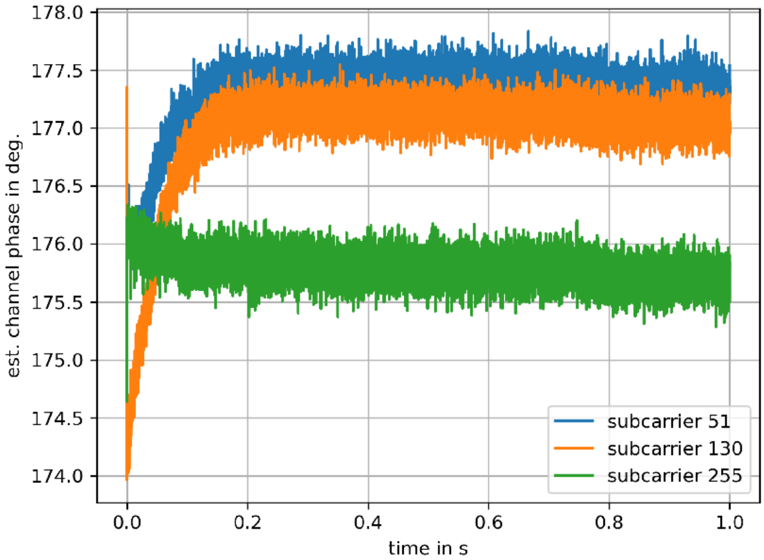

Figure 4.17 – Estimated phase

back to back was performed in the lab. Both USRPs are fed by a low phase noise 40MHz reference. An OFDM signal with Nyman phases and 300 subcarriers spaced by 15kHz was transmitted by one USRP and received with the other one. The OFDM symbol was continuously repeated for a duration of 1sec. In order to investigate the phase stability of the setup, the phase of the received signal was estimated. A plot of the estimated phase over 1sec for three randomly chosen subcarrier indices is depicted in Fig. 4.17. This experiment proves that the phase between two RRUs is stable over an extended time duration and only residual phase noise is observed.

In Fig. 4.18 we see a detailed presentation of our modified RRUs. For better understanding, a block diagram of the modified RRU is drawn in Fig. 4.19. The RRU has two connections. A 1G ethernet connection over a CAT7 cable and a 40 MHz RF reference signal over a RG213U coaxial cable. Both of these connections lead from the ceiling mounting spot of the RRU directly to the switch room at the end of the corridor and might therefore be up to approximately 50m. In order to prevent ground loops over these two connections, a transformer providing galvanic isolation is inserted in the 40 MHz reference line. It is a 1:1 (transformation factor) transformer Coilcraft PWB1010-1 with a 3dB bandwidth of 30 kHz-250 MHz, designed for 50Ohm systems.

4.5 Summary

In this chapter, we described the architecture of our C-RAN testbed which is based on the open-source OAI software and cheap commodity hardware. We discussed about the LTE basics on precoding and how we integrated these technologies into OAI. Furthermore, we analyzed the challenges for RRU synchronization and proposed low-cost solutions for

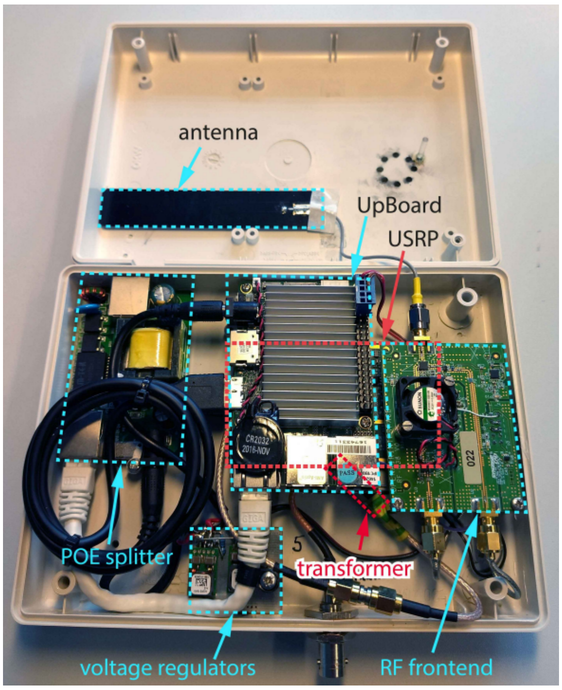

Figure 4.18 – Modified RRU structure

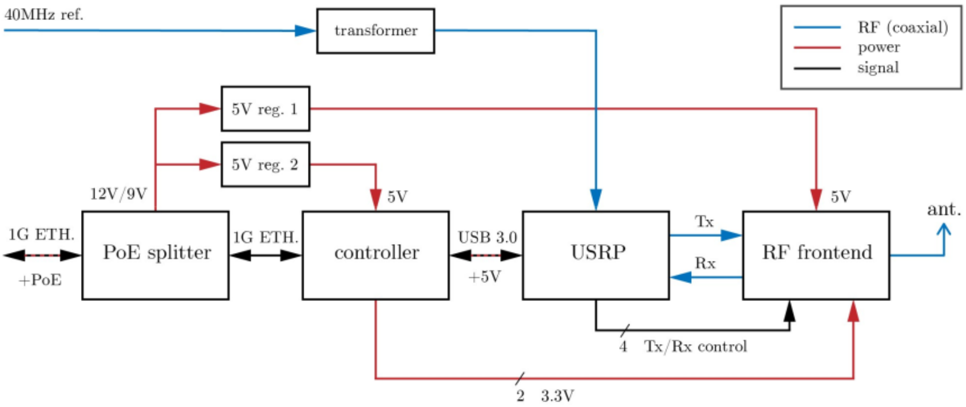

Figure 4.19 – RRU block diagram

hardware-related issues.

Chapter 5

Real-time Performance Evaluation of Relative Calibration Schemes on the OAI C-RAN testbed

In this chapter, we present a group-based OTA calibration framework and through real-time measurements on our C-RAN testbed and OAI software we compare its performance against existing calibration algorithms from Section 3.3. We show the performance gains when we minimize the size of the largest group and simultaneously forming groups by selecting RRUs in an interleaving way. The results of this work are presented in [91].

5.1 Estimation of the Calibration Matrix for a group-based scheme

In this work we played around with different ways of creating groups in a set of active RRUs. Our scope was to find out the optimal grouping and simultaneously access its performance against some existing calibration algorithms in the literature. For example, if we had a set of 5 RRUs active in out C-RAN testbed, would it be preferable to split them in groups of 3 and 2 RRUs or in groups of 2, 2 and 1? Questions like this will be answered later in this section.

Let's analyze how we estimate the reciprocity calibration elements $\hat{f}$ of the calibration matrix $\mathbf{F}$ derived from a grouping scheme of 5 RRUs. We consider $M = 5$ RRUs partitioned into $G = 2$ groups denoted by A_1 and A_2 as in Fig. 5.1. Group A_1 contains $M_1 = 3$ RRUs and group A_2 has $M_2 = 2$ RRUs. Group A_1 transmits a sequence of $L_1 = 3$ calibration symbols, defined by matrix $\mathbf{P}_1 \in \mathbb{C}^{M_1 \times L_1}$, and group A_2 transmits $L_2 = 2$ calibration symbols, defined by matrix $\mathbf{P}_2 \in \mathbb{C}^{M_2 \times L_2}$. The calibration symbols are generated by the same set of base sequences used for PUSCH DMRS [92]. The modulation type used is Zadoff-Chu, causing the constellation for pilots to look like irregularly spaced points on a circle with unit power. The Zadoff-Chu sequence values

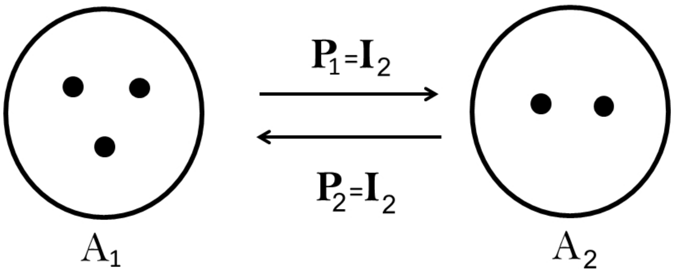

Figure 5.1 – Bi-directional transmission between two RRU groups.

are modulated directly onto the subcarriers using OFDM. The received signal for each resource block of bidirectional transmission between the two RRU groups is given by,

$$\begin{aligned} \mathbf{Y}_{1\to 2} &= \mathbf{R}_2\mathbf{C}_{1\to 2}\mathbf{T}_1\mathbf{P}_1 + \mathbf{N}_{1\to 2} \\ \mathbf{Y}_{2\to 1} &= \mathbf{R}_1\mathbf{C}_{2\to 1}\mathbf{T}_2\mathbf{P}_2 + \mathbf{N}_{2\to 1} \end{aligned} \tag{5.1}$$

where $\mathbf{Y}_{1\to 2} \in \mathbb{C}^{M_2 \times L_1}$ and $\mathbf{Y}_{2\to 1} \in \mathbb{C}^{M_1 \times L_2}$ are received signal matrices at RRU groups A_2 and A_1 respectively. $\mathbf{N}_{1\to 2}$ and $\mathbf{N}_{2\to 1}$ represent the corresponding received noise matrix. $\mathbf{T}_1,\ \mathbf{R}_1 \in \mathbb{C}^{M_1 \times M_1}$ and $\mathbf{T}_2,\ \mathbf{R}_2 \in \mathbb{C}^{M_2 \times M_2}$ represent the effect of the transmit and receive RF front-ends of the RRUs in groups A_1 and A_2 respectively.

Following the same process as in Section 3.2 we derive the vectorized equation,

$$(\mathbf{Y}_{2\to 1}^T * \mathbf{P}_1^T)\mathbf{f}_1 - (\mathbf{P}_2^T * \mathbf{Y}_{1\to 2}^T)\mathbf{f}_2 = \tilde{\mathbf{n}}_{12} \tag{5.2}$$

This allows us to construct the $\boldsymbol{\mathcal{Y}}(\mathbf{P})$ defined as,

$$\underbrace{\Big[(\mathbf{Y}_{2\to 1}^T * \mathbf{P}_1^T) \quad -(\mathbf{P}_2^T * \mathbf{Y}_{1\to 2}^T)\Big]}_{(\sum_{j=2}^{G}\sum_{i=1}^{j-1} L_i L_j)\times M} \tag{5.3}$$

The estimation of the calibration coefficients consists in solving a LS problem assuming a unit norm constraint such as

$$\hat{\mathbf{f}} = \arg\min_{\mathbf{f}:\|\mathbf{f}\|=1} \|\boldsymbol{\mathcal{Y}}(\mathbf{P})\,\mathbf{f}\|^2 \;=\; V_{min}(\boldsymbol{\mathcal{Y}}(\mathbf{P})^H\boldsymbol{\mathcal{Y}}(\mathbf{P})) \tag{5.4}$$

where $V_{min}(\mathbf{X})$ denotes the eigenvector of matrix $\mathbf{X}$ corresponding to its eigenvalue with the smallest magnitude.

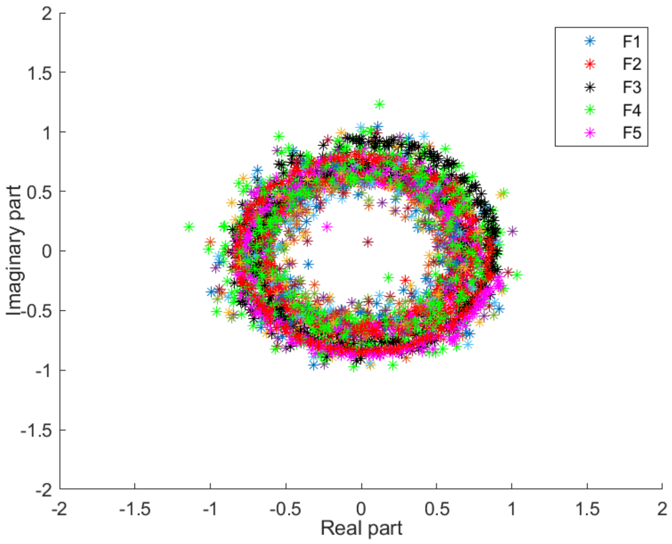

Figure 5.2 – Calibration coefficients in frequency domain using group-based FC method.

5.2 Evaluation Metrics

Fig. 5.2 depicts the diagonal estimation of the calibration coefficients $\hat{f}_j[l,k]$, in which each circle is composed of $k = 1, \ldots, K$ subcarriers covering the whole bandwidth, for each RRU with tag j, averaged across $l = 1, \ldots, L$ measurements. Note that the first coefficients are fixed to 1 so that $f_1 = 1$.

$$\hat{\mathbf{g}}_j[l] = \text{IFFT}\{\hat{\mathbf{f}}_j[l]\} \tag{5.5}$$

By converting the frequency response to the time domain we can see in Fig. 5.3 that a channel over 2.6 GHz is flat and a single filter tap is sufficient to represent the channel. Since we do not have the ground truth for our measurements (true calibration parameters are unknown), we cannot leverage the mean square error, $\text{MSE} = \mathbb{E}\left[\|\hat{\mathbf{f}} - \mathbf{f}\|^2\right]$, as our performance evaluation metric. An important channel parameter is the time-scale of the variation of the channel, which we use as a metric for "goodness" of the estimate.

Therefore, we compute the variance of the time-domain calibration elements computed at the maximum value given by

$$\begin{aligned} k' &= \arg\max_k \hat{g}_j[l,k], \\ \sigma_j &= \underset{l}{var}(\hat{g}_j[l,k']). \end{aligned} \tag{5.6}$$

5.3 Experimental Results

In this section, results from the experimental measurements are presented to illustrate the efficient application of the proposed fast calibration (FC) scheme from Section 3.2 to

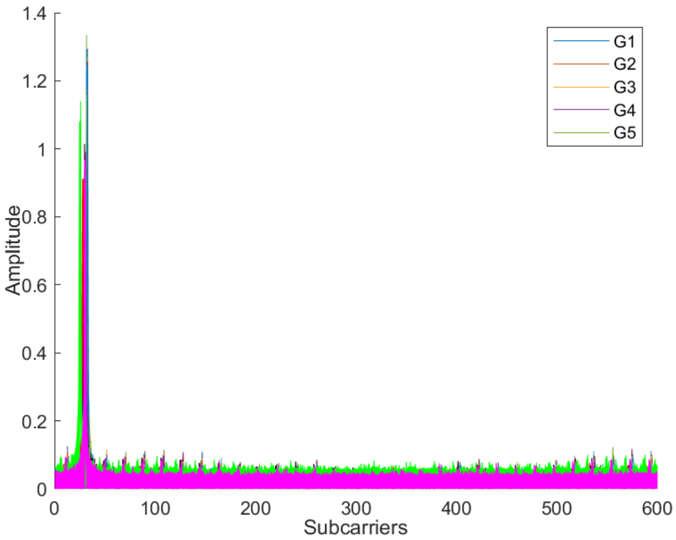

Figure 5.3 – Calibration coefficients in time domain.

our real-time C-RAN testbed. The DL/UL channel estimates extracted from the DMRS calibration symbols are sent via packetized I/Q samples to the RAU over fronthaul protocol on commodity Ethernet. The RAU receives inter-RRU reference signal measurements and deduces the needed calibration information to form a distributed MIMO transmitter. The system has always to be under calibrated status, therefore, calibration procedures need to be repetitively performed.

We first compare the proposed group-based FC method from Section 3.2 against the existing calibration methods Argos, Rogalin and Avalanche. FC-2-2-1 and FC-3-2 correspond to two different grouping schemes in the case of a set of $M = 5$ RRUs and FC-I corresponds to a fast calibration scheme where the RRU grouping is exactly the same as that of Avalanche (i.e., 1-1-2-1). For better understanding an illustration of these schemes is shown in Fig. 5.4. We assess numerically the performance of various calibration algorithms and compare them based on the estimated variance of the time-domain calibration coefficients.

In Fig. 5.5 the performance of the proposed FC-2-2-1 grouping greatly outperforms that of the Avalanche scheme. The LS estimator in Avalanche uses previously estimated calibration parameters which causes error propagation; estimation errors on a given calibration coefficient will propagate to subsequently calibrated RRUs. Moreover, it is important to note that the performance with the FC-2-2-1 grouping improves dramatically compared to the FC-3-2 scheme, since the overall estimation performance of the group-based FC is limited by the condition number of the largest group size. Hence, it is reasonable to try to minimize the size of the largest RRU group. Fig. 5.6 illustrates the performance results from three different grouping schemes (Interleaved, Neighbours, Random). "Interleaved" grouping corresponds to selecting every other RRU along to corridor while "Neighbours" scheme groups the closest RRUs together, Fig. 5.7. The

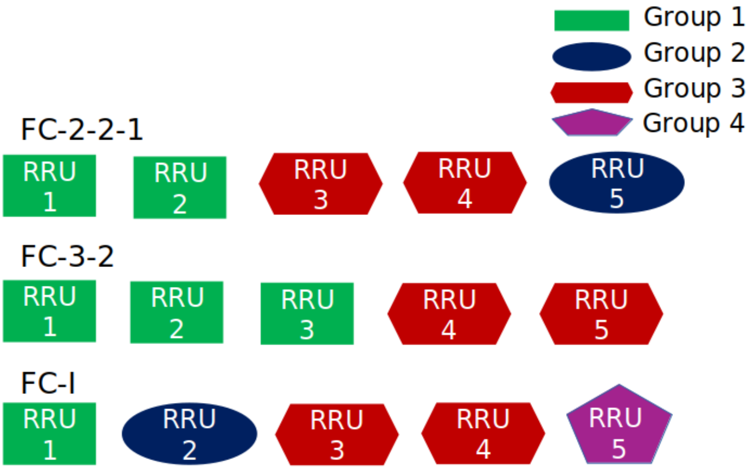

Figure 5.4 – Demonstration of different grouping methods for M=5 RRUs.

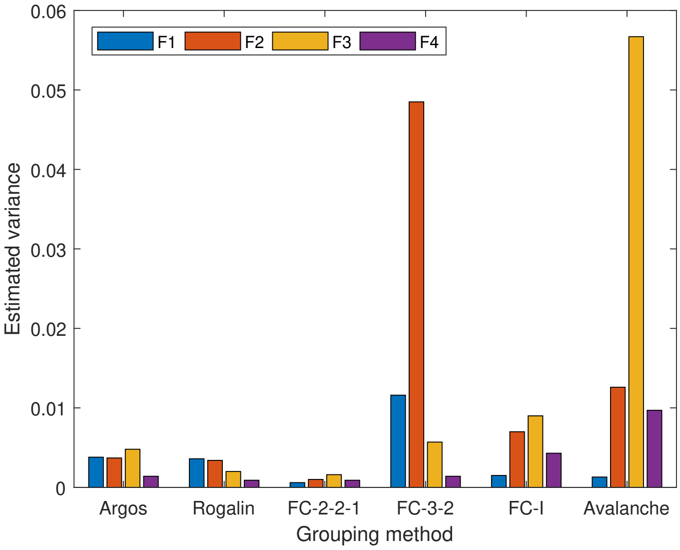

Figure 5.5 – Variance of the time-domain calibration coefficients (computed at the maximum value) for M=5 RRUs.

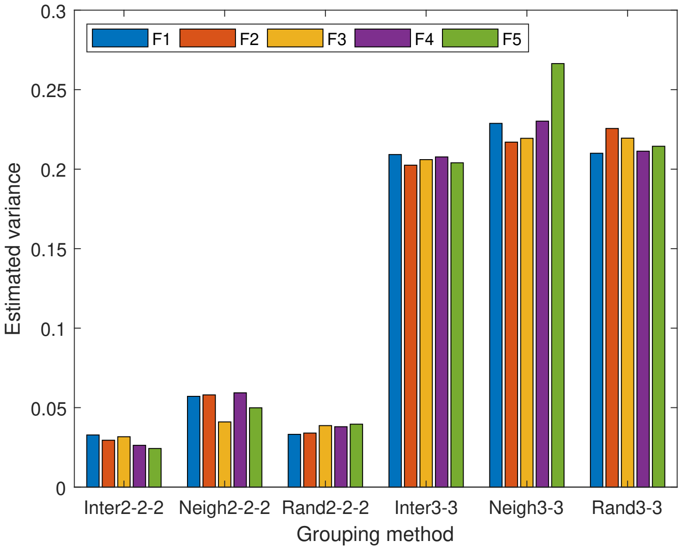

Figure 5.6 – Comparison of three different choices to form the RRU groups (FC with equally partitioned groups, M=6 RRUs).

performance gains at Inter2-2-2 and Inter3-3 show that the interleaving of the RRUs ensures that the channel from a group to the rest of the RRUs is as well conditioned as possible. Furthermore, we verify the fact that the performance improves when the group sizes are allocated more equitably to the minimum group size as in grouping scheme Inter2-2-2 which has a lower condition number (well-conditioned) than for scheme Inter3-3. A condition number applies to the LS problem being solved in (3.7). We invert the matrix, finding its eigenvalues. In Inter3-3 scheme, the matrix can be poorly conditioned for inversion so it is more sensitive to machine's relative round-off errors made during the LS solution process.

5.4 Summary

In this chapter, we proposed various ways of grouping distributed RRUs and an evaluation metric based on the variance of the time-domain calibration elements in order to compare their performance in real-time to existing calibration schemes in literature. We proved that a calibration scheme with equally partitioned groups of RRUs provides good performance gains. On top of that, we showed that by grouping the RRUs in an interleaving way we can get additional performance gains.

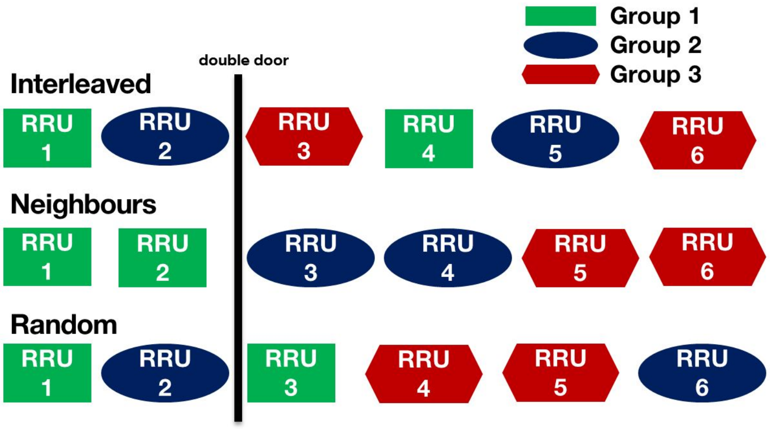

Figure 5.7 – Example of three different choices to form the RRU groups for M=6 RRUs.

Chapter 6

Modeling the OAI C-RAN testbed

In Chapter 5 we adapted a fast calibration (FC) scheme based on antenna grouping to our OAI C-RAN testbed in order to confirm its efficiency, in real environment. We examined the performance results from three different grouping schemes (Interleaved, Neighbours, Random) according to Fig. 5.7. We illustrated that the interleaved grouping of the RRUs results in performance gains. Furthermore, we played around with the size of the largest group and simultaneously formed groups by selecting RRUs in an interleaving way like in Fig. 6.1. This proved that the overall estimation performance of the group-based FC algorithm improves when we try to minimize the size of the largest RRU group. These conclusions we made based on the variance of the time-domain calibration elements. The scope of this chapter is to provide a ground truth for the evaluation of the group-based OTA calibration framework through channel measurements on our simulated distributed antenna system. We generate an indoor LOS radio wave propagation model using ray tracing technique and perform distributed channel reciprocity calibration which is required to exploit uplink (UL) channel estimates to infer the precoder performed on the downlink (DL) channel. We consider a channel based on the geometry of the area where the RRUs are distributed and compare the different choices to form the RRU groups. We validate that the simulation results match the experimental results from our work [91]. The results of this work are presented in [93].

6.1 Channel Model

In the case of indoor radio wave propagation along the corridor of a building, the free space path, ground and side wall reflective path are taken into consideration. The RRU positions are represented in the 3-dimensional space by means of three coordinates (i.e. inter-RRU distance, side wall distance, ceiling height). The inter-RRU distance is set to 5.5m, the distance of each RRU to the side wall is measured at 1.25m, while the ceiling height is 3m. We consider the 2-ray model with LOS and one dominant reflection from the ground Fig. 6.2. The path loss depends on whether we are in LOS or NLOS

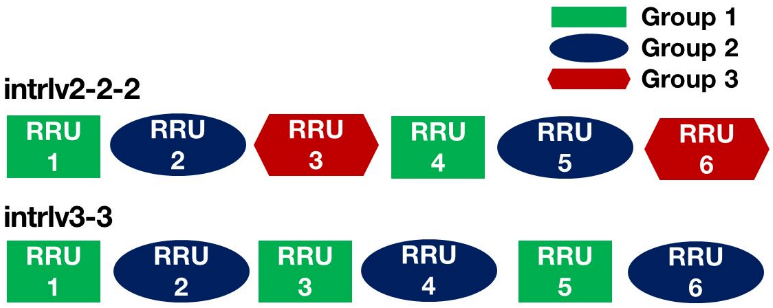

Figure 6.1 – Example of two different grouping sizes in an interleaving way for M=6 RRUs.

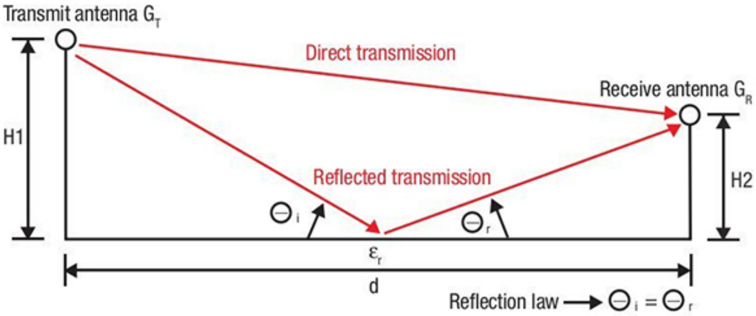

Figure 6.2 – 2-ray propagation model with a LOS ray and a ground-reflected ray.

conditions. In the NLOS case we take into account only the reflected ray and we assume a reflection coefficient of -1. Whereas, in LOS conditions we have to compute the phase difference between the direct ray and the reflected ray, since the received signal may suffer constructive or destructive interference.

The channel (amplitude and phase) between RRU m and n is

- NLOS case
$$\mathrm{c}'_{m,n} = -\frac{\lambda}{4\pi d_{\mathrm{refl}}} e^{-jkd_{\mathrm{refl}}} \tag{6.1}$$
- LOS case
$$\mathrm{c}'_{m,n} = \frac{\lambda}{4\pi d_{\mathrm{dir}}} \left(1 - e^{-jk(d_{\mathrm{refl}} - d_{\mathrm{dir}})}\right) \tag{6.2}$$

where λ is the wave length and $k = \frac{2\pi}{\lambda}$ is the wave number. In addition to the direct and reflected ray, we also account for diffuse components by adding a random phase $g_{m,n}$ drawn from a Rayleigh distribution $\mathcal{CN}(0,1)$ and scaled by a Ricean K-factor K.

$$c_{m,n} = \sqrt{K}\mathrm{c}'_{m,n} + \sqrt{1-K} g_{m,n}. \tag{6.3}$$

In our simulations we assume a Rician K-factor for indoor channels of 4dB.

6.2 Hardware properties model

The reciprocal values $\boldsymbol{T}_A$ and $\boldsymbol{R}_A$ are modeled as i.i.d. random variables, with independent magnitude uniformly distributed on $[1-\epsilon, 1+\epsilon]$, with ϵ chosen such that the standard deviation of the squared-magnitudes is 0.1, and uniformly distributed phase between $[-\pi \ \ \pi]$, [86]. We fix the first reciprocal coefficients to 1 ($f_1 = 1$). The transmitted pilots are generated by the same set of base sequences used for PUSCH DMRS. The modulation type used is Zadoff-Chu, causing the constellation for pilots to look like irregularly spaced points on a circle with unit power. The Zadoff-Chu sequence values are modulated directly onto the subcarriers using OFDM.

6.3 Simulated Performance Analysis

In order to find the optimal grouping policy for our testbed we carry out simulations. To conduct performance comparisons for different grouping calibration schemes, we use the MSE of calibrated channel matrices as our metric. We modeled the transmit and receive calibrated parameters, thus, we are able to compare the true calibrated coefficients $\mathbf{f}$ to the estimated ones $\hat{\mathbf{f}}$.

$$\mathrm{MSE} = \frac{\mathbb{E}\left[\|\hat{\mathbf{f}} - \mathbf{f}\|^2\right]}{M-1} \tag{6.4}$$

We fix the noise variance to the thermal noise of one subcarrier (15kHz) at N_0=-132dBm. Thus, the performance of different grouping methods is only driven by the different values at the transmit power per RRU. We assess numerically the performance of the proposed group-based fast calibration method from Section III at 2.58 GHz. We use the MSE of the calibrated channel normalized by the total number of active RRUs. Some important parameters that impact the MSE of the calibration coefficient estimates are evaluated.

Fig. 6.3a illustrates the performance results from the three different grouping schemes. The MSE curve with the "Interleaved" grouping method shows that the interleaving of the RRUs ensures that the channel from a group to the rest of the RRUs is as well conditioned as possible. Through our simulations we noticed how crucial is the geometry of the environment to the effective calibration coefficients estimation. For this experiment we consider 6 RRUs in row and a double door blocking the first two RRUs from the rest like in Fig. 5.7. Changing the inter-RRU distance $d_{i,j}$ by only 10cm may result in destructive interference among almost all the possible pairs of RRUs based on our 2-ray interference channel model. Thus, the benefits of our proposed "Interleaved" grouping scheme no longer hold, Fig. 6.3b.

Furthermore, in Fig. 6.4, we verify the fact that the performance improves when the group sizes are allocated more equitably to the minimum group size as in grouping scheme 2-2-2-2-2-2. This can be verified by looking at the condition number of $\boldsymbol{\mathcal{Y}}(\mathbf{P})$ in (3.7). The condition number of matrices plays an important role in solving systems of linear equations such as the linear least squares method. It measures the sensitivity of the solution of a problem to data quality. It provides an approximate upper bound on the error in a computed solution. In 6-6 scheme, the matrix can be poorly conditioned for inversion so it is more sensitive to machine's relative round-off errors made during the LS solution process, Fig. 6.5. Also, we can clearly see from the curves representing 4-4-4 and 2-4-6 that even if we split the RRUs into the same number of groups, grouping them equitably is favorable.

The results presented at Fig. 6.6 show how strongly a condition number depends on the size of the matrix. Increasing the number of RRUs results in larger linear system of equations and consequently a more accurate approximation of the LS solution. The curves show that the matrices representing the largest possible grouping, the condition number of which is very high, are ill-conditioned, so the LS estimation process can generate solutions with a large error, resulting in a calibration matrix with poor accuracy. On the contrary, the matrices formed by the minimum-size grouping scheme, have smaller condition numbers, which means that they are well-conditioned matrices for which the LS estimation process, after a few iterations, gives the estimate with a minor error.

6.4 Summary

In this chapter, we presented the emulation of C-RAN testbed in order to provide the ground truth through simulations for the efficiency of our proposed grouping schemes. We applied a 2-ray channel model and observed that the performance of each grouping scheme is highly sensitive to the geometrical characteristics of the area where the RRUs are distributed. As evaluation metrics we used the MSE and the condition number.

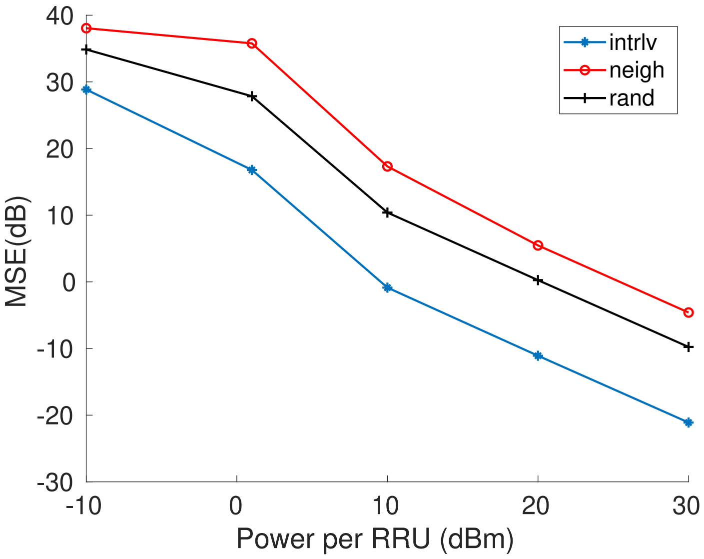

(a) Constructive interference ($d_{i,j}$=5.4m)

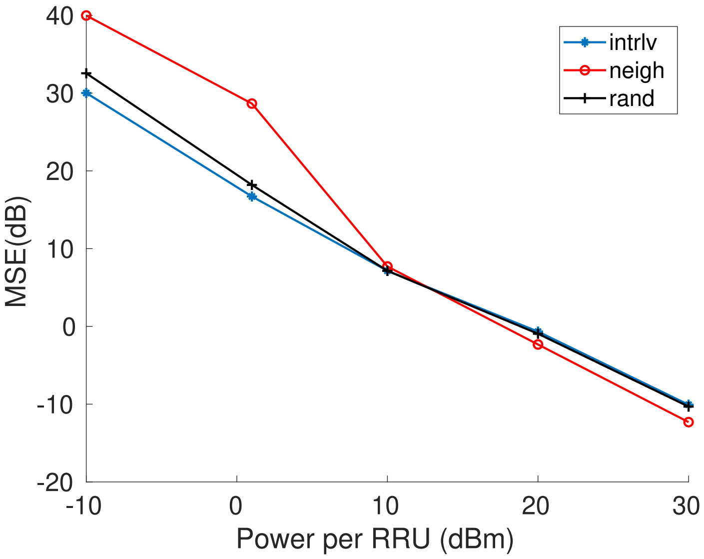

(b) Destructive interference ($d_{i,j}$=5.5m)

Figure 6.3 – MSE of estimated calibration matrix over transmit power per RRU (M=6 RRUs).

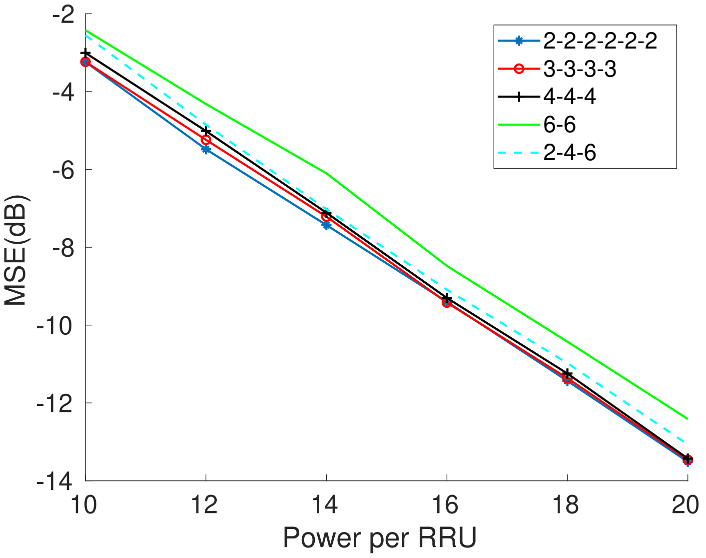

Figure 6.4 – MSE of estimated calibration matrix over transmit power per RRU (interleaving M=12 RRUs - LOS case).

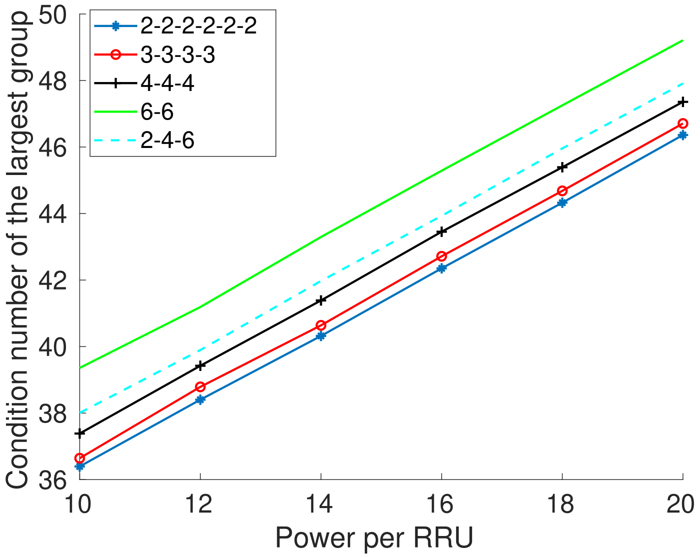

Figure 6.5 – Condition number of 5 different grouping schemes over transmit power per RRU (interleaving M=12 RRUs - LOS case).

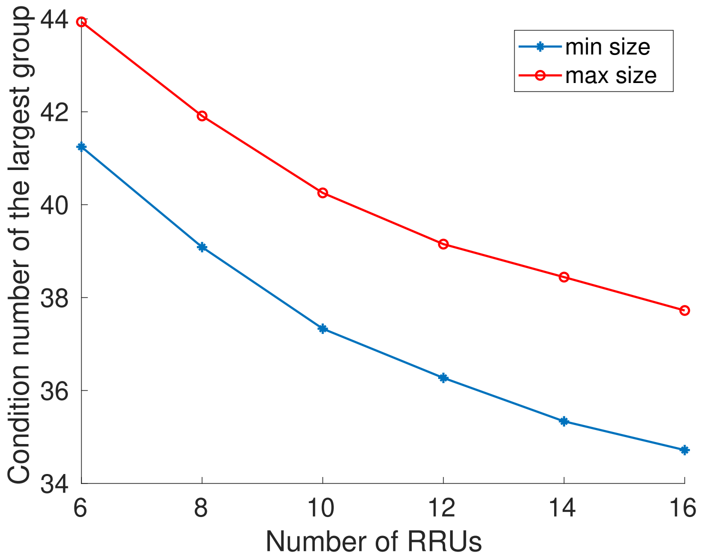

Figure 6.6 – Condition number of the largest grouping over the total number of distributed RRUs (LOS case).

Chapter 7

Low-cost MIMO antenna assessment based on OAI

During the first year of my PhD studies we developed a testbed in order to facilitate the evaluation of relative calibration in a MISO-TDD system and simultaneously assess the performance of the MIMO antenna prototypes designed by our team in Orange labs.

7.1 Measurement Setup

The experimental results presented in this chapter were obtained using Eurecom's open-source hardware and software development platform OpenAirInterface (OAI) [94], and a rail moving with a Digital Servo Amplifier, SERVOSTAR 300 [95], Fig. 7.1, along with a Rosier servo motor controlling the movement [96], Fig. 7.2.

The measurements in this work were carried out using EXPRESSMIMO2 Peripheral Component Interconnect (PCI) Express (PCIe) boards Fig. 7.3, inside a controlled laboratory environment. The ExpressMIMO2 motherboard features four high-quality RF chipsets from Lime Micro Systems (LMS6002), which are LTE-grade MIMO RF front-ends for small cell eNBs. The radio frequency equipment can be configured for both TDD or FDD operation with channel bandwidths up to 20 MHz covering a very large part of the available RF spectrum (250MHz-3.8GHz) and a subset of LTE MIMO transmission modes. Fig. 7.4 represents the measurement setup. Two ExpressMIMO2 boards acting as node A and one acting as node B were connected with cables for both time and frequency synchronization as depicted in Fig. 7.5.

The antennas used at node A are prototypes designed by the Antenna team at Orange labs. Emerging technologies such as 3D printing [97] and plastronic, offering new degrees of freedom and more flexibility, are used. The antenna array in Fig. 7.6 is printed on a Printed Circuit Board (PCB) while the prototype in Fig. 7.7 uses innovative methods to print the antennas directly on a plastic box, like Laser Direct Structuring (LDS) [98]. This method is highly promising for optimizing the volume in small devices such as femtocells. The prototype of plastronic gateway includes 8 dual-band antennas (2.5 GHz & 5 GHz) for Wi-Fi and LTE technologies. The antennas are printed on a plastic box

Figure 7.1 – SERVOSTAR 300

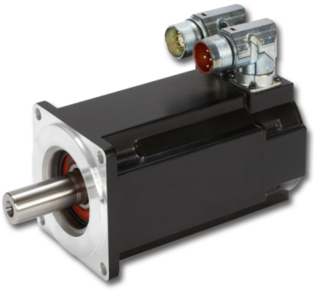

Figure 7.2 – Servo Motor

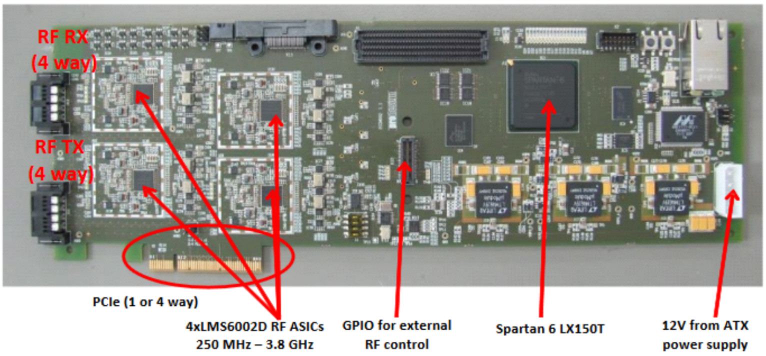

Figure 7.3 – ExpressMIMO2 motherboard

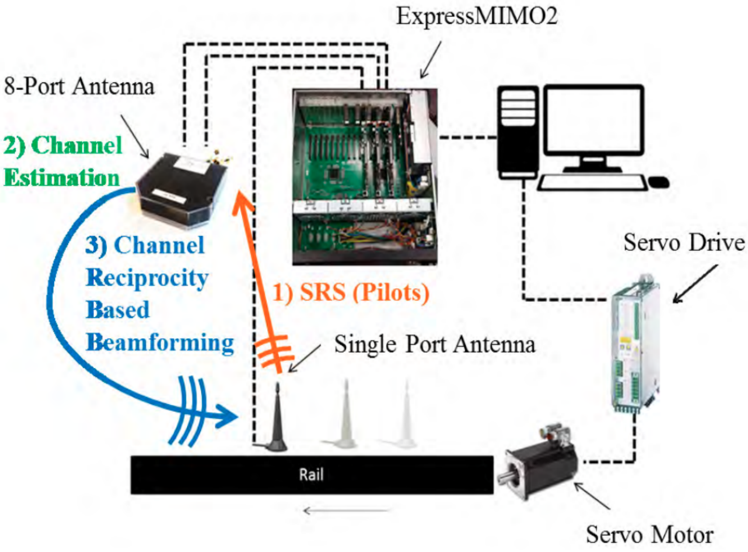

Figure 7.4 – Measurement Setup

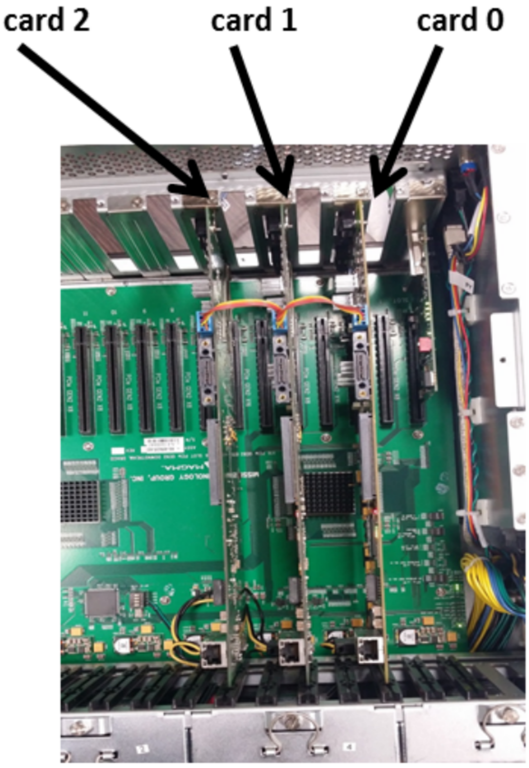

Figure 7.5 – ExpressMIMO2 Synchronization Setup

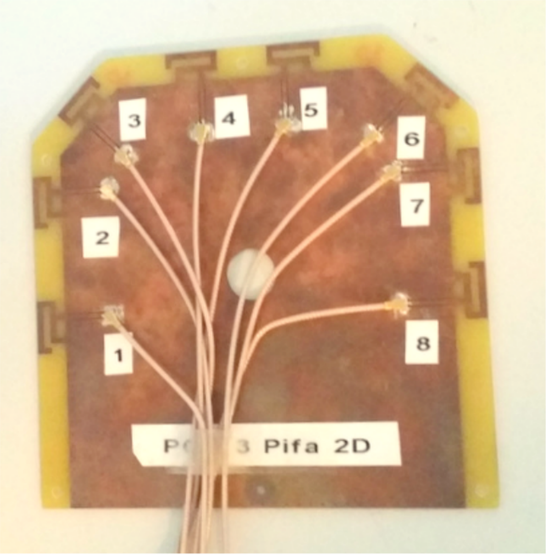

Figure 7.6 – PCB antenna array

made by polycarbonate using LDS technology.

Four out of the eight antennas from the prototype are connected to card 0 and the rest are connected to card 1. At card 2 we have connected a single antenna which was attached upon the rail. We have used two different types of antennas for this purpose:

1. An LTE magnetic antenna-SMAm, Fig. 7.8.
2. A smartphone-like antenna [99], Fig. 7.9.

The experiments were carried out using LTE-like OFDM frames. Each OFDM symbol consists of 512 carriers, out of which 300 are filled with random QPSK symbols and the rest are set to zero. An extended cyclic prefix (ECP) of 128 samples is added to each OFDM symbol after the 512-point Inverse Fast Fourier Transform (IFFT). The sampling rate is 7.68 MSPS, resulting in an effective bandwidth of 4.5 MHz. Ten subframes each with 12 ECP-OFDM symbols compose the TDD OFDM frame. When one antenna of node A is on transmission, other antennas of the same side keep silent so that orthogonality in the time domain is achieved. The carrier frequency is 2.68 GHz and the transmission power is of around 10 dBm. The power is chosen to insure a good level of reception in the whole room while avoiding saturation of receiving RF chains. Both transmit and receive gains on all the RF chains are set to 15 dB.

7.2 Experimental Results

The reciprocity model used for these experiments belongs to the UE-involved calibration methods such as [23–25, 100], which enable bi-directional transmission of pilots between the BS and the UE. Both sides estimate their UL channels and then the BS calculates

Figure 7.7 – LDS antenna prototype

Figure 7.8 – Magnetic antenna

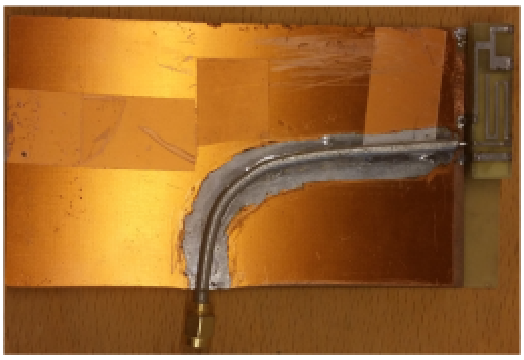

Figure 7.9 – Smartphone antenna

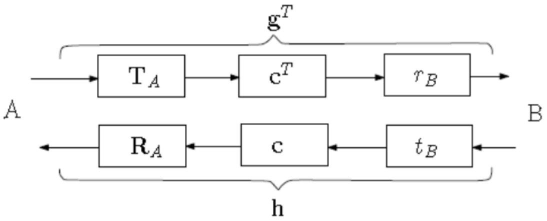

Figure 7.10 – MISO reciprocity model

the calibration coefficients based on its own UL channel estimates. We consider a point-to-point MISO-TDD communication system involving two devices A and B with M antennas and 1 antenna respectively, as illustrated in Fig. 7.10.

The channel seen by transceivers in the digital domain (the composite channel), is comprised of the physical channel c, assumed reciprocal in both UL and DL, and filters modeling the imperfections of the transmit RF hardware (e.g., power amplifiers (PA)), ($\mathbf{T}_A$ and t_B), and the receive RF hardware (e.g, low-noise amplifiers (LNA)), ($\mathbf{R}_A$ and r_B). We note $\mathbf{T}_A$ (matrix of size MxM) as the system function in the frequency domain of the transmit block at node A from the digital-to-analog converter (DAC) to the antenna array. The diagonal elements represent the gains on each transmit chain whereas the off-diagonal elements correspond to the RF chain on-chip crosstalk and the antenna mutual coupling. We consider the ideal case, where $\mathbf{T}_A$, t_B, $\mathbf{R}_A$ and r_B are all identity filters (no crosstalk/mutual coupling) and carrier frequency at both sides is identical. Also, the filters modeling the amplifiers are assumed to remain constant over the observed time horizon. $\mathbf{R}_A$ is the system function of the receive block at node A and includes the characteristics from the antenna array to the analog-to-digital converter (ADC). t_B and r_B represent the transmit and receive chains at node B respectively. The measured UL and DL channels between nodes A and B, represented by $\mathbf{g}^T$ and $\mathbf{h}$, are thus modeled as:

$$\begin{aligned} \boldsymbol{g}^T &= r_B\boldsymbol{c}^T\boldsymbol{T}_A \\ \boldsymbol{h} &= \boldsymbol{R}_A\boldsymbol{c}t_B \end{aligned} \tag{7.1}$$

Eliminating c from (7.1), we obtain:

$$\boldsymbol{g}^T = r_B(\boldsymbol{R}_A^{-1}\boldsymbol{h}t_B^{-1})^T\boldsymbol{T}_A = \boldsymbol{h}^T\frac{r_B}{t_B}\boldsymbol{R}_A^{-T}\boldsymbol{T}_A = \boldsymbol{h}^T\boldsymbol{F} \tag{7.2}$$

where $\boldsymbol{F} = \frac{r_B}{t_B}\boldsymbol{R}_A^{-T}\boldsymbol{T}_A$ includes all the hardware properties on both sides and forms the *calibration matrix.*

Let us describe how the calibration matrix is estimated. We assume that the matrix $\boldsymbol{F}$ is diagonal. This assumption has been validated in [101], where it has been shown experimentally that the magnitude of the off-diagonal elements is at least 30dB below the one of the main diagonal and that there is thus almost no difference in beamforming perfomance.

We consider an orthogonal frequency division multiplexing (OFDM) system where for each subcarrier the channel can be regarded as flat fading. The signal model is given by:

$$\begin{aligned} y_b &= \boldsymbol{g}^T \boldsymbol{s}_a + n_a \\ \boldsymbol{y}_a &= \boldsymbol{h} s_b + \boldsymbol{n}_b \end{aligned} \tag{7.3}$$

where $\boldsymbol{y}_a \in \mathbb{C}^M$ and $y_b \in \mathbb{C}$ are the received signals at node A and B respectively. $\boldsymbol{s}_a \in \mathbb{C}^M$ and $s_b \in \mathbb{C}$ are the known transmit pilot sequences on the concerned subcarrier whereas the noise n_a and $\boldsymbol{n}_b$ are circularly-symmetric complex Gaussian random variables following $\mathcal{CN}(0, \sigma_n^2)$ and $\mathcal{CN}(0, \sigma_n^2 \boldsymbol{I})$ respectively.
The channel responses can be estimated using received pilots. We adopt here the least square (LS) estimators as they do not require any statistical channel information, given by:

$$\begin{aligned} \hat{\boldsymbol{g}}^T &= y_b \boldsymbol{s}_a^H (\boldsymbol{s}_a \boldsymbol{s}_a^H)^{-1} \\ \hat{\boldsymbol{h}} &= \boldsymbol{y}_a \frac{s_b^*}{\|s_b\|^2} \end{aligned} \tag{7.4}$$

Since LS estimators are linear, the estimation errors remain circular-symmetric Gaussian variables following $\mathcal{CN}(0, \sigma_n^2 (\boldsymbol{s}_a^* \boldsymbol{s}_a^T)^{-1})$ and $\mathcal{CN}(0, \frac{\sigma_n^2}{\|s_b\|^2} \boldsymbol{I})$ respectively.

Substituting (7.4) in (7.2) we get the diagonal estimation of the calibration matrix $\boldsymbol{F}$.

7.2.1 Feasibility of relative calibration method through beamforming SNR measurements

In this work, published in [102], we studied the transmit time reversal beamforming in a $8x1$ MISO communication system at 2.68 GHz. We proved the feasibility of a relative calibration method through beamforming SNR measurements. Moreover, we evaluated the performance of an antenna selection scheme at the transmit side as a low-cost low-complexity alternative to capture many of the advantages of multi-antenna systems. The measurements showed that the relative calibration method is performing almost optimal and that the complexity can be significantly reduced by using antenna selection.

The experimental results were taken through the following process:

- Move the receive antenna to the middle of the rail.
- Execute the calibration phase and save the calibration matrix.
- Move the receive antenna to the start position (one of the 2 edges) and begin the transmission phase which is repeated for 200 positions.
- For each position compute the beamforming SNR under the ideal and the diagonal $\boldsymbol{F}$ estimation assumptions.
- Average spatially and obtain the final beamforming SNR values.

- Compute the cdf by averaging the received SNR over the 300 subcarriers.

We compare the beamforming performance based on different CSIT acquisition methods. When the calibration matrix $\boldsymbol{F}$ is obtained, it can be used in the transmission. Hence, we estimate the relative DL CSI by using only UL pilots and $\boldsymbol{F}$, (7.2), without any feedback. Thus, we can use relative downlink channel estimation to calculate the beam weights and then send the beamformed data. Let us consider the signal received by B as:

$$y = \boldsymbol{g}^T \boldsymbol{s} + n \tag{7.5}$$

We adopt the conjugate beamforming which consists in using the conjugate-transpose of the relative channel estimates as a linear precoder on the forward link. Thus, the precoded transmitted symbol $\boldsymbol{s}$ is given by:

$$\boldsymbol{s} = \frac{(\hat{\boldsymbol{g}}^T)^H}{\|\hat{\boldsymbol{g}}\|} x = \frac{\hat{\boldsymbol{g}}^*}{\|\hat{\boldsymbol{g}}\|} x \tag{7.6}$$

We compare the beamforming SNR noted by γ under 3 different assumptions.

- Ideal
  We assume node A knows $\hat{\boldsymbol{g}}$ measured by node B. The beamforming SNR is given by:

$$\gamma_{ideal} = \frac{\|\boldsymbol{g}^T \hat{\boldsymbol{g}}^*\|^2}{\|\hat{\boldsymbol{g}}\|^2} \frac{\sigma_x^2}{\sigma_n^2} \tag{7.7}$$

- No calibration
  Under this assumption, the transceiver hardware is considered totally reciprocal and $\boldsymbol{h}$ is considered to be equal to $\boldsymbol{g}$, thus no calibration is needed. The SNR is:

$$\gamma_{no\,calib} = \frac{\|\boldsymbol{g}^T \hat{\boldsymbol{h}}^*\|^2}{\|\hat{\boldsymbol{h}}\|^2} \frac{\sigma_x^2}{\sigma_n^2} \tag{7.8}$$

- Diagonal $\boldsymbol{F}$ estimation
  The RF chain crosstalk and the antenna mutual coupling are ignored and the calibration matrix is assumed to be diagonal, noted by $\hat{\boldsymbol{F}}$. The beamformming SNR is:

$$\gamma_{diag} = \frac{\|\boldsymbol{g}^T (\hat{\boldsymbol{h}}^T \hat{\boldsymbol{F}})^H\|^2}{\|\hat{\boldsymbol{h}}^T \hat{\boldsymbol{F}}\|^2} \frac{\sigma_x^2}{\sigma_n^2} \tag{7.9}$$

We compare the 3 different beamforming SNRs shown above with the the average received SNR over all the transmit antennas.

$$\gamma_{SISO,mean} = \frac{\sum |\hat{\boldsymbol{g}}_i^*|^2}{N} \frac{\sigma_x^2}{\sigma_n^2} = \frac{\|\hat{\boldsymbol{g}}^*\|^2}{N} \frac{\sigma_x^2}{\sigma_n^2} \tag{7.10}$$

Fig. 7.11 and Fig. 7.12 illustrate the beamforming SNR from the magnet foot antenna and the smartphone one, respectively. The total transmit power is fixed for both SISO

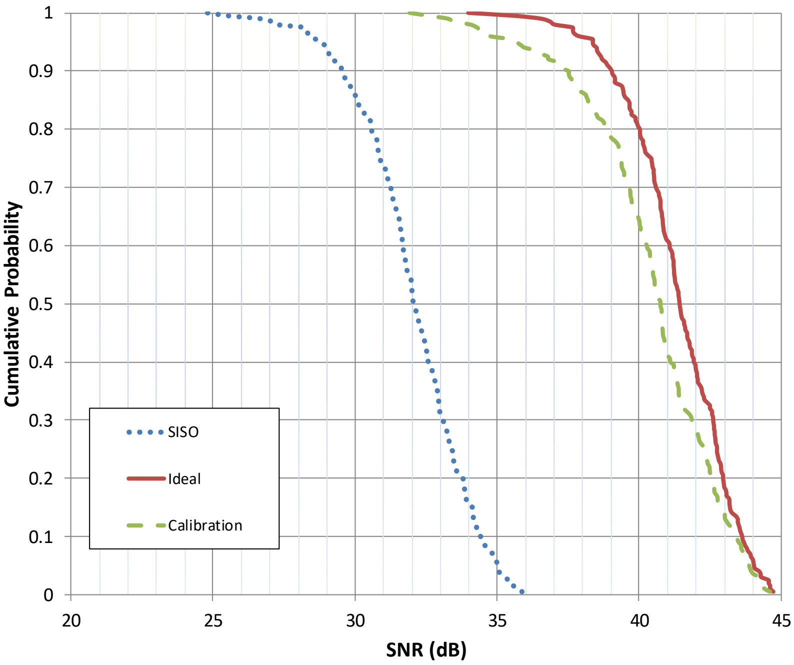

Figure 7.11 – CDF of SNR (magnetic Rx)

and MISO cases. As we can see the expected beamforming gain of 9dB[1] compared to its corresponding SISO case is achieved. We observe a degradation in the performance of the system when the smartphone antenna acts as node B. This happens due to lower efficiency and gain of the smartphone antenna. Also, the omnidirectional radiation pattern of the magnetic antenna matches better to this measurement setup. However, the deviation between the two curves representing the beamforming SNR under the ideal assumption and the diagonal $\boldsymbol{F}$ estimation one for both receive antennas is the same meaning that our calibration method works perfectly regardless the different radiation patterns and gains.

Beamforming is the method used to create the radiation pattern of the antenna array by adding constructively the phases of the signals in the direction of the mobiles desired. Geometric corrections are easy, but instrumental corrections must be found. Beamforming can severely degrade in the presence of some signal steering vector errors. These errors can be caused by a number of reasons such as array calibration imperfections, non-linearities in amplifiers, A/D converters and other hardware. All the measures that have to be taken to protect against the aforementioned imperfections require extra signal processing time and more power consumption. Thus, we decided to check if by selecting two or four out of the eight antennas existing in a prototype, we could get similar

---

[1] In a $N \times M$ MIMO system the array gain is $10 * log(M)$ dB on receive side and $10 * log(N)$ dB on transmit side if transmit channel is known.

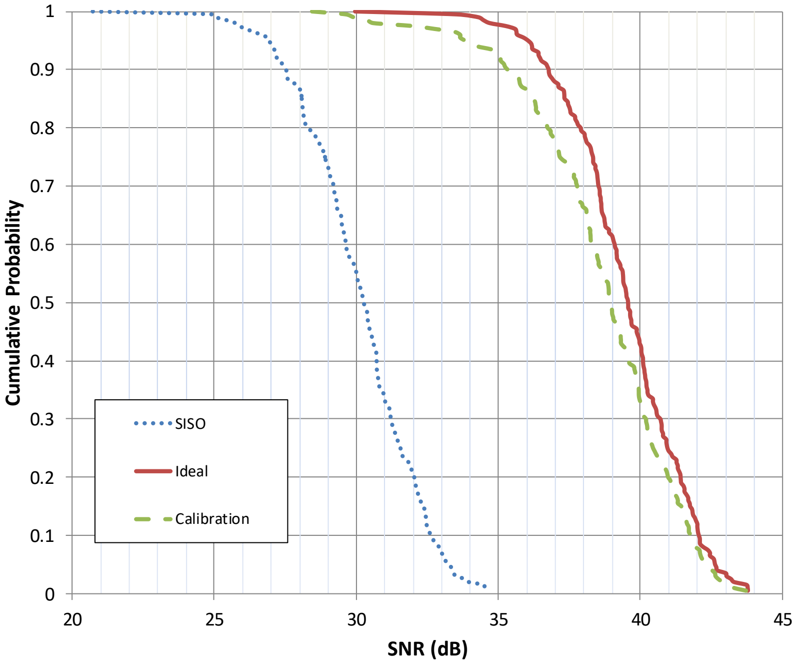

Figure 7.12 – CDF of SNR (smartphone Rx)

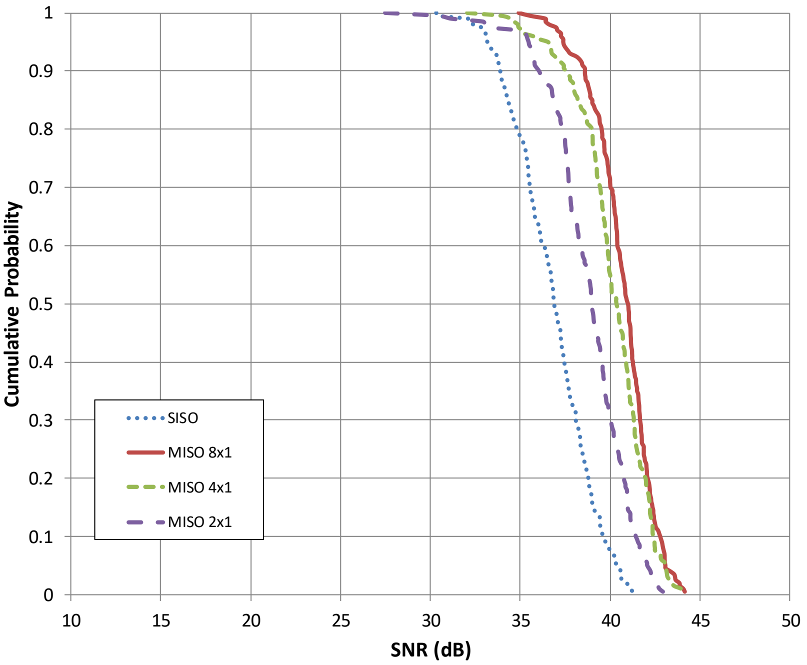

Figure 7.13 – Beamforming SNRs (adaptive scheme)

beamforming gains. Such that, if the circumstances allow it, in terms of coverage, we may decrease the number of antennas used for transmission to a single user.

We performed beamforming techniques using the diagonal $\boldsymbol{F}$ estimation for 200 different positions of the single receive antenna under two different scenarios:

1. *Adaptive antenna selection.* Having performed 8 SISO transmissions for each antenna element on the prototype and having measured the received SNR at node B for each SISO case, we form a vector in descending order from the identities of the antennas having the strongest signal to the antennas providing low SNR performance. Node A acquires this information through reciprocity channel and uses it to perform beamforming using the 2 or 4 high-performance antennas.

2. *Fixed antenna selection.* In this scenario we pick each time the front 2 or 4 elements from the antenna array.

The results we get after the implementation of those two scenarios are illustrated in Fig. 7.13 and Fig. 7.14. We observe that by selecting two or four “best” antennas we get quite similar beamforming gains compared to transmitting from all the available antennas. So, we can exploit it to save power and signal processing resources.

In [103] our main goal is to prove the efficiency of our relative calibration algorithm and assess the measurement setup by verifying the 3 dB increase on the beamforming

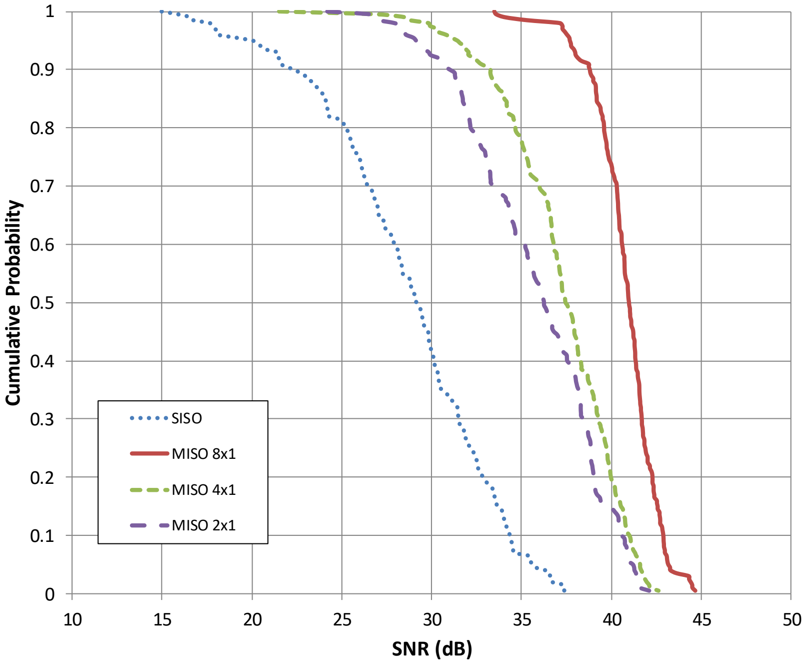

Figure 7.14 – Beamforming SNRs (fixed scheme)

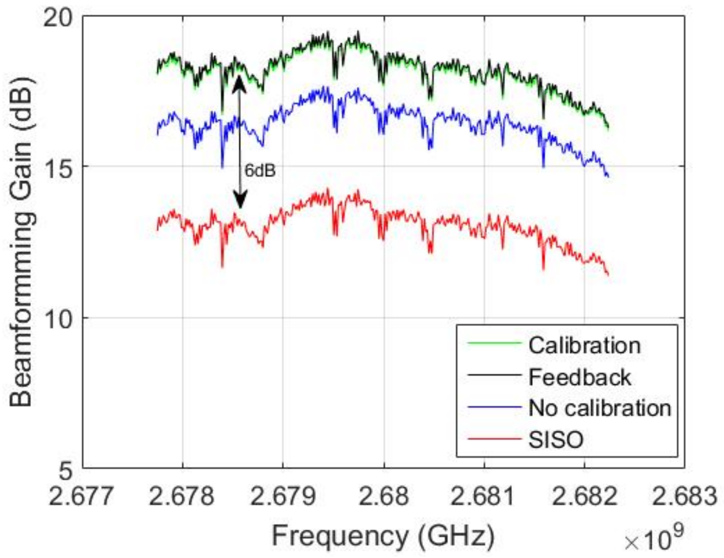

Figure 7.15 – Beamforming Gain between SISO and 4x1 MISO

gain when doubling the number of antennas. We repeat the bi-directional transmissions for 20 different positions along the 4 meters long rail and afterwards we average the measured SNR in the space domain.

Our goal is to increase the channel capacity through SNR. According to the channel capacity formula (7.11) we should have a 3 dB increase of the SNR when doubling the number of antennas at the transmitter.

$$C = \sum_{i=1}^{min(M,N)} B_i \log(1 + SNR_i) \tag{7.11}$$

where B is the bandwidth, M and N the number of antennas at the receiver and the transmitter respectively, and SNR represents the signal to noise ratio.

Fig. 7.15 illustrates a 6 dB increase on the SNR for the 4x1 MISO case compared to the SISO one. We also observe that the calibration method achieves the same beamforming gain compared to the feedback method ("ideal" case). Both calibration and feedback methods show a 2 dB improvement of the SNR compared to a no calibration measurement.

7.2.2 Validation of a low-cost SDR testbed for MIMO performance assessment

The aim of our work in [104] is to confirm the effectiveness of the ExpressMIMO2 testbed by the reproducibility of the measurements, which have been obtained using the plastronic gateway with eight antennas in Fig. 7.7. Again the eNB is in a static position at 4m away from the center of the rail. The UE uses a monopole reference antenna embedded on an automated 4m long rail to perform statistic measurements in different propagation channels. Measurements are performed in a line-of-sight (LOS) configuration.

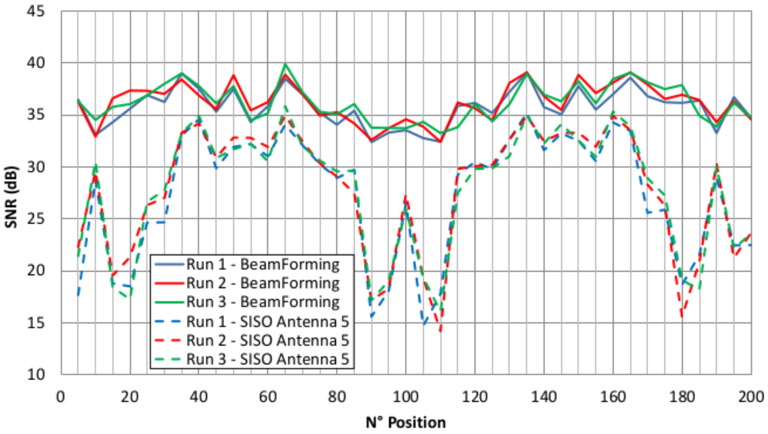

Figure 7.16 – Dispersion between 3 identical 8x1 MISO and SISO transmissions

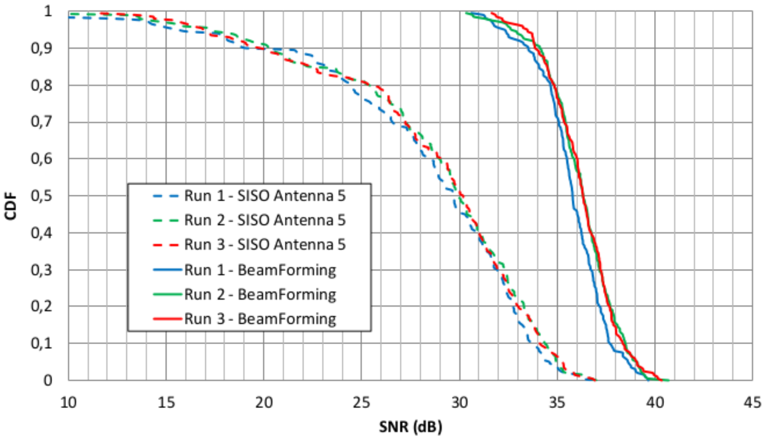

Figure 7.17 – Beamforming gain between 4x1 MISO and SISO methods

In order to determine reproducibility of the test method we repeated three times the same test. The rail moves 100 positions forward and 100 positions backwards with a 3 cm step and we collect the SNR measurements for all these 200 positions.

Fig. 7.16 presents the beamforming gain results by transmitting from all the 8 antennas of the prototype against using only one particular antenna. We observe that for both cases and for all the 3 runs, we get a very low dispersion among measurements. The overall average dispersion is 1.3 dB. The symmetrical pattern of the curve is justified by the two-way movement of the receiver along the rail.

Furthermore, Fig. 7.17 shows the Cumulative Distributed Function (CDF) for the full 200 measurements where we can see that the beamforming gain is the same for all three runs. Thus, the good accuracy of our testbed and the reproducibility of our relative calibration method are confirmed.

7.2.3 Single-carrier Spatial Modulation for the Internet of Things

In this section we present our contribution to the work published in [105]. In this paper, the authors proposed innovative solutions to boost the data rate between small connected objects and the 5G mobile network using spatial modulation (SM), single-carrier waveform and compact reconfigurable antennas at the object side.

We carry out experiments in the same testbed illustrated in Fig. 7.4 but in non-line-of-sight (NLOS) conditions, in order to prove that although 5G is based on multi-carrier modulation which is not compatible with spatial modulation [106], the mobile networks have the potential to support single-carrier modulations, with bandwidths as large as several MHz.

In these experiments, the receiver sends pilots called sounding reference signals (SRS) in the uplink direction. The transmitter uses these pilots to estimate the uplink channel. Channel reciprocity is exploited to deduce the downlink channel. The transmitter precodes its downlink data and pilots with a maximum ratio transmission (MRT) precoder, to beamform the signal towards the receiver. Note that MRT is equivalent to time reversal or to transmit matched filter pre-filtering (applied to OFDM instead of a single-carrier modulation) [107]. During the experiment, 15 different positions of the receiver are tested, along a rail, and all in NLOS of the transmitter. For each position, the receiver measures the frequency response of the received beamformed channel thanks to the downlink precoded pilots. The measurements were carried out inside a controlled laboratory environment. Fig. 7.18 illustrates the propagation environment during the experiments. Non-line-of sight propagation is chosen to create multi-path propagation. In such environment, the channel impulse response has several delayed taps. Hence, a single-tap receiver trying to demodulate a single-carrier modulation would suffer from inter-symbol interference. Finally, we apply an IFFT to the frequency response of the received beamformed channel, to obtain the corresponding filter in the time domain.

Fig. 7.19 illustrates the measured frequency response and the corresponding impulse response, for the received beamformed channel measured at the 15th position. We observe that the beamformed channel is nearly a single-tap channel. We also evaluate the ratio between the useful signal and the inter-symbol interference (SIR) that would be undergone by a single-tap receiver demodulating a single-carrier modulation at 5 MHz. As illustrated in Fig. 7.20, for all tested positions, this value exceeds 20 dB. This is largely sufficient to support a single-carrier modulation with 16 QAM. More precisely, for the worst case position (position number 3), we simulate the transmission of 1.500.000 random bits over a single-carrier modulation transmission with a Raised Root Cosine (RRC) filter, 16 QAM, and a single-tap receiver. For this simulation we chose an extreme value of Roll Off factor (0.001), to test the worst case scenario. We use the same simulation methodology detailed in [108], except that we use the current measured beamformed channel impulse response. The resulting measured bit error rate over 1.500.000 bits is zero. This means that the attainable BER, in this case, is estimated to be lower than 10^{-5}.

This confirms that current standards for mobile networks have the potential to support single-carrier modulations, with bandwidths as large as several MHz. Note that, by

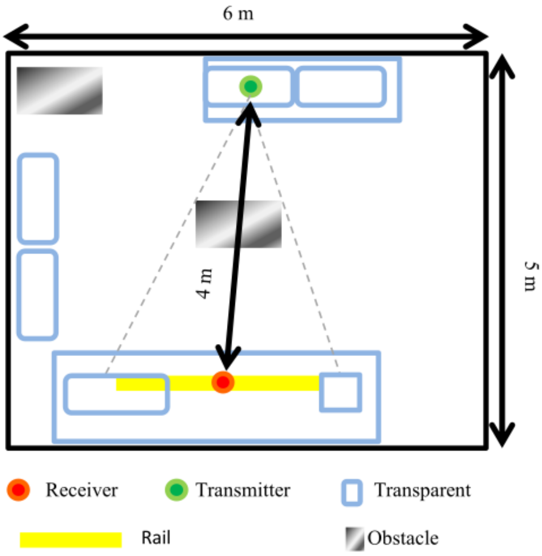

Figure 7.18 – NLOS propagation

applying maximum ratio combining (MRC) at the receiver side (instead of MRT at the transmitter side), in an uplink transmission (instead of a downlink transmission) we would have obtained the same result: the channel after equalization would have been single-tap. This means that after a receive matched filter, the channel is single-tap and compatible with a single-carrier modulation and a single-tap detector.

7.3 Summary

In this chapter, we presented the testbed developed inside a controlled laboratory environment using the OAI platform and ExpressMIMO2 motherboards. We assessed various MIMO antenna prototypes through SNR measurements in LOS/NLOS propagation conditions and we studied the potential to support single-carrier modulations in the 5G technology.

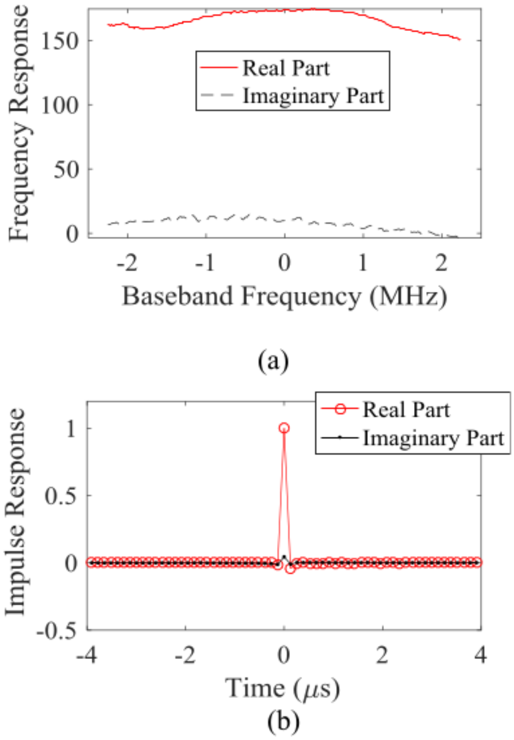

Figure 7.19 – Received beamformed channel for the 15th position of the UE. (a) Frequency response. (b) Impulse response.

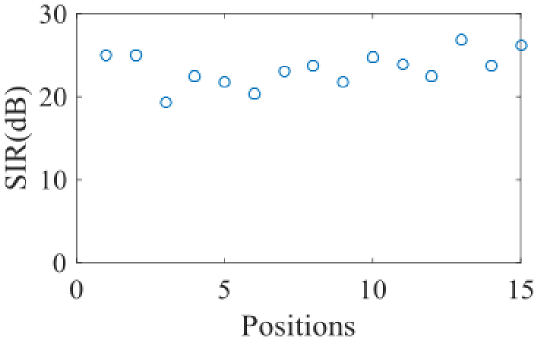

Figure 7.20 – SIR with single-carrier modulation.

Chapter 8

Conclusion and Future Work

This thesis mainly concerns deploying a low-cost distributed antenna system based on the OpenAirInterface 5G platform and evaluating the performance of the existing reciprocity calibration schemes in a real-time environment. Correctly and efficiently calibrate the transmit and receive RF asymmetry is essential for reciprocity based CSIT acquisition in TDD distributed massive MIMO systems. Also, accurate timing synchronization and phase coherence between each RF chain is a crucial prerequisite for the deployment of a distributed massive MIMO network. Many applications based on MIMO transmissions such as beamforming methods, require high-precision synchronization and phase coherence between each RF chain.

We describe the system architecture of our C-RAN testbed deployed at Eurecom using OpenAirInterface software and inexpensive commodity hardware. We discuss the synchronization and calibration algorithms implemented in our network and we analyze the hardware problems we had to overcome. We achieve to maintain OTA synchronization between several RRUs and confirm the efficiency of the proposed fast calibration schemes based on RRU grouping in real environment. Our results are based on the variance of the time-domain calibration elements and illustrate that the FC algorithm with equally partitioned groups outperforms the existing Argos, Rogalin and Avalanche methods. Moreover, we present the case where the overall estimation performance of our FC algorithm improves when we try to minimize the size of the largest RRU group. Finally, we prove through real-time measurements that the interleaved grouping of the RRUs results in performance gains.

We also model our OpenAirInterface C-RAN testbed through simulations in order to provide a ground truth for the evaluation of the proposed FC scheme using channel measurements. We show that the performance of each grouping scheme is highly sensitive to the geometrical characteristics of the area where the RRUs are distributed. Moreover, we prove, through MSE and condition number metrics, that the overall estimation performance of our group-based FC algorithm improves when we try to minimize the size of the largest RRU group with equally partitioned groups.

In addition to these real-time experiments carried out in a distributed antenna system, we deploy a MISO-TDD testbed inside a controlled laboratory environment using the open-source hardware and software development platform OpenAirInterface, ExpressMIMO2 motherboards and a rail moving with a Digital Servo Amplifier, SERVOSTAR 300 along with a Rosier servo motor controlling the movement. We study the beamforming performance after applying OTA reciprocity calibration methods over a long time period. We use the experimental results in oder to assess the performance of MIMO antenna prototypes built with LDS techniques and to investigate the perspective of using single-carrier modulations in the 5G technology.

Building a distributed massive MIMO system is a hard and challenging process. Our C-RAN testbed at Eurecom is not really massive but we managed to keep at least 8 RRUs synchronized in time and frequency for long periods. This is quite an achievement considering the OTA synchronization protocol which is not as reliable or stable as the IEEE 1588 precision time protocol with SyncE and the unfavorable propagation conditions during busy hours in the corridors at Eurecom. In the future, we would like to achieve time synchronization across all the 20 RRUs distributed over the 2 floors and study the performance of various grouping schemes when RRUs from different floors are included.

While some interesting results have been established in this thesis, some issues are left unsolved in order to complete the communication of our distributed antenna system with UEs. We managed to integrate the real-time calibration process into the OAI platform without breaking neither the multi-thread parallelization nor the RRU synchronization. We had successfully connected to the core network but as soon as the UE was attached to the RRUs, the connection was suddenly broken. Due to lack of time we did not resolve this issue. Moreover, since OAI has recently moved to the 5G area, we would like to adapt our implementations (precoding, reciprocity calibration, RRU synchronization) to the new specifications and the tighter timing requirements.

Since 2018, base stations of fully digital massive MIMO arrays with 64 transceiver chains are commercially deployed in many countries. Massive MIMO is now a reality. In [109] the authors propose a few research directions for the future of massive MIMO (e.g., cell-free massive MIMO, very large aperture massive MIMO). Cell-free massive MIMO combines the distributed MIMO and massive MIMO concepts, with hundreds of RRUs distributed over a wide area serving autonomous users. Extremely large aperture array is a new antenna deployment strategy which provides truly massive spatial resolution with hundreds of antennas distributed along existing construction elements such as the facade of a building. Our group-based calibration schemes could be applied to these promising research topics. Study the performance of our reciprocity calibration algorithms for a very large number of RRUs and for topologies with different geometrical characteristics would be an extremely interesting topic.

Furthermore, our group-based reciprocity calibration schemes could be integrated into the Intelligent massive MIMO concept. We could use machine learning to dynamically optimize the RRU grouping in order to improve the performance of the existing group-based algorithm, considering the network demands at a given time. In Chapter 6 we observed that the geometrical characteristics and the propagation conditions affect significantly the way we form the RRU groups and model our system. ML is especially powerful in modeling such difficult characteristics in a system by learning from a large amount of data and even enable new, more efficient, grouping schemes. Maintaining a calibrated status in a distributed massive MIMO system is an important task and usually it is hard to decide the pace with which the calibration process will be repeated. ML would help the system to automatically switch between different time intervals of reciprocity calibration application. This way, possible waste of resources allocated for the hardware assymetry estimation could be avoided.

Bibliography

[1] "What is MIMO?" https://www.grandmetric.com/2018/02/07/what-is-mimo/.

[2] "Cisco Annual Internet Report (2018–2023) White Paper," https://www.cisco.com/c/en/us/solutions/collateral/executive-perspectives/annual-internet-report/white-paper-c11-741490.html.

[3] "Mobilizing mmWave with 5G NR," https://www.qualcomm.com/invention/5g/5g-nr/mmwave.

[4] "802.11ac MU-MIMO: Bridging the MIMO Gap in Wi-Fi," https://www.qualcomm.com/media/documents/files/802-11ac-mu-mimo-bridging-the-mimo-gap-in-wi-fi.pdf.

[5] S. Gollakota, S. D. Perli, and D. Katabi, "Interference alignment and cancellation," in *Proceedings of the ACM SIGCOMM 2009 conference on Data communication*, 2009, pp. 159–170.

[6] H. V. Balan, R. Rogalin, A. Michaloliakos, K. Psounis, and G. Caire, "Achieving high data rates in a distributed mimo system," in *Proceedings of the 18th annual international conference on Mobile computing and networking*, 2012, pp. 41–52.

[7] H. S. Rahul, S. Kumar, and D. Katabi, "Jmb: scaling wireless capacity with user demands," *ACM SIGCOMM Computer Communication Review*, vol. 42, no. 4, pp. 235–246, 2012.

[8] T. L. Marzetta, "Noncooperative cellular wireless with unlimited numbers of base station antennas," *IEEE transactions on wireless communications*, vol. 9, no. 11, pp. 3590–3600, 2010.

[9] H. Yang and T. L. Marzetta, "Performance of conjugate and zero-forcing beamforming in large-scale antenna systems," *IEEE Journal on Selected Areas in Communications*, vol. 31, no. 2, pp. 172–179, 2013.

[10] F. Rusek, D. Persson, B. K. Lau, E. G. Larsson, T. L. Marzetta, O. Edfors, and F. Tufvesson, "Scaling up mimo: Opportunities and challenges with very large arrays," *IEEE signal processing magazine*, vol. 30, no. 1, pp. 40–60, 2012.

[11] H. Q. Ngo, A. Ashikhmin, H. Yang, E. G. Larsson, and T. L. Marzetta, "Cell-free massive mimo versus small cells," *IEEE Transactions on Wireless Communications*, vol. 16, no. 3, pp. 1834–1850, 2017.

[12] C.-M. Chen, V. Volskiy, A. Chiumento, L. Van der Perre, G. A. Vandenbosch, and S. Pollin, "Exploration of user separation capabilities by distributed large antenna arrays," in *2016 IEEE Globecom Workshops (GC Wkshps)*. IEEE, 2016, pp. 1–6.

[13] E. Björnson, M. Matthaiou, A. Pitarokoilis, and E. G. Larsson, "Distributed massive mimo in cellular networks: Impact of imperfect hardware and number of oscillators," in *2015 23rd European Signal Processing Conference (EUSIPCO)*. IEEE, 2015, pp. 2436–2440.

[14] J.-C. Guey and L. D. Larsson, "Modeling and evaluation of mimo systems exploiting channel reciprocity in tdd mode," in *IEEE 60th Vehicular Technology Conference, 2004. VTC2004-Fall. 2004*, vol. 6. IEEE, 2004, pp. 4265–4269.

[15] X. Luo, "Multiuser massive mimo performance with calibration errors," *IEEE Transactions on Wireless Communications*, vol. 15, no. 7, pp. 4521–4534, 2016.

[16] W. Zhang, H. Ren, C. Pan, M. Chen, R. C. de Lamare, B. Du, and J. Dai, "Large-scale antenna systems with ul/dl hardware mismatch: Achievable rates analysis and calibration," *IEEE transactions on communications*, vol. 63, no. 4, pp. 1216–1229, 2015.

[17] X. Jiang, F. Kaltenberger, and L. Deneire, "How accurately should we calibrate a massive mimo tdd system?" in *2016 IEEE International Conference on Communications Workshops (ICC)*. IEEE, 2016, pp. 706–711.

[18] A. Bourdoux, B. Come, and N. Khaled, "Non-reciprocal transceivers in ofdm/sdma systems: Impact and mitigation," in *Radio and Wireless Conference, 2003. RAWCON'03. Proceedings*. IEEE, 2003, pp. 183–186.

[19] K. Nishimori, K. Cho, Y. Takatori, and T. Hori, "Automatic calibration method using transmitting signals of an adaptive array for tdd systems," *IEEE transactions on vehicular technology*, vol. 50, no. 6, pp. 1636–1640, 2001.

[20] K. Nishimori, T. Hiraguri, T. Ogawa, and H. Yamada, "Effectiveness of implicit beamforming using calibration technique in massive mimo system," in *2014 IEEE International Workshop on Electromagnetics (iWEM)*. IEEE, 2014, pp. 117–118.

[21] M. Petermann, M. Stefer, F. Ludwig, D. Wubben, M. Schneider, S. Paul, and K.-D. Kammeyer, "Multi-user pre-processing in multi-antenna ofdm tdd systems with non-reciprocal transceivers," *IEEE Transactions on Communications*, vol. 61, no. 9, pp. 3781–3793, 2013.

[22] A. Benzin and G. Caire, "Internal self-calibration methods for large scale array transceiver software-defined radios," in *WSA 2017; 21th International ITG Workshop on Smart Antennas*. VDE, 2017, pp. 1–8.

[23] M. Guillaud, D. T. Slock, and R. Knopp, "A practical method for wireless channel reciprocity exploitation through relative calibration." in *ISSPA*, 2005, pp. 403–406.

[24] F. Kaltenberger, H. Jiang, M. Guillaud, and R. Knopp, "Relative channel reciprocity calibration in mimo/tdd systems," in *2010 Future Network & Mobile Summit.* IEEE, 2010, pp. 1–10.

[25] J. Shi, Q. Luo, and M. You, "An efficient method for enhancing tdd over the air reciprocity calibration," in *2011 IEEE Wireless Communications and Networking Conference.* IEEE, 2011, pp. 339–344.

[26] B. Kouassi, I. Ghauri, B. Zayen, and L. Deneire, "On the performance of calibration techniques for cognitive radio systems," in *2011 The 14th International Symposium on Wireless Personal Multimedia Communications (WPMC).* IEEE, 2011, pp. 1–5.

[27] C. Shepard, H. Yu, N. Anand, E. Li, T. Marzetta, R. Yang, and L. Zhong, "Argos: Practical many-antenna base stations," in *Proceedings of the 18th annual international conference on Mobile computing and networking.* ACM, 2012, pp. 53–64.

[28] R. Rogalin, O. Y. Bursalioglu, H. Papadopoulos, G. Caire, A. F. Molisch, A. Michaloliakos, V. Balan, and K. Psounis, "Scalable synchronization and reciprocity calibration for distributed multiuser mimo," *IEEE Transactions on Wireless Communications*, vol. 13, no. 4, pp. 1815–1831, 2014.

[29] J. Vieira, F. Rusek, and F. Tufvesson, "Reciprocity calibration methods for massive mimo based on antenna coupling," in *2014 IEEE Global Communications Conference.* IEEE, 2014, pp. 3708–3712.

[30] J. Vieira, F. Rusek, O. Edfors, S. Malkowsky, L. Liu, and F. Tufvesson, "Reciprocity calibration for massive mimo: Proposal, modeling, and validation," *IEEE Transactions on Wireless Communications*, vol. 16, no. 5, pp. 3042–3056, 2017.

[31] H. Papadopoulos, O. Y. Bursalioglu, and G. Caire, "Avalanche: Fast rf calibration of massive arrays," in *2014 IEEE Global Conference on Signal and Information Processing (GlobalSIP).* IEEE, 2014, pp. 607–611.

[32] X. Jiang, A. Decunringe, K. Gopala, F. Kaltenberger, M. Guillaud, D. Slock, and L. Deneire, "A framework for over-the-air reciprocity calibration for TDD massive MIMO systems," *IEEE Transactions on Wireless Communications*, vol. 17, no. 9, pp. 5975–5990, Sep. 2018. [Online]. Available: http://arxiv.org/abs/1710.10830

[33] F.-L. Luo and C. J. Zhang, *Signal processing for 5G: algorithms and implementations.* John Wiley & Sons, 2016.

[34] S. Malkowsky, J. Vieira, L. Liu, P. Harris, K. Nieman, N. Kundargi, I. C. Wong, F. Tufvesson, V. Öwall, and O. Edfors, "The world's first real-time testbed for

massive mimo: Design, implementation, and validation," *IEEE Access*, vol. 5, pp. 9073–9088, 2017.

[35] J. C. Eidson, *Measurement, control, and communication using IEEE 1588.* Springer Science & Business Media, 2006.

[36] K. Hann, S. Jobert, and S. Rodrigues, "Synchronous ethernet to transport frequency and phase/time," *IEEE Communications Magazine*, vol. 50, no. 8, pp. 152–160, 2012.

[37] T. Bigler, A. Treytl, D. Löschenbrand, and T. Zemen, "High accuracy synchronization for distributed massive mimo using white rabbit," in *2018 IEEE International Symposium on Precision Clock Synchronization for Measurement, Control, and Communication (ISPCS).* IEEE, 2018, pp. 1–6.

[38] F. Kaltenberger, X. Jiang, and R. Knopp, "From massive MIMO to C-RAN: the OpenAirInterface 5G testbed," in *Proceeding of Asilomar Conference on Signals, Systems, and Computers*, Pacific Grove, CA, Oct. 2017.

[39] A. J. Paulraj and T. Kailath, "Increasing capacity in wireless broadcast systems using distributed transmission/directional reception (dtdr)," Sep. 6 1994, uS Patent 5,345,599.

[40] K. S. V. Prasad, E. Hossain, and V. K. Bhargava, "Energy efficiency in massive mimo-based 5g networks: Opportunities and challenges," *IEEE Wireless Communications*, vol. 24, no. 3, pp. 86–94, 2017.

[41] O. Elijah, C. Y. Leow, T. A. Rahman, S. Nunoo, and S. Z. Iliya, "A comprehensive survey of pilot contamination in massive mimo—5g system," *IEEE Communications Surveys & Tutorials*, vol. 18, no. 2, pp. 905–923, 2015.

[42] E. G. Larsson, O. Edfors, F. Tufvesson, and T. L. Marzetta, "Massive mimo for next generation wireless systems," *IEEE communications magazine*, vol. 52, no. 2, pp. 186–195, 2014.

[43] T. L. Marzetta, *Fundamentals of massive MIMO.* Cambridge University Press, 2016.

[44] C. E. Shannon, "A mathematical theory of communication," *The Bell system technical journal*, vol. 27, no. 3, pp. 379–423, 1948.

[45] E. Dahlman, S. Parkvall, J. Skold, and P. Beming, *3G evolution: HSPA and LTE for mobile broadband.* Academic press, 2010.

[46] S. Deshpande, "Appendix b: Introduction to mimo and massive mimo," *Fundamentals of Network Planning and Optimisation 2G/3G/4G: Evolution to 5G*, pp. 325–335, 2018.

[47] A. Goldsmith, S. A. Jafar, N. Jindal, and S. Vishwanath, “Capacity limits of mimo channels,” *IEEE Journal on selected areas in Communications*, vol. 21, no. 5, pp. 684–702, 2003.

[48] D. Tse and P. Viswanath, “Mimo ii: capacity and multiplexing architectures,” in *Fundamentals of Wireless Communication.* Stanford Univ. Press, 2005, pp. 332–376.

[49] E. Telatar, “Capacity of multi-antenna gaussian channels,” *European transactions on telecommunications*, vol. 10, no. 6, pp. 585–595, 1999.

[50] D. Gesbert, M. Kountouris, R. W. Heath, C.-B. Chae, and T. Salzer, “Shifting the mimo paradigm,” *IEEE signal processing magazine*, vol. 24, no. 5, pp. 36–46, 2007.

[51] G. Caire and S. Shamai, “On the achievable throughput of a multiantenna gaussian broadcast channel,” *IEEE Transactions on Information Theory*, vol. 49, no. 7, pp. 1691–1706, 2003.

[52] P. Viswanath and D. N. C. Tse, “Sum capacity of the vector gaussian broadcast channel and uplink-downlink duality,” *IEEE Transactions on Information Theory*, vol. 49, no. 8, pp. 1912–1921, 2003.

[53] S. Vishwanath, N. Jindal, and A. Goldsmith, “Duality, achievable rates, and sum-rate capacity of gaussian mimo broadcast channels,” *IEEE Transactions on Information Theory*, vol. 49, no. 10, pp. 2658–2668, 2003.

[54] H. Q. Ngo, *Massive MIMO: Fundamentals and system designs.* Linköping University Electronic Press, 2015, vol. 1642.

[55] H. Q. Ngo and E. G. Larsson, “No downlink pilots are needed in tdd massive mimo,” *IEEE Transactions on Wireless Communications*, vol. 16, no. 5, pp. 2921–2935, 2017.

[56] E. Björnson, J. Hoydis, and L. Sanguinetti, “Massive mimo networks: Spectral, energy, and hardware efficiency,” *Foundations and Trends in Signal Processing*, vol. 11, no. 3-4, pp. 154–655, 2017.

[57] H. Q. Ngo and E. G. Larsson, “Blind estimation of effective downlink channel gains in massive mimo,” in *2015 IEEE International Conference on Acoustics, Speech and Signal Processing (ICASSP).* IEEE, 2015, pp. 2919–2923.

[58] P. Almers, F. Tufvesson, and A. F. Molisch, “Keyhole effect in mimo wireless channels: Measurements and theory,” *IEEE Transactions on Wireless Communications*, vol. 5, no. 12, pp. 3596–3604, 2006.

[59] X. Li, S. Jin, X. Gao, and M. R. McKay, “Capacity bounds and low complexity transceiver design for double-scattering mimo multiple access channels,” *IEEE transactions on signal processing*, vol. 58, no. 5, pp. 2809–2822, 2010.

[60] C. Zhong, S. Jin, K.-K. Wong, and M. R. McKay, "Ergodic mutual information analysis for multi-keyhole mimo channels," *IEEE transactions on wireless communications*, vol. 10, no. 6, pp. 1754–1763, 2011.

[61] G. Levin and S. Loyka, "From multi-keyholes to measure of correlation and power imbalance in mimo channels: Outage capacity analysis," *IEEE transactions on information theory*, vol. 57, no. 6, pp. 3515–3529, 2011.

[62] A. A. M. Saleh, A. Rustako, and R. Roman, "Distributed antennas for indoor radio communications," *IEEE Transactions on Communications*, vol. 35, no. 12, pp. 1245–1251, December 1987.

[63] H. Q. Ngo, A. Ashikhmin, H. Yang, E. G. Larsson, and T. L. Marzetta, "Cell-free massive mimo: Uniformly great service for everyone," in *2015 IEEE 16th international workshop on signal processing advances in wireless communications (SPAWC).* IEEE, 2015, pp. 201–205.

[64] C. Masterson, "Massive mimo and beamforming: the signal processing behind the 5g buzzwords," *10 Massive MIMO and Beamforming: The Signal Processing Behind the 5G Buzzwords*, p. 10, 2017.

[65] T. Schenk, *RF imperfections in high-rate wireless systems: impact and digital compensation.* Springer Science & Business Media, 2008.

[66] G. Fettweis, M. Löhning, D. Petrovic, M. Windisch, P. Zillmann, and W. Rave, "Dirty rf: A new paradigm," *International Journal of Wireless Information Networks*, vol. 14, no. 2, pp. 133–148, 2007.

[67] D. Petrovic, W. Rave, and G. Fettweis, "Effects of phase noise on ofdm systems with and without pll: Characterization and compensation," *IEEE Transactions on Communications*, vol. 55, no. 8, pp. 1607–1616, 2007.

[68] A. K. Poddar, U. L. Rohde, and A. M. Apte, "How low can they go?: Oscillator phase noise model, theoretical, experimental validation, and phase noise measurements," *IEEE microwave magazine*, vol. 14, no. 6, pp. 50–72, 2013.

[69] H. Wei, D. Wang, H. Zhu, J. Wang, S. Sun, and X. You, "Mutual coupling calibration for multiuser massive mimo systems," *IEEE Transactions on Wireless Communications*, vol. 15, no. 1, pp. 606–619, 2015.

[70] Y. Hara, Y. Yano, and H. Kubo, "Antenna array calibration using frequency selection in ofdma/tdd systems," in *IEEE GLOBECOM 2008-2008 IEEE Global Telecommunications Conference.* IEEE, 2008, pp. 1–5.

[71] T. Salman, "Cloud ran: Basics, advances and challenges," *A Surv. C-RAN Basics Virtualization Resour. Alloc. Chall*, pp. 1–16, 2016.

[72] L. Gavrilovska, V. Rakovic, and D. Denkovski, "From cloud ran to open ran," *Wireless Personal Communications*, pp. 1–17, 2020.

[73] A. Checko, H. Christiansen, Y. Yan, L. Scolaris, G. Kardaras, and M. Berger, "L. dittman—cloud ran for mobile networks-a technology overview," *IEEE Communications surveys & tutorials, vol. PP*, no. 99, 2014.

[74] V. Rakovic, A. Ichkov, S. Marinova, D. Todorovski, V. Atanasovski, and L. Gavrilovska, "Dynamic virtual resource allocation in virtualized multi-rat cellular networks," *Wireless Personal Communications*, vol. 97, no. 2, pp. 1677–1692, 2017.

[75] A. Checko, H. L. Christiansen, Y. Yan, L. Scolari, G. Kardaras, M. S. Berger, and L. Dittmann, "Cloud ran for mobile networks—a technology overview," *IEEE Communications surveys & tutorials*, vol. 17, no. 1, pp. 405–426, 2014.

[76] "O-ran alliance white paper o-ran: Towards an open and smart ran," https://static1.squarespace.com/static/5ad774cce74940d7115044b0/t/5bc79b371905f4197055e8c6/1539808057078/O-RAN+WP+FInal+181017.pdf.

[77] O. R. Alliance, "O-ran: towards an open and smart ran," *White Paper*, 2018.

[78] "The race to Open RAN is a marathon, not a sprint." https://www.huawei.com/en/publications/communicate/89/open-ran-is-a-marathon-not-a-sprint.

[79] D. Venmani, Y. Lagadec, O. Lemoult, and F. Deletre, "Phase and time synchronization for 5g c-ran: Requirements, design challenges and recent advances in standardization," *EAI Endorsed Transactions on Industrial Networks and Intelligent Systems*, vol. 5, no. 15, 2018.

[80] "Transforming Next-Generation Wireless with 5T for 5G and the NVIDIA Aerial SDK." https://developer.nvidia.com/blog/transforming-next-gen-wireless-with-5t-for-5g-and-aerial-sdk/.

[81] "5G is all in the timing," https://www.ericsson.com/en/blog/2019/8/what-you-need-to-know-about-timing-and-sync-in-5g-transport-networks.

[82] J. Bartelt, N. Vucic, D. Camps-Mur, E. Garcia-Villegas, I. Demirkol, A. Fehske, M. Grieger, A. Tzanakaki, J. Gutierrez, E. Grass *et al.*, "5g transport network requirements for the next generation fronthaul interface," *EURASIP Journal on Wireless Communications and Networking*, vol. 2017, no. 1, pp. 1–12, 2017.

[83] "New Transport Network Architectures for 5G RAN," https://www.fujitsu.com/us/Images/New-Transport-Network-Architectures-for-5G-RAN.pdf.

[84] A. U. T. Yajima, T. Uchino, and S. Okuyama, "Overview of o-ran fronthaul specifications," 2019.

[85] H. Wei, D. Wang, H. Zhu, J. Wang, S. Sun, and X. You, "Mutual coupling calibration for multiuser massive MIMO systems," *IEEE Trans. on Wireless Commun.*, vol. 15, no. 1, pp. 606–619, 2016.

[86] R. Rogalin, O. Y. Bursalioglu, H. C. Papadopoulos, G. Caire, and A. F. Molisch, "Hardware-impairment compensation for enabling distributed large-scale mimo," in *2013 Information Theory and Applications Workshop (ITA).* IEEE, 2013, pp. 1–10.

[87] "OpenAirInterface: 5G software alliance for democratising wireless innovation," http://www.openairinterface.org/.

[88] E. Dahlman, S. Parkvall, and J. Skold, *4G: LTE/LTE-advanced for mobile broadband.* Academic press, 2013.

[89] M. Passoja, "5g nr: Massive mimo and beamforming–what does it mean and how can i measure it in the field?" *Retrieved April*, vol. 1, p. 2020, 2018.

[90] 3GPP, "Technical Specification 38.801: Study on new radio access technology; Radio access architecture and interfaces." [Online]. Available: www.3gpp.org

[91] T. Magounaki, F. Kaltenberger, and R. Knopp, "Real-time performance evaluation of relative calibration on the oai 5g testbed," in *2019 53rd Asilomar Conference on Signals, Systems, and Computers.* IEEE, 2019, pp. 564–568.

[92] 3GPP, "Evolved universal terrestrial radio access (E-UTRA); physical channels and modulation," 3GPP, Tech. Rep. Technical Specification 36.211 V15.2.0 Release 15, October 2018.

[93] T. Magounaki, F. Kaltenberger, and R. Knopp, "Modeling the distributed mu-mimo oai 5g testbed and group-based ota calibration performance evaluation," in *2020 IEEE 21st International Workshop on Signal Processing Advances in Wireless Communications (SPAWC).* IEEE, 2020, pp. 1–5.

[94] N. Nikaein, R. Knopp, F. Kaltenberger, L. Gauthier, C. Bonnet, D. Nussbaum, and R. Ghaddab, "Openairinterface: an open lte network in a pc," in *Proceedings of the 20th annual international conference on Mobile computing and networking*, 2014, pp. 305–308.

[95] "Kollmorgen s300 servo drive manual," https://www.kollmorgen.com/sites/default/files/public_downloads/Kollmorgen%20S300%20Servo%20drive%20Manual.pdf.

[96] "Akm series servo motor," https://www.kollmorgen.com/en-us/products/motors/servo/akm-series/akm-series-ac-synchronous-motors/ac-synchronous-servo-motors/.

[97] J.-M. Floch, B. El Jaafari, and A. E. S. Ahmed, "New compact broadband gsm/umts/lte antenna realised by 3d printing," in *2015 9th European Conference on Antennas and Propagation (EuCAP).* IEEE, 2015, pp. 1–4.

[98] F. Sonnerat, R. Pilard, F. Gianesello, F. Le Pennec, C. Person, and D. Gloria, "Innovative lds antenna for 4g applications," in *2013 7th European Conference on Antennas and Propagation (EuCAP).* IEEE, 2013, pp. 2773–2776.

[99] F. Ferrero, L. Lizzi, R. Staraj, J.-M. Ribero *et al.*, "Reconfigurable antenna for future spectrum reallocations in 5g communications," *IEEE Antennas and Wireless Propagation Letters*, vol. 15, pp. 1297–1300, 2015.

[100] B. Kouassi, L. Deneire, B. Zayen, R. Knopp, F. Kaltenberger, F. Negro, D. Slock, and I. Ghaur, "Design and implementation of spatial interweave lte-tdd cognitive radio communication on an experimental platform," *IEEE wireless communications*, vol. 20, no. 2, pp. 60–67, 2013.

[101] X. Jiang, M. Čirkić, F. Kaltenberger, E. G. Larsson, L. Deneire, and R. Knopp, "Mimo-tdd reciprocity under hardware imbalances: Experimental results," in *2015 IEEE International Conference on Communications (ICC)*. IEEE, 2015, pp. 4949–4953.

[102] T. Magounaki, F. Kaltenberger, X. Jiang, C. Buey, P. Ratajczak, and F. Ferrero, "Experimental evaluation of relative calibration in a miso-tdd system," in *2017 European Conference on Networks and Communications (EuCNC)*. IEEE, 2017, pp. 1–5.

[103] C. Buey, T. Magounaki, F. Ferrero, P. Ratajczak, L. Lizzi, and F. Kaltenberger, "Mimo antenna performance assessment based on open source software defined radio," in *2017 11th European Conference on Antennas and Propagation (EUCAP)*. IEEE, 2017, pp. 644–647.

[104] C. Buey, P. Ratajczak, F. Ferrero, L. Lizzi, T. Magounaki, and F. Kaltenberger, "Validation of an open source software defined radio test bed," in *2017 IEEE International Symposium on Antennas and Propagation & USNC/URSI National Radio Science Meeting*. IEEE, 2017, pp. 1875–1876.

[105] D.-T. Phan-Huy, Y. Kokar, K. Rachedi, P. Pajusco, A. Mokh, T. Magounaki, R. Masood, C. Buey, P. Ratajczak, N. Malhouroux-Gaffet *et al.*, "Single-carrier spatial modulation for the internet of things: Design and performance evaluation by using real compact and reconfigurable antennas," *IEEE access*, vol. 7, pp. 18 978–18 993, 2019.

[106] P. Yang, Y. Xiao, Y. L. Guan, K. Hari, A. Chockalingam, S. Sugiura, H. Haas, M. Di Renzo, C. Masouros, Z. Liu *et al.*, "Single-carrier sm-mimo: A promising design for broadband large-scale antenna systems," *IEEE Communications Surveys & Tutorials*, vol. 18, no. 3, pp. 1687–1716, 2016.

[107] Y. Kokar, J.-C. Prévotet, and M. Hélard, "Receive antenna shift keying modulation testbed for wireless communications systems," in *2016 IEEE Globecom Workshops (GC Wkshps)*. IEEE, 2016, pp. 1–6.

[108] D.-T. Phan-Huy, S. B. Halima, and M. Hélard, "Dumb-to-perfect receiver throughput ratio maps of a time reversal wireless indoor system," in *ICT 2013*. IEEE, 2013, pp. 1–5.

[109] E. Björnson, L. Sanguinetti, H. Wymeersch, J. Hoydis, and T. L. Marzetta, "Massive mimo is a reality—what is next?: Five promising research directions for antenna arrays," *Digital Signal Processing*, vol. 94, pp. 3–20, 2019.